MULTI-HAZARD PERFORMANCE OF BRIDGE TIMBER PILES RETROFITTED WITH FIBER REINFORCED POLYMER COMPOSITES

BY

KUN-HO EUGENE KIM

DISSERTATION

Submitted in partial fulfillment of the requirements
for the degree of Doctor of Philosophy in Civil Engineering
in the Graduate College of the
University of Illinois at Urbana-Champaign, 2018

Urbana, Illinois

Doctoral Committee:

Associate Professor Bassem Andrawes, Chair and Director of Research
Professor C. Armando Duarte
Professor James M. LaFave
Professor David A. Lange

ABSTRACT

Bridges with various timber structural components make up a large portion of the transportation infrastructure in the US. Bridges supported on timber pile substructure, simply referred to as timber pile bridges, are particularly common. Many timber pile bridges still in service today were constructed in the 1950's and 60's using simplified design approaches largely based on convention and empirical data. Since only gravity loads were considered in their original design, many timber pile bridges are deficient by modern standards. Further exacerbating this problem is their age and the susceptibility to degradation. Despite these issues, timber bridges in general are overlooked in terms of operational importance and afforded minimal maintenance effort. Furthermore, whereas countless research studies have focused on every aspect of conventional reinforced concrete or steel bridges, research activity on timber bridges has been almost non-existent. Given ever increasing demands on bridges and interest in sustainable, resilient structures, the time is now to close the gap.

The first part of this research is devoted to the experimental testing of timber piles with a special focus on the short- and long-term performance of piles retrofitted with fiber reinforced polymer (FRP) composites. The impact of timber deterioration and the effectiveness of different FRP application strategies are examined to make retrofit design recommendations, and a unique accelerated aging procedure is used to study their durability. In the second part of the research, numerical approaches are used to develop methods for estimating the capacity of deteriorated timber pile bridge substructure. This includes a comprehensive load rating method for abutment timber piles in which the in-situ pile condition is a key input parameter as well as performance prediction models for bridges subject to earthquake-tsunami hazards. Under earthquake-tsunami loading considerations, a sequential analysis framework is used to perform nonlinear dynamic time history analyses and tsunami impact simulations using the particle finite element method (PFEM). Failure criteria for a typical bridge are introduced in the form of earthquake-tsunami hazard interaction diagrams then a probabilistic approach is used to quantify the effect of damage accumulation and introduce the concept of a demand amplification factor.

The findings from this research clearly demonstrate the need to more carefully consider the safety of existing timber bridges, and show that proper maintenance and retrofitting can significantly improve their strength and durability. Most importantly, this research contributes simple and robust tools for assessing the vulnerability of timber pile bridges under both typical service conditions and multi-hazard scenarios.

ACKNOWLEDGEMENTS

This dissertation could not have been possible without the help and support of many different people. First and foremost, I must thank Professor Bassem Andrawes for providing me with the opportunity to take on this research in the first place and for his guidance through it all. His vision and expertise provided the foundation upon which to build my knowledge and helped me find my direction as a scholar. I simply would not be who I am today without him.

I also want to sincerely thank Professor Carlos Armando Duarte for introducing me to PFEM and his invaluable guidance. My interest in numerical analysis and computational methods truly burgeoned under his tutelage. I would also like to sincerely thank my other committee members, Professor James LaFave and Professor David Lange for their insightful feedback on this dissertation, as well as Tim Prunkard, Darold Marrow, Don Marrow, and the entire Civil Engineering Machine Shop for their assistance in the experimental component of this research. I must also thank members of our research group, both old and new. Dr. Qiwen Chen, Hang Zhao, Minsoo Sung, and Pratik Deogekar have all helped me in various ways and I am grateful.

I have made so many great friends during my time here at the University of Illinois that I cannot possibly thank them all individually within the confines of a few pages. I owe a particular debt of gratitude to Donghyuk Jung who has become a brother to me. His help was instrumental in my experimental work and his words of encouragement helped me through some very tough times. Along the same lines, I must also thank Dr. Hajin Choi who has always been a guiding example and thank all the Korean students in Civil Engineering, particularly Andy Hur, Jaeho Shin, Homin Song, and Soonpil Kang for keeping me sane. I also want to thank some old friends who are far away but close to my heart, Scott Jones, Justin Lee, and Olivier Daigle. Our friendship is both a place of refuge and a source of energy.

Finally, I need to thank my family. I would not be here if not for my parents, my sister, and my brother. Thank you for the love and always believing in me. I am most greatly indebted to my wife and words cannot begin to describe how much she means to me. She sacrificed everything to allow me to pursue this path and every single day I am grateful for having met someone like her. Thank you for your unequivocal love and for giving us Lucas and Andrew, the two most precious jewels of my life.

This study was supported in part by the Illinois Center for Transportation (ICT) and the Illinois Department of Transportation (IDOT) under project No. R27-134.

For my wife Songyi and

Our Boys Lucas and Andrew

TABLE OF CONTENTS

CHAPTER 1

INTRODUCTION

1.1 PROBLEM DESCRIPTION

There exists a general sense of urgency throughout the US regarding the safety and resilience of the rapidly degrading infrastructure in the face of growing threats from both anthropogenic and natural hazards. Although there is popular belief that timber bridges are an insignificant and obscure subset of the bridge inventory in the US, bridges with significant timber structural components still in service number in the tens of thousands. According to the National Bridge Inventory (NBI), approximately 7% of all highway bridges in the US have a timber structural component. Bridges with supported on timber pile substructure, simply referred to as timber pile bridges, is a special subset of timber bridges that are not only distinctive in design but also present unique challenges. Although the Federal Highway Administration (FHWA) does not distinguish the timber bridges in their inventory by component type, a study published in 1994 by Holt et al. estimated up to 240,000 bridges are supported on timber piles in the US. This research focuses on the particular case of timber pile bridges, most of which were constructed in the 1950's and 60's. Despite the fact that a large number of these structures are still in service, there is a great lack of interest in the performance and maintenance of timber bridges. Whereas immense amounts of effort have been dedicated to researching almost every aspect of concrete and steel structures, there is very little information in the literature on timber bridges.

The design of most timber pile bridges is extremely simple with many provisions derived from convention or experience. Furthermore, because traditional design practices only took standard gravity loads into consideration, they lack the redundancy and robustness characteristic of modern structures. As a result, even a minor deviation from the original design loads can significantly increase the risk of catastrophic failure. Further exacerbating this problem is their age and the susceptibility of timber to deterioration. Although preservative treatments can reduce problems due to biological degradation, it is by no means a perfect solution. The natural tendency for wood to split and exposure to wet-dry cycles can accelerate decay which can critically reduce strength and lead to section loss. In 1996, timber bridges accounted for approximately 18% of all structurally deficient bridges in the US (Duwadi and Wood 1996). This number is likely to have grown by a large margin in the past two decades. Despite these factors, most timber pile bridges receive minimal maintenance because they typically span lower traffic roads.

For aged and deteriorated timber pile bridges to meet current load demands as well as other more extreme load cases unanticipated in the original design, there is a definite need to retrofit or strengthen the timber piles. In recent years, fiber reinforced polymer (FRP) composites have become a popular material for a variety of structural applications including applications to timber structures. FRP can be used in a number of different ways to enhance stiffness, strength and ductility in timber. Although the effectiveness of FRP retrofitted timber has already been demonstrated in different research studies (Plevris & Triantafillou 1992; Hagos 2001; Lopez-Anido et al. 2003; among others) there are no standardized guidelines for design and significant uncertainty regarding their long-term performance.

Timber pile bridges offer an interesting deviation from typical bridge structures. Their distinctive construction results in unique problems and structural response that is not well understood. As construction costs rise and funding for infrastructure decline, it is becoming increasingly more important to develop effective repair strategies to prolong the service life of existing infrastructure. In addition, fast growing interest in structural resilience and societal focus on sustainability add greater pressure to address the knowledge gap that exist in the behavior of timber bridges and introduce robust platforms for evaluating and strengthening existing timber pile bridges to ascertain their safety.

1.2 RESEARCH OBJECTIVES AND SCOPE

The term *timber bridge* is used to collectively describe bridges with timber structural components. This research, however, focuses on the specific case of timber pile bridges and aims to address the needs identified above through four main objectives:

1. Developing a multi-parameter load rating method for evaluating the safe loading capacity of timber piles with consideration for in-situ pile and loading conditions
2. Developing FRP retrofit design guidelines for deteriorated timber piles.
3. Investigating the durability and long-term performance of FRP retrofitted timber.
4. Assessment of timber pile bridge performance under various multiple hazard loading scenarios including combinations of construction error, severe deterioration, overloading, seismic loading, and tsunami inundation.

The load rating method in the first objective was developed specifically for abutment timber piles but is generally applicable to any timber pile loaded in compression with lateral loads. The second and third objectives involved a sizable experimental component in which out-of-service Red Oak timber piles were used as test specimens. The pile specimens were obtained from various bridges in the state of Illinois and assessing their condition was a key component in the experimental studies. For this purpose, a non-destructive stress wave timing (SWT) technique was used. Although the results from this study show that SWT is a reliable inspection method, further studies are recommended given the limited scope and sample size.

Numerical models developed in this study were based on generalizations made from information found in the as-built drawings for several timber pile bridges in Illinois. A thorough review has shown that typical timber pile bridge design is simple with little variation from structure to structure. In the last objective, numerical simulations were extensively used to model timber pile bridge response under earthquake-tsunami hazards. There is absolutely no precedent in the literature on the performance of timber bridges in tsunami scenarios. While the analysis of earthquake-tsunami hazards in this research specifically focuses on timber pile bridges, the ideas are directly applied to any structure of any material composition. One of the main goals of this dissertation is to somewhat fill the great knowledge void mentioned above but also to serve as a guideline for studying the performance of other structures in earthquake-tsunami hazards. This dissertation only details the experiments and numerical analyses conducted to achieve the objectives listed above and is by no means a complete authoritative manual on all facets of timber pile bridges.

1.3 DOCUMENT OUTLINE

This dissertation is composed of eight chapters:

- Chapter 2: Literature Review

  An overview of common timber pile bridge design and maintenance practices. Information on traditional design methods, problems caused by timber deterioration, retrofitting, and design for earthquake and tsunami hazards is presented.

- Chapter 3: Long-term Performance of FRP Strengthened Timber Piles

The durability and performance of FRP retrofitted timber piles after long-term degradation under field conditions was tested using an accelerated aging procedure. 20 specimens were wrapped with glass-FRP (GFRP) composites manufactured using different resins at varying thicknesses. The accelerated aging protocol exposed specimens to alternating wet-dry and freeze-thaw cycles at elevated temperatures to artificially simulate harsh exposure conditions. The specimens were then tested under uniaxial compression to compare strength, ductility, and failure patterns.

- Chapter 4: Retrofitting of Abutment Timber Piles Using FRP Composites

  Three full-scale timber piles were tested under combined compression and bending using a unique test setup. The piles were inspected using SWT and FRP was used to retrofit two of the specimens in flexure. Correlations were drawn between the SWT measurements and test results to show the effect of deterioration on timber pile behavior. These results were also used to calibrate timber material models and a finite element model was used to quantify the effect of deterioration and use the information to iteratively design FRP retrofits.

- Chapter 5: Load Rating of Deteriorated and FRP Retrofitted Abutment Timber Piles

  A new load rating equation is derived for timber piles carrying axial and lateral loads. An elastic analysis approach is also introduced for estimating the capacity abutment timber piles with FRP retrofits. The new load rating method is applied to a finite element model of a typical abutment timber pile and a series of charts are developed for graphically determining the load rating of a pile with dead load, pile length, soil pressure, and pile section loss as input. The proposed method is compared to the traditional load rating equation using a prototype timber pile bridge.

- Chapter 6: Multi-Hazard Assessment and Retrofit of Deteriorated Timber Pile Bridges

  Since typical timber pile bridges were designed simply for gravity loads only, they are highly vulnerable to unanticipated load cases, particularly lateral loading. The response of a prototype unbraced timber pile bent was modeled using the software OpenSees under incrementally increasing combinations of earthquake ground motion and tsunami intensity to examine its behavior. The tsunami impact was simulated using PFEM and the results were consolidated into hazard interaction diagrams which define the ultimate limit of a typical timber pile bridge in terms of the hazard intensities. The effect of pile section loss and FRP retrofitting were also considered.

- Chapter 7: Damage Evaluation and Prediction of Timber Pile Bridges Subjected to Earthquake-Tsunami Scenarios

  Structures in tsunami zones must be designed such that there is enough residual capacity after the earthquake loading to resist the tsunami load effects. Although design standards and guidelines are being revised to include provisions for tsunami loading, they are unclear on how residual load effects from the earthquake impacts the structure in the subsequent tsunami inundation. This is an especially critical scenario for structures such as timber pile bridges that do not have the robustness of concrete or steel structures. Using timber pile bridges as an example, the idea of a tsunami demand amplification factor is introduced and a Monte Carlo approach is used to develop prediction models based on simplified load cases.

- Chapter 8: Conclusions and Recommendations

  Major findings and observations from the research are summarized and recommendations are made for future research.

CHAPTER 2

LITERATURE REVIEW

2.1 OVERVIEW OF TIMBER PILE BRIDGES

The first bridge structure in the United States constructed on treated round timber piles was the Taunton River Bridge in Massachusetts in 1865 Graham (1996). Most timber pile bridges remaining in service today were constructed between the 1950’s and 60’s and are mainly found on low volume roads. In 1989 and 1991 the federal government established the Timber Bridge Initiative and the Highway Timber Bridge Research and Demonstration Program to promote the use of timber as a cheap and sustainable material alternative for highway bridges (Duwadi & Wood 1996). However, it is difficult to find evidence that these initiatives led to a noticeable increase in the construction of timber bridges. In a study published in 1994, Holt et al., estimated there were up to 240,000 bridges supported on timber piles throughout the US (Holt et al. 1994). Typical timber pile bridges carry two lanes of traffic and consist of one or two simply-supported spans.

2.1.1 Typical Design

Shama & Mander (2003) note that timber bridges tend to follow convention rather than novel design and most do not deviate significantly from Federal Highway Administration (FHWA) Standard Plans. Extensive effort was made to procure a copy of the 1990 edition of the Standard Plans for Highway Bridges which is referred to by Shama & Mander (2003), however, only the 1962 edition could be found. Volume 3 of the standard plans provides plans for timber pile substructure and timber or timber-concrete composite superstructure (US Department of

Commerce 1962). The plans also provide design charts for determining timber stringer spacing based on span length and the design live load. The standard design for timber pile abutments and piers given in the Standard Plans is shown in Figure 2.1.

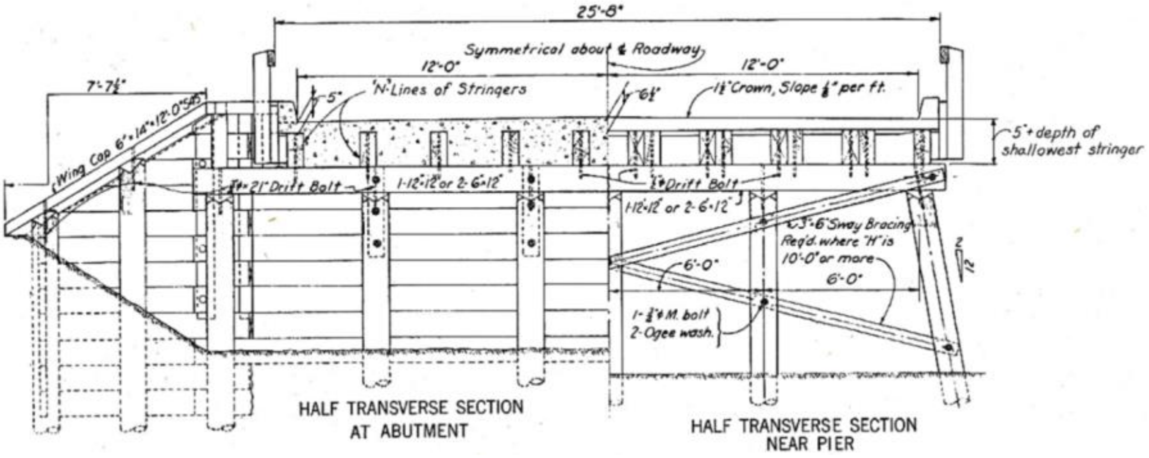

Figure 2.1 Typical timber pile substructure design from the 1962 edition of Standard Plans for Highway Bridges (US Department of Commerce 1962)

Figure 2.1 depicts a bridge with timber stringers and a concrete deck. However, substructure design was relatively consistent regardless of the superstructure type. As shown, the standard plans specify battered piles and a timber pile cap. Some general requirements imposed on the timber piles include preservative treatment, a minimum diameter of 12 inches (305 mm) at the pile butt, and a minimum baring capacity of 13 tons (116 kN) but there are no specific design requirements.

The type of timber bridge that is of specific interest in this study consist of timber pile substructure with reinforced concrete pile caps and precast concrete superstructure or a concrete deck with steel stringers. Commonly called a timber pile bridge, bridge structures of this kind are very common throughout the US. Figure 2.2 shows an example of a timber pile bridge.

a)

b)

Figure 2.2 A typical timber pile bridge **a)** Bridge elevation **b)** Timber pile bent

In most timber pile bridges, timber usage is limited to the substructure with typically five to seven piles supporting the abutments and bents. The piles are driven with the larger cross-section in the natural taper of the timber as the head and are embedded in a reinforced concrete pile cap as shown in Figure 2.2 b). The particular bridge shown in Figure 2.2 consists of steel girders and a cast-in-place deck supported on timber pile bents and abutments. However, precast beam-slab systems are also commonly used.

To establish a good understanding of timber pile bridge design, as-built drawings for several existing structures were carefully studied. It was observed that although the designs were not strictly comparable to the standard plans introduced above, they were remarkably similar to one another with many common details. Most of the as-built drawings were dated between 1945 and 1977 which suggests design standards did not evolve much over time and that many of these structures that are still in service may be in poor condition. Typical details seen in the as-built drawings are shown in Figure 2.3.

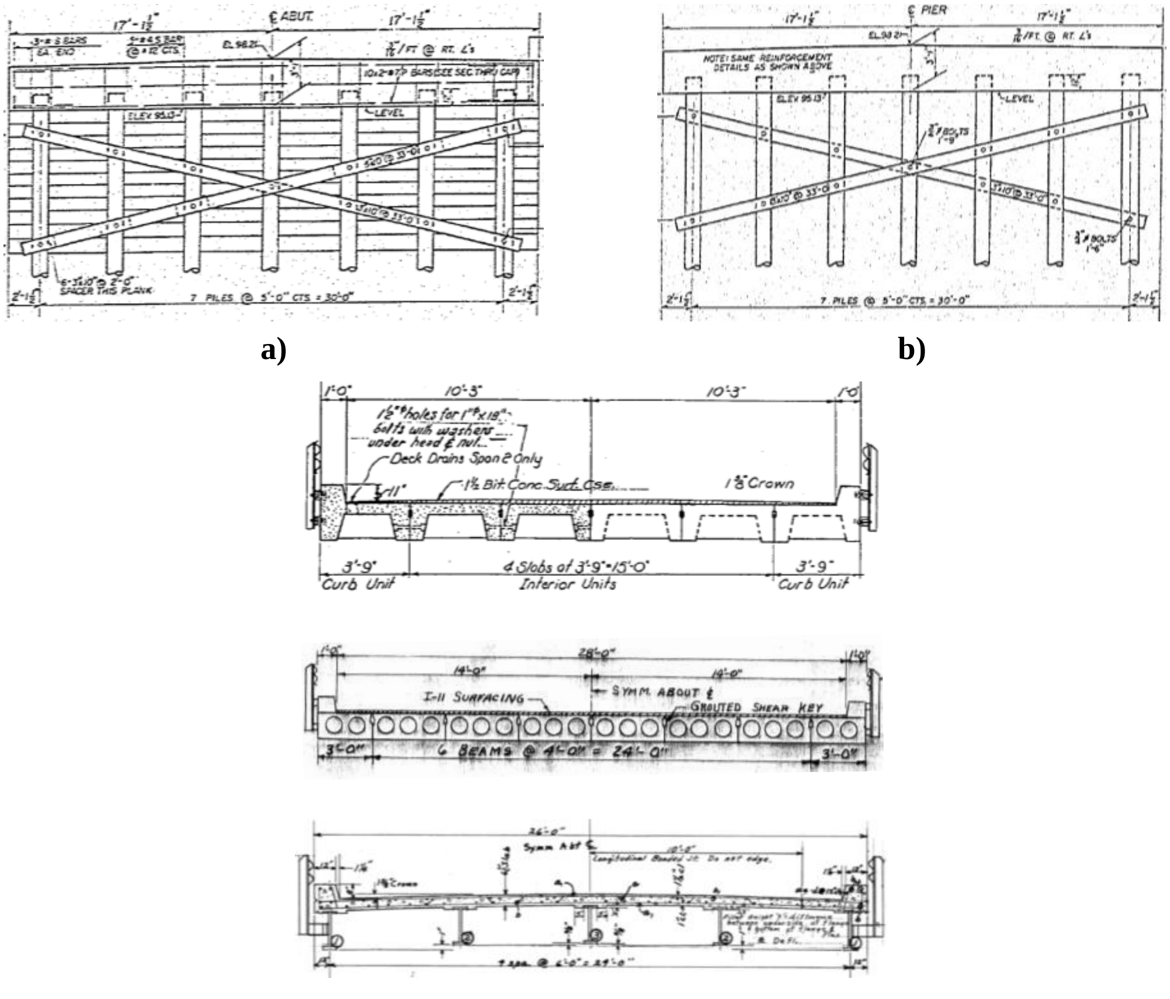

a) **b)**

c)

Figure 2.3 Schematic of typical timber pile bridge components **a)** Abutment **b)** Bent **c)** Typical superstructure types

As mentioned above, precast deck components or a concrete deck supported on steel stringers as shown in Figure 2.3 c) are the most common superstructure types. The deck is simply-supported on the pile caps with fabric bearing pads and dowel connections. Span lengths generally do not exceed 42 ft (12.8 m). The drawings uniformly specify round creosote treated timber piles with a minimum length of 30 ft (9.14 m) but do not indicate a minimum diameter or a particular wood species. The piles are typically spaced at less than 6 ft (1.83 m) and driven a minimum of 15 ft (4.57 m) with minimum capacities ranging between 12 tons (107 kN) and 24 tons (214 kN). It is unclear what these values are based on but it is likely that they were empirically derived as early timber pile design was largely based on observations of pile performance under comparable conditions and the results of static loading tests (AFPA 2005). The unsupported pile length above the ground surface does not exceed approximately 9 ft (2.74 m) and the piles are braced with 3 in × 10 in (76 mm × 254 mm) dimension lumber. In all the as-built drawings considered, the retaining wall in timber pile abutments were also constructed using the same dimension lumber. The bent pile cap design was consistent regardless of the span length or the number of piles used with the piles embedded a minimum of 12 inches in the concrete. Reproductions of some of the as-built drawings are provided in the Appendix.

The general structural details outlined above were adopted in developing various analytical models throughout this research study. The overall design of timber pile bridges is relatively straight forward and uniform. As discussed in more detail below, the simple design, susceptibility to various forms of environmental deterioration, and the lack of redundancy mean many timber pile bridges are critically vulnerable to unanticipated loading scenarios.

2.1.2 Pile Design

Timber is naturally an orthotropic, defect-filled material. Its strength depends on the direction of loading with respect to the direction of the annular rings and naturally occurring defects such as knots, grain distortions, and inconsistencies in specific gravity all contribute to high variability in material properties. Timber behavior also varies by wood species and is sensitive to various environmental factors. Inconsistencies in material behavior and member size can be a source of uncertainty in timber structures (Mansour 1990; Brites et al. 2013). However, considering the cost-to-strength ratio and the fact that they are relatively easily replaceable, timber is an extremely valuable alternative for not just light-frame residential structures but also heavy structures such as bridges, transmission structures, and marine structures. A concise review of both historical and current timber pile design methods is provided below.

2.1.2.1 Structural Capacity

Works by Chellis (1944, 1961) offer one of the earliest and most comprehensive guidelines for the design of timber pile foundations. Chellis (1944) recommends the following formula from the Wood Handbook published in 1935 by the Forest Products Library for determining the load capacity of timber piles extending above ground support:

$$R = Ap \qquad \text{when } l/d \leq 11 \tag{2.1}$$

$$R = Ap\left[1 - 0.33\left(\frac{l}{Kd}\right)^4\right] \qquad \text{when } 11 < l/d < K \tag{2.2}$$

$$R = 0.274\frac{AE}{(l/d)^2} \qquad \text{when } l/d \geq K \tag{2.3}$$

where, R is the safe load capacity, A is the pile cross-sectional area at the 1/3 point of the unsupported height, E is the timber elastic modulus, p is the allowable unit compression parallel to grain, l is the unsupported height, d is the dimension of an equivalent square column based on the pile diameter at the 1/3 point of the unsupported height, and $K = 0.64\sqrt{E/p}$. It should be noted that current versions of the Wood Handbook do not include these provisions.

Timber piles have traditionally been designed for maximum working loads between 15 tons (133 kN) to 25 tons (222 kN) depending on the species and size of the pile (Chellis 1961; Wilkinson 1968). This is in agreement with the values specified in the as-built drawings discussed in the previous section. It was not until the 1950's that timber pile design standards and allowable stress values began being established (AFPA 2005). Funded by the American Society for Testing Materials (ASTM), the Forest Products Laboratory carried out a comprehensive testing program for establishing reference allowable stresses for round timber piles and standard test methods (Erickson & Wood 1960; Lumsden 1961). The findings presented in the final report titled *Strength and Related Properties of Wood Poles* by Wood et al. (1960) were adopted in what is now known as ASTM Standards D25, and D2899. ASTM D25 provides guidelines for the selection of timber piles based on physical characteristics such as size and straightness while ASTM D2899 outlines procedures for determining the allowable stresses in round timber piles (ASTM 2017a; ASTM 2017b). These standards are adopted by design standards including the National Design Specifications (NDS) for Wood Construction (AFPA 2005), and the AASHTO (American Association of State Highway and Transportation Officials) LRFD (Load and Resistance Factor Design) Bridge Design Specifications (AASHTO 2012).

Despite efforts made to adopt LRFD principles in timber design, allowable stress design (ASD) approach is most commonly adopted in the design of timber bridge structures (Groenier

2006; Timber Piling Council 2016). The standard design procedure for computing the allowable stresses in timber piles consists of applying a series of adjustment factors to the reference timber strength. The reference design values for several wood species are provided in the NDS (AFPA 2005). The AASHTO LRFD Bridge Design Specifications specifies four species for use as piles: Pacific Coast Douglas Fir, Red Oak, Red Pine, and Southern Pine (AASHTO 2012). All timber piles tested in this study were of the Red Oak variety. Table 2.1 summarizes the timber pile design equations specified in the NDS. Design provisions in the NDS and the AASHTO LRFD Bridge Design Specifications closely mirror each other.

Table 2.1 NDS design equations for round timber piles and poles (AFPA 2005)

		ASD Adjustment Factors							
		Load Duration	Temperature	Untreated	Size	Column Stability	Critical Section	Bearing Area	Single Pile
$F_c' = F_c$	×	C_d	C_t	C_u	-	C_P	C_{cs}	-	C_{sp}
$F_b' = F_b$	×	C_d	C_t	C_u	C_F	-	-	-	C_{sp}
$F_v' = F_v$	×	C_d	C_t	C_u	-	-	-	-	-
$F_{c\perp}' = F_{c\perp}$	×	C_d	C_t	C_u	-	-	-	C_b	-
$E' = E$	×	-	C_t	-	-	-	-	-	-
$E_{\min}' = E_{min}$	×	-	C_t	-	-	-	-	-	-

F_c, F_b, F_v, and $F_{c\perp}$ denote the reference design strength values in compression parallel to grain, bending, shear parallel to grain, and compression perpendicular to grain, respectively. E and E_{min} are reference elastic moduli. E_{min} is used for beam and column stability calculations. The prime designation signifies the adjusted allowable stress for each design value. The adjustment factors account for a variety of different conditions including load duration, exposure conditions, and unbraced pile lengths. Detailed descriptions of each factor are provided in the NDS. For a pile of given size, the minimum required timber pile capacity can be used to calculate the demand which can be compared to the allowable stress computed using the equations in Table 2.1 to determine the structural adequacy of timber piles.

Timber pile bents have traditionally been only provisioned for vertical loading (Shama et al. 2007). As such, they may be vulnerable to lateral loading and combined axial-flexural loading (P-M interaction). The guidelines provided in Chellis (1944, 1961) include brief discussion on eccentric loading in piles. While it is recommended that piles subjected to axial loads and bending satisfy P-M interaction requirements, such considerations were typically neglected in the design of timber pile bridges under the assumptions that bending loads are generally small enough and result in no net tension, and that the superstructure provides sufficient rigidity to prevent eccentricity in piles (Borello et al. 2010). This research in fact has its roots in the failure of a timber pile bridge due to the negligence of P-M interaction. Borello et al. (2010) carried out a comprehensive investigation of a collapsed timber pile bridge and experimentally showed that the capacity of an eccentrically loaded timber pile can be up to 60% lower than that of concentrically loaded pile. Although P-M interaction equations for timber columns were developed early by Newlin (1940) and Wood (1950), they were not adopted in timber bridge design under the assumption that the superstructure is sufficiently rigid to preclude eccentric loading (Borello et al. 2010). However, in many timber pile bridges, the deck is simply-supported as discussed in Section 2.1. This was also the case in the failed bridge investigated by Borello et al. (2010). Both the NDS and the AASHTO LRFD Bridge Design Specifications require timber members subjected to combined flexure and compression parallel to grain to satisfy P-M interaction equations.

2.1.2.2 Geotechnical Capacity

Timber piles fall into two distinct categories: those in which the tip bears on a solid layer of soil or rock, and those that depend largely on skin friction for support. Piles in the first case are designed as columns while friction piles have mainly been designed using pile driving formulas or empirical data (AFPA 2005). Hannigan et al. (2016) states timber piles are best suited for carrying modest loads as friction piles. In the US, this has historically been the case with the Engineering-News (EN) formula being used most widely to determine the geotechnical capacity (Graham 1996). Developed by Arthur Mellen Wellington and introduced in the 1888 edition of the Engineering News, the EN formula is a simplified representation of pile-soil interaction which is an extremely complex phenomenon. It is built on the assumption that the ultimate carrying capacity of a driven pile is equal to the dynamic driving force (Chellis 1961). The EN formula takes the form:

$$Safe\ Load = \frac{2WH}{s+1} \tag{2.4}$$

where, W is the weight of the hammer in pounds, H is the drop height in feet, and s is the pile penetration per blow in inches. One of the problems with the EN formula is its inconsistency (Chellis 1961). Poulos & Davis (1980) specifically points out that the EN formula has been shown to be unreliable as it yields safety factors with an excessively wide range. Agerschou (1962) statistically compared the results from 171 pile load tests of which 25 were timber to capacity estimated using the EN formula and determined that the EN formula yields highly inaccurate results.

Despite this, the EN formula is still used to estimate the capacity of timber piles. However, most agencies and DOT’s have adopted more accurate methods for determining the geotechnical capacity (AWPI 2002). The American Wood Preservers Institute (AWPI) highlights five methods for determining the static axial load capacity of timber piles: the Meyerhof Method and the Nordlund Method for cohesionless soils, the Alpha (α) Method and the Effective Stress Method for cohesive soils, and the Nottingham Schmertmann Method when cone penetration test (CPT) data is available (AWPI 2002). These methods are discussed in detail in both the AASHTO LRFD Bridge Design Specifications and “Design and Construction of Driven Pile Foundations” published by the FHWA (AASHTO 2012; Hannigan et al. 2016).

2.2 DETERIORATION OF TIMBER PILES

Sources in the literature agree that timber piles permanently situated below the water table have indefinite service life. However, environmental and biological degradation are a major concern especially when the pile is exposed above the water table and subjected to wet and dry cycles (Hannigan et al. 2016; AWPI 2002; Tomlinson & Woodward 2008). Although preservative treatments are mandatory for bridge timber piles, their effectiveness depends on the degree of penetration and retention. Depending on the species and source, it may be difficult to achieve full penetration to the very core of the timber which leaves it highly vulnerable to various biological deterioration mechanisms (Ritter 1990). Accurately identifying the type and extent of damage in timber piles is critical for estimating the load carrying capacity of timber pile bridges.

2.2.1 Biological Deterioration

Biological deterioration of timber can occur in two forms: decay, and animal or insect attack. The decay of timber piles is caused by fungi which break down the cellular structure. The fungi use the wood as a food source and require the combination of moisture, temperature, and air (Chellis 1961). Brown rot fungi, and white rot fungi are the two most critical sources of decay (Ritter 1990). Wood affected by brown rot is brown in color as the name suggests and becomes brittle with cross-grain checks, resembling heavily charred timber. Wood affected by white rot is white or light tan in color with dark streaks and becomes soft (Highley & Scheffer 1989). Decay due to both brown rot and white rot fungi result in significant weight loss and strength loss (Chellis 1961; Ritter 1990). The work by Wilcox (1978) provides a comprehensive review of research studies that have correlated decay to timber strength. Wilcox (1978) notes decay is commonly associated with weight loss to indicate the severity and that bending strength under impact is the most critically affected characteristics. A weight loss of 6% caused by white rot reduces the impact bending strength by approximately 50% while brown rot leads to a reduction between 62% and 72%. The modulus of rupture can also be significantly affected with reductions of up to 27% and 61% for 6% weight loss caused white and brown rot respectively (Wilcox 1978). The loss of strength and energy absorption characteristics resulting from decay have critical implications for the performance of timber bridges in not only extreme loading scenarios but also everyday service.

Compared to problems caused by decay, damage due to insects is less common and generally less destructive (Highley & Scheffer 1989). Insects can create tunnels and cavities in the wood that may reduce the stiffness and load carrying capacity of timber structures. Six different species of insects are known to cause damage to wood: termites, beetles, bees, wasps, and ants (Ritter 1990). The range of termite virtually covers the entire continental US but most termites and beetles will only attack live trees, freshly cut wood or untreated wood. Carpenter ants are common and often difficult to control but are more of a nuisance than a source of structural problems (Fisette 2002). For timber structures in salt or brackish waters, marine borers such as shipworms or gribbles can cause significant damage. Some marine borers such as the *L. tripunctata* can even attack creosote treated wood (Ritter 1990).

2.2.2 Physical Deterioration

The list of factors that can cause physical deterioration of timber bridge components is endless. Some of the more prominent sources reported in the literature include mechanical abrasion, impact damage and ultraviolet (UV) light (Ritter 1990). In timber piles, these deterioration mechanisms typically damage the exterior preservative barrier, leaving the interior of the pile cross-section open to biological deterioration (Dahlberg et al. 2012). UV light breaks down the lignin, a complex organic polymer that gives wood strength, and causes discoloration. However, the effect of UV light does not penetrate deep into timber and it does not have a significant impact on the strength its strength (Ritter 1990). Overloading and wet-dry cycles can also be problematic for timber piles. Frequent or long-term overloading can lead to localized compression failure such as splitting or mushrooming as well as lead to settlement (Dahlberg et al. 2012). Wet-dry cycles can cause checking and splitting of the wood fibers which increase the susceptibility to decay (Chow et al. 1986).

2.2.3 Detection of Timber Deterioration

Deterioration of timber can be difficult to detect, particularly at early stages or when the defect is more than several millimeters below the surface (Ross et al. 2004). Some traditional methods for detecting internal decay include sounding, probing, and boring (Highley & Sheffer

1989; Ritter 1990). These methods are subjective and depend highly on the inspector’s familiarity and understanding of wood deterioration mechanisms. The *Wood and Timber Condition Assessment Manual* prepared by the Forest Products Library (FPL) provides detailed information on the state-of-the-art in timber inspection (Ross et al 2004). Today, there are two nondestructive inspection methods that can be used to accurately locate deteriorated regions in timber and estimate the extent of the problem.

The first is a resistance drill which uses a very small drill bit to drill through the timber and measure the resistance of the wood. The method is based on the premise that decayed wood is softer and offers less resistance to the drill (Ross et al. 2004). While resistance drilling has been shown to be effective at determining whether there is decay in various timber components, it is difficult to use it to obtain a clear picture of the extent of deterioration because the amount of drilling required to obtain a three-dimensional image would be prohibitive. Figure 2.4 shows the resistance drill being used to inspect a bridge timber pile and the output data.

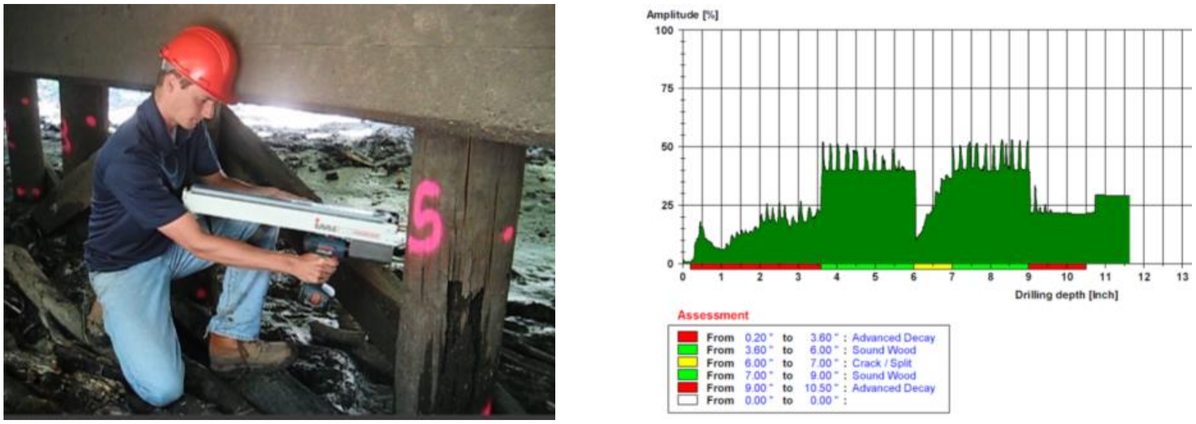

a) **b)**

Figure 2.4 Timber pile inspection using a resistance drill **a)** Application **b)** Output data

Another nondestructive inspection method becoming popular for timber structure applications is stress wave timing (SWT). SWT is a method where decay and other damages can be detected by measuring the velocity at which stress waves propagates through a material. SWT is commonly used to assess the condition of heavy timber as well as live trees (Wang et al. 2004). It is based on the principle that stress waves propagate rapidly through stiff, solid materials and more slowly through soft, flexible materials. The fundamental concept behind the SWT method is illustrated in Figure 2.5.

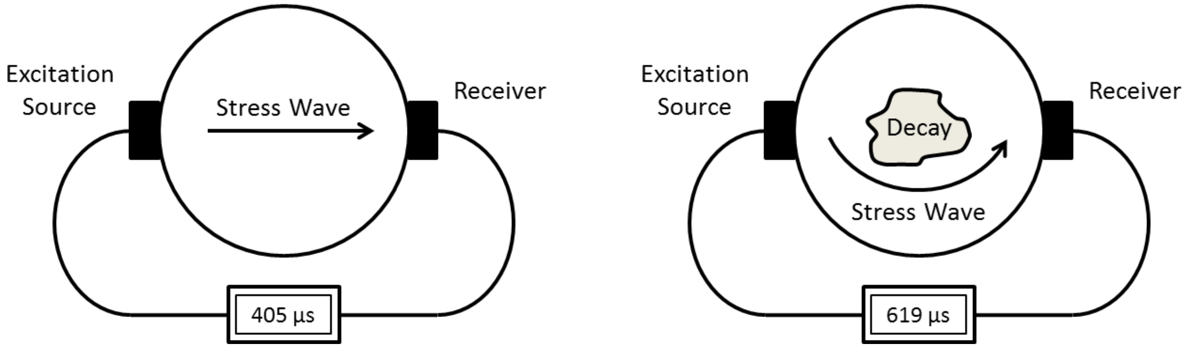

Figure 2.5 Stress wave timing concept

As illustrated in Figure 2.5, stress waves are induced on one side of a specimen by using an ultrasonic excitation source or by impacting the specimen and the time it takes for the stress wave to be detected by a receiver at a known distance away from the source is measured. The size of a defect that can be detected using ultrasonic waves is directly proportional to the frequency. Higher frequency stress waves can be used to identify fine defects but they will attenuate more rapidly. Emerson (1999) notes that 100 kHz to 200 kHz is the upper range for using ultrasonic waves to inspect timber. Typical stress wave transmission times through timber vary depending on the species, grain direction, and moisture content. Table 2.2 summarizes stress wave transmission time reference values obtained from Wang et al. (2004) for undeteriorated Red Oak.

Table 2.2 Stress wave transmission times through undeteriorated Red Oak (Wang et al. 2004)

Reference	**Moisture Content (%)**	**Stress Wave Transmission Time - µs/m (µs/ft)**	
		Parallel to Grain	**Perpendicular to Grain**
Smulski (1991)	11	262 – 200 (80 – 61)	-
Armstrong et al. (1991)	4 – 6	226 – 177 (69 – 54)	646 – 571 (197 – 174)
Jung (1979)	12	302 – 226 (92 – 69)	-
Ross et al. (1994)	Green	-	795 (242)

Due to the unique microstructure of wood, the stress wave velocity varies greatly depending on the direction of measurement and data can be collected in two ways. Firstly, measurements taken across the cross-section in directions tangent and perpendicular to the grain can be used to pinpoint defects and obtain a detailed description of internal deterioration. Wipf et al. (2007) used a simultaneous iterative reconstruction technique (SIRT) to post-process SWT data and generate tomographic images of artificially damaged timber pile sections as shown in Figure 2.6.

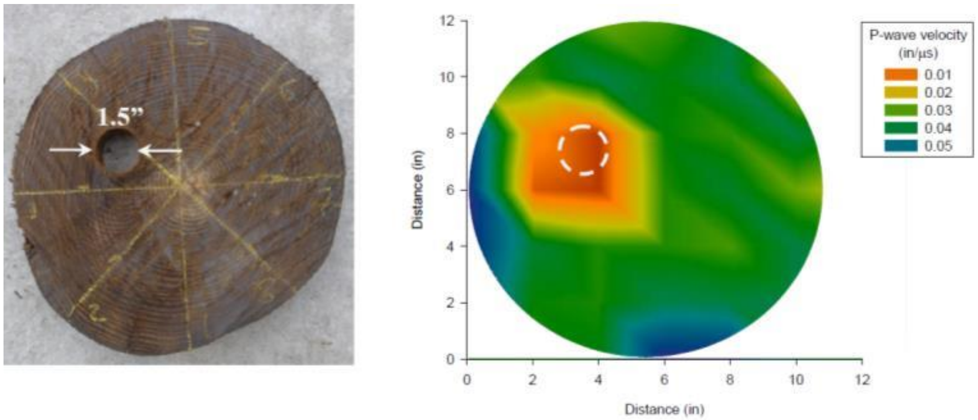

Figure 2.6 Tomographic images of artificial timber deterioration generated based on cross-sectional SWT measurements (Wipf et al. 2007)

Although this approach can accurately describe the extent and severity of deterioration in timber, a large number of sampling points is needed to generate accurate images of the cross-section. Divos and Szalai (2002) showed that the minimum size of an internal defect that can be detected using six cross-sectional measurements is approximately 8% of the cross-sectional area.

A second way to employ SWT to inspect timber piles is to take measurements in the longitudinal direction parallel to the grain. This method offers a more direct representation of the structural condition of timber piles. Using one-dimensional wave theory, stress wave velocity in the longitudinal direction can be related to the dynamic elastic modulus of a material as follows (Kim et al. 2000):

$$c = \sqrt{E_d/\rho} \tag{2.5}$$

Where, c is the stress wave velocity, E_d is the dynamic elastic modulus, and ρ is the material density. The dynamic elastic modulus is a property of a material under vibratory conditions. Although it is not possible to obtain a perfectly accurate predictions of the strength or behavior of wood solely from stress wave transmission characteristics but studies have shown that the speed and attenuation of stress waves through timber is a reliable indicator of its overall condition and are strongly related to the mechanical properties (Ross & Pellerin 1994; Ross et al. 1997).

2.3 RETROFIT OF TIMBER PILES

Several different methods have been developed over the years for strengthening or retrofitting timber piles. For timber pile bridges, posting has traditionally been the most widely used method because it is cheap and easy to implement. Posting consists of simply cutting away the deteriorated sections of a pile and splicing a new timber segment to the existing pile using steel drift pins or nails (Fanous et al. 2003). However, since the connections have no moment capacity, posting can have catastrophic consequences, especially if the piles are subjected to bending moment in addition to axial loads (Borello et al. 2009). Grout or epoxy injection has also been proposed as a cost effective and durable repair option for timber piles (Avent 1989; Emerson 2004). While grout or epoxy injection can effectively fill gaps and large voids due to decay, it still leaves a large portion of the timber exposed. Furthermore, as shown by Emerson (Emerson 2004) epoxy injection is less effective without additional confinement. Reinforced concrete jacketing is another retrofitting technique that can be used on timber piles (Department of the Army 1985; Dahlberg et al. 2012). However, it requires significantly more labor and drastically increases the pile diameter. Examples of timber pile repair using posting, epoxy injection, and concrete jacketing techniques are shown in Figure 2.7.


a) **b)** **c)**

Figure 2.7 Timber pile repair techniques **a)** Posting **b)** Epoxy injection (Emerson 2004) **c)** Concrete jacketing (Dahlberg et al. 2012)

Fiber reinforced polymer (FRP) composites have gained popularity in structural engineering applications because they do not corrode and offer a high strength-to-weight ratio.

While the performance of FRP retrofitted concrete members has been studied extensively (Mirmiran & Shahawy 1997; Xiao & Wu 2000; among others), FRP composites have also been used in timber structures to a lesser degree in a variety of applications including bridges, railroad sleepers, marine structures, and transmission towers. Experiments by Najm et al. (2007) on circular poplar wood specimens showed that confinement with carbon-FRP (CFRP) significantly improved their performance under axial loads leading to increased stiffness, strength, and deformation capacity. Najm et al. (2007) also found fully wrapping timber column specimens reduced the variability in timber behavior. When used as flexural reinforcement in timber beams, FRP composites provided improved strength, stiffness and ductility (Plevris & Triantafillou 1992; Johns & Lacroix 2000). Others have investigated using a combination of grout or mortar shell and FRP composites to reinforce heavily deteriorated timber piles (Hagos 2001; Lopez-Anido et al. 2003; Caiza et al. 2012).

Currently, unified specifications or standards do not exist for designing FRP retrofits for timber piles. The study by Caiza et al. (2012) offers a simplified design equation for designing full FRP wraps for round timber piles. The approach is based on the premise of providing adequate FRP reinforcement to restore the flexural stiffness of a deteriorated timber pile to that of sound timber. The method neglects the tensile strength of timber. The number of FRP layers required, n, is calculated as

$$n = \frac{D}{2t}\left(\left(1 + \left(1 - \frac{I_{comp}}{I}\right)\frac{E_{timber}}{E_{FRP}}\right)^{\frac{1}{4}} - 1\right) \tag{2.6}$$

where, *D* is the timber pile diameter, *t* is the thickness of a single layer of FRP composite, *I* is the moment of inertia of the complete timber pile section, I_{comp} is the effective moment of inertia of the timber pile section neglecting timber tensile strength, and E_{timber} and E_{FRP} are the Young's moduli for the timber pile and FRP composite, respectively. Caiza et al. (2012) tested several Red Oak timber pile specimens in flexure-compression to determine their elastic moduli then used Equation (2.6) to determine the FRP thickness necessary to retrofit them.

FRP composites show promise as a retrofitting alternative for timber piles and guidelines for their use would be extremely valuable. However, its effectiveness may depend on several factors affecting the timber substrate since there are so many uncertainties in timber as a material itself. This includes variability in timber strength and the effect of deterioration. Therefore, in order to develop FRP retrofits that are effective, it may be necessary to establish a good understanding of the existing condition of the in-situ timber pile.

2.4 SEISMIC PERFORMANCE OF TIMBER BRIDGES

2.4.1 Performance in Past Earthquakes

Compared to concrete or steel bridge structures, there is very little information available in the literature on the seismic performance of timber bridges. The report by Kachadoorian (1968) on the Alaskan highway system following the 1964 Alaska Earthquake is the only record in the literature that documented the timber bridge damage in an earthquake. The survey by Kachadoorian (1968) noted that only four of 20 bridges with timber sub and superstructures were severely damaged or destroyed while 22 of 27 bridges with timber substructure and concrete superstructure were severely damaged or destroyed. Kachadoorian (1968) attributed most of the damage to soil amplification effects and liquefaction with the substructure-superstructure connection details being the most critical components. No other account of timber pile bridge performance in past earthquakes was found in the literature.

2.4.2 Seismic Design of Timber Bridges

As discussed above, traditional timber pile bridge design was simplified with some aspects based on convention or experience rather than mechanistic approaches. Furthermore, most timber pile bridges were provisioned for gravity loads only with no explicit consideration for lateral loads. Therefore, timber pile bridges are ill-equipped to resist extreme ground shaking. The manual titled *Timber Bridges: Design, Construction, Inspection, and Maintenance* published by the US Department of Agriculture offers the most complete overview of practices in timber bridges and suggests the Equivalent Static Force Method is the most appropriate method of analysis for timber bridges (Ritter 1990). The Equivalent Static Force Method as outlined in the 1983 AASHTO Standard Specifications for Highway Bridges consists of applying an equivalent static horizontal force at the structure's center of mass. The equivalent static force is determined based on the structure type, self-weight, fundamental period, and a site specific response coefficient (Ritter 1990). This approach, however, is no longer current. Shama et al. (2007) further note that since many timber highway bridges are short and consist of a single span or multiple simply-supported spans, the design requirements would have been limited to checking connection force and displacement.

Current seismic design specifications are maintained by AASHTO in the LRFD Bridge Design Specifications (2012) and the Guide Specifications for LRFD Seismic Bridge Design (2011). For multispan bridges, the seismic design procedure in these standards begins with the identification of the seismic zone which depends on the location, soil type, and operational importance of the bridge. Since most timber pile bridges do not fit the bill of essential or critical infrastructure and meet the definition of a "regular" bridge as described by AASHTO, more simplified analysis methods are sufficient. Although the standards have specific requirements for concrete and steel structures, no special provisions are given for timber bridges. Bridges with a single span, which is the case for many timber bridges, are not subject to seismic analysis regardless of seismic zone.

2.4.3 Work by Shama et al. (2007)

The most comprehensive research study on the seismic performance of timber bridges is presented in the report written by Shama et al. (2007). The literature review conducted by the authors includes a section on an experimental study conducted at the University of British Columbia (UBC) on the seismic performance of Douglas fir timber piles used to support heavy-duty electrical transformers. Although a copy of the report detailing the experiments and results could not be found, some key findings highlighted by Shama et al. (2007) include:

- Moisture content and creosote treatment did not affect pile behavior.
- Douglas fir timber piles can withstand horizontal displacements of up to 1 m.
- Given that deflections at failure were approximately double that at the linear elastic limit, it is reasonable to include inelasticity in the design of timber piles under lateral loading.
- In a laterally loaded timber pile, a plastic hinge develops at or in the immediately below the concrete pile cap and the plastic hinge likely limits the shear and moment capacity of the pile.

In addition to a thorough literature review, the authors also carried out an extensive experimental program including quasi-static, cyclic lateral loading of single piles and model bents, as well as shaking table experiments on ¾ scale timber pile bent models. The test results showed that timber pile bents behave in a very ductile manner with performance limited by the timber bending strength and condition in unbraced bents, and timber cross bracing in braced bents. Test results from Shama et al. (2007) demonstrating the behavior of timber piles under cyclic lateral loading are shown in Figure 2.8.

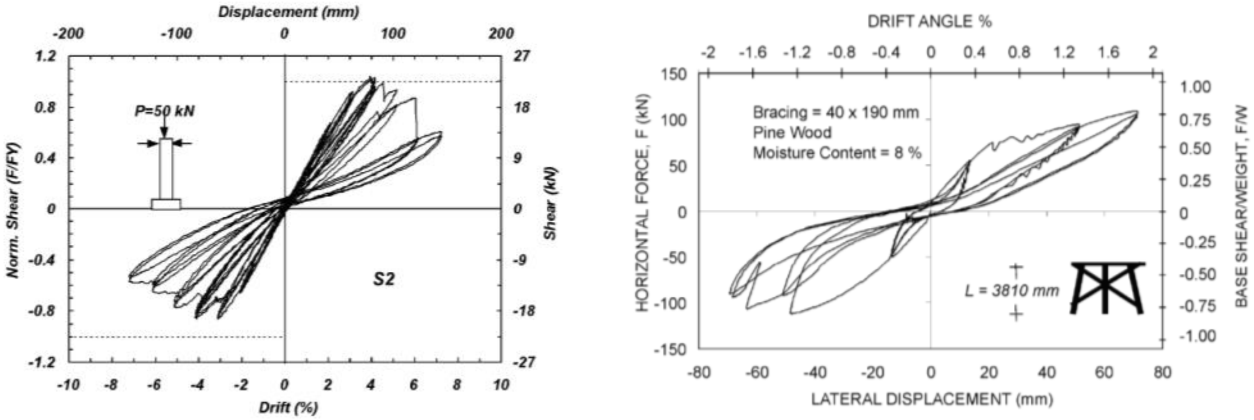

a) **b)**

Figure 2.8 Behavior of timber piles under cyclic lateral loading **a)** Single pile **b)** ¾ scale timber pile bent (Shama et al. 2007)

Shama et al. (2007) also developed analytical models for timber pile behavior that are relevant and valuable to the current study. This includes energy dissipation characteristics, a rotational spring model for modeling timber pile-concrete pile cap joints, and a trilinear force-displacement relationship for collectively modeling the behavior of timber cross bracing and connector elements. Shama et al. (2007) adopted the concrete material model developed by Mander et al. (1988) to describe the behavior of timber in their numerical simulations and found the results to be quite satisfactory. Since both timber and concrete behave nonlinearly in compression and in a brittle, linear elastic manner in tension, the concrete model can provide good predictions of timber behavior.

Lastly, Shama et al. (2007) also studied the seismic fragility of timber pile bents using information obtained from experimental testing and numerical modeling. It is shown that timber pile bridges with concrete superstructure, which is the principal focus of the current study, is more susceptible to damage in earthquakes than those with timber superstructure. Furthermore, fragility curves derived based on lateral cyclic loading tests on round Douglas fir timber piles showed that deteriorated piles with substantial splitting are considerably more likely to fail under seismic excitation than timber piles in good condition.

2.5 TSUNAMI LOADING

The consideration of tsunami-induced loads on structures is a relatively new development that was largely brought on in the aftermath of the 2004 Indian Ocean Tsunami, and more recently the 2011 Great East Japan Tsunami. This section contains a short overview of the state-of-the-art in the analysis of tsunami hazards as it pertains to bridge structures. There was no information in the literature that specifically focuses on timber bridges.

2.5.1. Tsunami Performance of Bridges

Several reports and journal publications detailing observations from post-disaster surveys following the 2004 Indian Ocean Tsunami and 2011 Great East Japan Tsunami are available in the literature (Ghobarah et al. 2006; Chock et al. 2013; Kawashima & Buckle 2013 among others). At least 150 highway bridges were damaged as a direct result of tsunami inundation in the 2011 tsunami (Kawashima & Buckle 2013). Most bridges in the 2011 tsunami survived the earthquake but were completely destroyed by the tsunami which shows that seismic design provisions do not provide sufficient capacity for tsunami forces (Yim et al. 2014). The most common bridge failure mode observed in these events was unseating of the deck. Chock et al. (2013) documented instances of reinforced concrete substructure failure in which a plastic hinge had formed at the base. Unlike earthquake loading, tsunami loads are sustained forces with long period cycles of flow (Chock 2016). Since a bridge superstructure represents a very large contact area for tsunami impact, high, sustained lateral loads can be imposed on substructure components. This can be especially problematic for timber pile substructure given their low strength. Tsunamis also generate debris fields which can carry massive objects such as vehicles, boats, and shipping containers inland. Debris can cause damage to structures by not only through the impact itself but also by restricting the water flow and creating a dam (Chock et al. 2013).

2.5.2 ASCE 7-16

Prior to the introduction of the chapter on tsunami loads and effects in the 2016 revision of ASCE 7 *Minimum Design Loads for Buildings and Other Structures* (ASCE/SEI 2017), the only guidelines available for tsunami resistant structural design was in FEMA P-646 *Guidelines for Design of Structures for Vertical Evacuation from Tsunamis* (FEMA 2012). Similar to seismic design, tsunami design is based on probabilistic analyses of tsunami hazards which were used to develop offshore tsunami amplitude maps and tsunami design zone inundation maps for Alaska, Washington, Oregon, California, and Hawaii (Chock 2016). These maps provide the basis for determining the inundation depth and flow velocity at a site which can be done using Energy Grade Line Analysis or a site-specific two-dimensional inundation analysis.

For structural design, the principal tsunami forces and effects, F_{TSU}, must be considered in two load combinations:

$$0.9D + F_{TSU} + H_{TSU} \tag{2.7}$$

$$1.2D + F_{TSU} + 0.5L + 0.2S + H_{TSU} \tag{2.8}$$

where, D, L and S are the dead, live and snow loads respectively, and H_{TSU} is the load due to tsunami-induced lateral foundation pressures developed under submerged conditions. Both tsunami inflow and outflow must be considered for F_{TSU}, and if the net effect of H_{TSU} counteracts the principal load effect, the load factor for H_{TSU} is taken to be 0.9 (ASCE/SEI 2017).

There are four main load effects that must be considered:

- Hydrostatic loads – buoyancy, unbalanced lateral hydrostatic force, residual water surcharge loads on floors and walls, and hydrostatic surcharge pressure on foundation.
- Hydrodynamic loads – drag force, and hydrodynamic pressure.
- Debris impact
- Scour

Chock (2016) provides detailed descriptions of each load effect. In the case of a bridge structure, it can be expected that there will be significant lateral hydrodynamic loads applied to columns and piers as well as high uplift forces on the deck. Scour effects including localized scour, erosion, and soil pore pressure softening may also be critical especially for substructure such as timber pile bents.

2.5.3 Numerical Modeling of Fluid-Structure Interaction (FSI)

Fluid-structure interaction is a topic that has been a growing rapidly within structural engineering in light of tsunami hazards but also due in large part to hurricane events. A wide range of numerical techniques have been developed and used for FSI simulations Researchers have developed and used a wide range of numerical methods for FSI simulations. Traditionally, the arbitrary Lagrangian-Eulerian (ALE) formulation has been the most widely used. Several studies in the literature have used ALE methods to numerically simulate the impact of tsunami waves on bridge structures (Yeom 2009; Azadbakht & Yim 2014; Yim et al. 2014). Issues with ALE simulations of FSI problems are well-documented and include numerical complexities in the Eulerian formulation, the need for a coupling algorithm between Lagrangian and Eulerian domains, and the inability to track the free surface of the fluid.

Apart from ALE, two unique numerical methods stand out in the literature for modeling structural response under tsunami impact: the smoothed particle hydrodynamics (SPH) method, and the particle finite element method (PFEM). SPH is a meshfree Lagrangian method initially developed to model astrophysical problems. The problem domain is discretized into a set of arbitrarily distributed particles and the vector function of a particle is approximated over a “smoothing kernel” by considering the influence of the neighboring particles. Adapting the SPH method to FSI problems requires a series of rather complex numerical approximations. Researchers have demonstrated the effectiveness and accuracy of SPH in simulating tsunami impact on structures but problems considered in the literature only involve simple, solitary columns (St-Germain et al. 2012; Wei et al. 2015). However, the numerical complexity and the lack of infrastructure that can facilitate more complex structural systems limit the applicability of the SPH method for structural engineering problems.

PFEM is also a Lagrangian method that has gained considerable attention over the past decade for its simplicity and versatility. The main strength of PFEM comes from the fact that the Lagrangian formulation is used for both the fluid and structural domains. Unlike the SPH method, however, a mesh is used to connect the discrete particles. The purely Lagrangian formulation offers several functional and numerical advantages over traditional methods used for FSI problems such as the Arbitrary Lagrangian-Eulerian (ALE) method. One important advantage is that convective terms which present numerical difficulties in Eulerian fluid formulations disappear. The fully Lagrangian formulation also allows for easy tracking of fluid boundaries and facilitates intuitive coupling at fluid-structure interfaces that is a natural extension of conventional finite element method computations (Oñate et al. 2004; Idelsohn et al. 2006). The tradeoff, however, is in the need to continuously regenerate a mesh to cope with extreme deformations. Nevertheless, with many efficient algorithms and computational resources available, the demand in computational effort is not a significant deterrent to using PFEM even for large FSI problems. The key idea behind a PFEM simulation is illustrated in Figure 2.9.

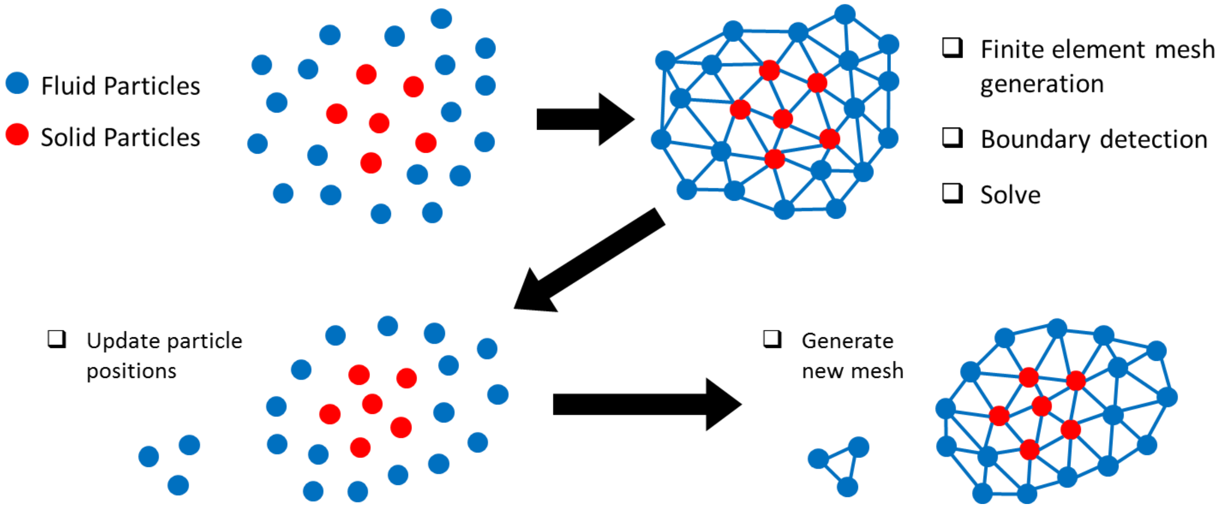

Figure 2.9 Typical solution step in PFEM

The accuracy of PFEM in solving FSI problems has already been demonstrated in numerous different studies. As part of this research, a novel PFEM analysis code was initially developed to examine the feasibility of using it to simulate earthquake-tsunami response. The development of the PFEM code is discussed in Chapter 6. PFEM has since been implemented into the OpenSees (Open System for Earthquake Engineering Simulations) framework by Zhu & Scott (2014b).

CHAPTER 3

LONG-TERM PERFORMANCE OF FRP STRENGTHENED TIMBER PILES

Several research studies have already shown that confining timber piles with FRP composites can improve their stiffness and strength (Hagos 2001; Lopez-Anido et al. 2003; Najm et al. 2007; Caiza et al. 2012). Despite the proven effectiveness of FRP composite retrofits, they are still not widely used in retrofitting timber structures. One area in which little research effort has been made is the long-term performance of FRP strengthened structures. This chapter investigates the effectiveness of FRP wrapping in strengthening and protecting timber bridge piles after being subjected to environmental degradation. One of the main difficulties in conducting a study of this nature is obviously the amount of time required for the degradation to take place. To overcome this, an accelerated aging procedure was used to artificially induce degradation that would naturally occur over years of exposure in the field. Results show that accelerated aging induces significant deterioration in unretrofitted timber piles but the effects are relatively minor in the FRP wrapped specimens. It is also proven that fully confining timber piles with FRP composites can significantly improve their peak stress and ductility even after being subjected to extreme degradation.

3.1 TEST SPECIMENS

3.1.1 Timber Piles

Since this study is aimed at investigating existing timber piles that are in need of rehabilitation, it was essential to use specimens from piles that have been in service for considerable amount of time. The specimens used in this study were cut from eight field-extracted Red Oak piles from a bridge in Illinois. Red Oak is a common species of wood used in many heavy timber applications including piles and railroad sleepers. Heavy timber structures are generally designed based on allowable stress. Reference design values for Red Oak listed in the National Design Specification for Wood Construction (NDS) are given in Table 3.1. F_c is the allowable compressive stress parallel to the grain, F_b is the allowable bending stress, F_v is the allowable shear stress parallel to the grain, E is the reference modulus of elasticity, and E_{min} is the reference modulus of elasticity used for beam and column stability calculations.

Table 3.1 Reference design values for treated Red Oak timber piles under normal load duration and wet service conditions (AFPA 2005)

F_c (MPa)	F_b (MPa)	F_v (MPa)	E (MPa)	E_{min} (MPa)
7.6	16.9	0.9	8,618	4,551

The piles used in this study ranged in diameter from 221 mm to 318 mm. While the exact age of the piles was not known, it was indicated that they were treated with creosote in 1993. Ports drilled for creosote injection were clearly visible and had been properly plugged. The piles were cut into specimens 610 mm in height. In total 24 specimens were prepared. Figure 3.1 shows typical timber specimens used in this study.

Figure 3.1 Typical Red Oak pile specimens used in the study

In general, the outside surfaces of the piles showed signs of moderate weathering. Splitting ranging from a few millimeters wide up to a centimeter was noted throughout the specimens both along grain boundaries and across grains. Inspection of the specimen cross-sections revealed that although the overall level of creosote retention was high, in some specimens it had not fully penetrated to the core. Moderate to severe decay was observed in some piles which had led to section loss. The decay was typically limited to localized areas affecting only a few individual specimens. The moisture content of the specimens was determined through oven drying to be between 11 and 14%.

3.1.2 FRP Wrapping

FRP retrofitting in the field can be done using prefabricated composite shells or using the wet layup method (Mirmiran et al. 2008). Prefabricated shells are relatively easier to implement in the field, however, they are more difficult to bond properly to the timber. Furthermore, it is difficult to fit one shell to multiple timber piles because of variations in the timber diameter. Therefore, all specimens were prepared using the wet layup method. A glass fiber reinforced polymer (GFRP) woven roving fabric was paired with three different resins were used to fabricate the FRP composite. Although the woven fabric consists of fibers in the longitudinal and transverse directions, the longitudinal fibers do not contribute to providing lateral confinement. The resins used were: 1) polyester resin 2) standard epoxy resin, and 3) epoxy resin formulated with a special moisture tolerant curing agent. The two epoxy resins had comparable characteristics. In general, epoxy resins are more expensive than polyester but offer higher strength and better bond. Material properties of the constituents are listed in Table 3.2.

Table 3.2 FRP composite material properties

GFRP Woven Roving	Thickness: 0.635 mm Density: 0.67 kg/m^3 Elastic Modulus: 124,000 MPa Ultimate Strain: 2%
Polyester Resin	Density:1.1 kg/L Tensile Strength: 55 MPa Ultimate Strain: 2.1%
Standard Epoxy Resin	Density: 1.1 kg/L Tensile Strength: 67.8 MPa Ultimate Strain: 1.9%
Moisture Tolerant Epoxy Resin	Density: 1.0 kg/L Tensile Strength: 61.4 MPa Ultimate Strain: 2.5%

Prior to applying the FRP, the surfaces of the timber piles were cleaned with wire brushes to remove any dirt and debris. The fabric was cut into sheets tailored to each specimen then wrapped around the timber and saturated with resin using rollers. Each layer was overlapped three inches at the ends with each subsequent layer being offset by 90° to ensure that the seams did not coincide. The saturated FRP was smoothed out to remove any air pockets. The FRP was allowed to cure for at least 48 hours before testing. The FRP wet layup process is illustrated in Figure 3.2.

a) **b)**

Figure 3.2 FRP wet layup process **a)** cutting the fabric **b)** resin application

Currently there are no guidelines available on designing FRP retrofits for timber piles. In the study by Caiza et al. (2012) it was determined that similar timber piles required a 6.35 mm thick (10 layers) GFRP wrap with standard epoxy resin to recover the deteriorated flexural stiffness. Caiza et al. used the same type of FRP fabric as the current study and each layer of FRP was 0.635 mm thick. In this study, 5 layers and 10 layers of FRP were considered to determine the effect of varying the FRP thickness. For the specimens fabricated with the moisture tolerant epoxy resin, wet and dry surface conditions were also considered. To simulate a wet initial pile condition, the timber was submerged under water for 48 hours and drip dried for 1 hour before applying the FRP. A summary of the test specimens is provided in Table 3.3. Each specimen is identified according to a specimen number from SP1 to SP24 followed by its resin type, number of FRP layers, and accelerated aging status. Resin type designation N represents unretrofitted timber pile specimens while P, E, and M correspond to the polyester, standard epoxy, and moisture tolerant epoxy resins, respectively. In the moisture tolerant epoxy resin specimens, the lower case letter d or w following the resin type refer to dry and wet initial surface conditions, respectively. Lastly, specimens ending in U were tested as-is without being subjected to accelerated aging while those ending in A were aged.

Table 3.3 Summary of test specimens

Resin Type	Specimen Designation	No. of FRP Layers
No FRP	SP1-NA SP2-NA SP3-NU SP4-NU	-
Polyester Resin	SP5-P5A SP6-P5A SP7-P5U	5
	SP8-P10A SP9-P10A SP10-P10U	10
Standard Epoxy Resin	SP11-E5A SP12-E5A SP13-E5U	5
	SP14-E10A SP15-E10A SP16-E10U	10
Moisture Tolerant Epoxy Resin	SP17-M5dA SP18-M5wA SP19-M5dU SP20-M5wU	5
	SP21-M10dA SP22-M10wA SP23-M10dU SP24-M10wU	10
Total Number of Specimens	24	

3.2 STRESS WAVE TIMING (SWT)

To better assess the condition of the timber pile samples before testing and determine how the initial condition of the timber affects the overall performance of the FRP retrofit, stress wave timing (SWT) was employed. The basic ideas and principles of SWT were introduced in Chapter 2. An ultrasonic pulse velocity (UPV) instrument was used to take measurements in the direction parallel to the grain. The instrument consisted of two 50 kHz piezoelectric transducers and a receiver which measured the transmission time. A gel-type couplant was applied between the transducers and the test specimen to reduce the impedance mismatch and ensure proper wave transmission into the specimen. The UPV equipment used in this study is shown in Figure 3.3 a). Measurements were taken at five equally spaced points across the cross-section in the direction parallel to the grain as shown in Figure 3.3 b).

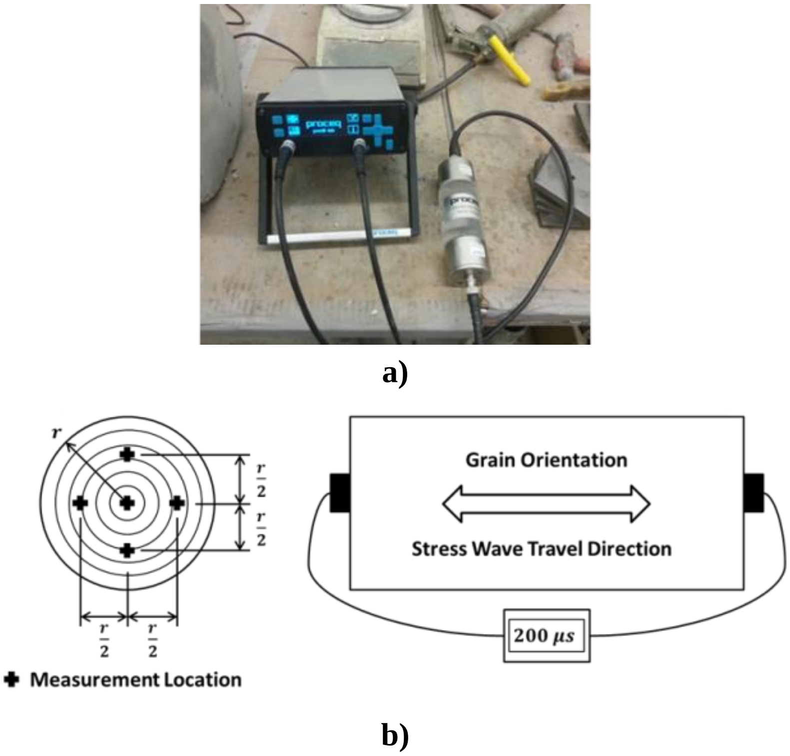

Figure 3.3 Stress wave timing parallel to grain **a)** UPV instrument **b)** schematic of test setup

As shown in Table 2.2, the reference stress wave transmission times for undeteriorated Red Oak parallel to the grain range from 177 to 302 μs/m depending on the moisture content. In total, measurements were taken on 13 specimens prior to subjecting them to accelerated aging. To evaluate the effect of accelerated aging on the stress wave transmission time, measurements were also taken after the procedure on four specimens. The average stress wave transmission times are summarized in Table 3.4.

Table 3.4 Average stress wave transmission times through timber pile specimens parallel to grain

Specimen	Average Transmission Time (μs/m)	
	Before Accelerated Aging	**After Accelerated Aging**
SP1-NA	215.6	-
SP2-NA	211.0	-
SP5-P5A	278.2	-
SP6-P5A	227.7	-
SP11-E5A	305.4	-
SP12-E5A	242.5	-
SP17-M5dA	228.7	247.0
SP18-M5wA	217.5	232.9
SP19-M5dU	228.3	-
SP21-M10dA	220.4	245.1
SP22-M10wA	222.4	247.7
SP23-M10dU	213.3	-
SP24-M10wU	222.1	-

Overall, most specimens were in good condition relative to the reference values. However, relatively high transmission times were observed in specimens SP5-P5A and SP11-E5A. These two specimens were cut from the same timber pile. When these specimens were load tested it was revealed that they were severely decayed. The data from these specimens were excluded as outliers. Measurements taken on specimens after accelerated aging showed that the aging increases the stress wave transmission time by as much as 11%, indicating the introduction of further deterioration in the timber.

Although an accurate mathematical expression does not exist for the relationship between stress wave transmission times and the mechanical properties of wood, the initial condition assessment may provide a basis on which to determine the strength of retrofit required in future applications.

3.3 ACCELERATED AGING

One of the main challenges in this study was simulating the effects of environmental degradation. Because it was not feasible to achieve this in real-time through years of actual field exposure, an accelerated aging procedure was used to artificially induce the degradation in the lab. One such procedure was developed by Chow et al. (1986) for artificially weathering Red Oak railroad sleepers. As identified by Chow et al., checking or splitting due to repeated wet-dry cycles, and decay are the principal causes of wood railroad sleeper failure. Although the loading conditions are different, these are problems common to all heavy timber structures. The accelerated aging procedure involves alternating steps of soaking, steaming, oven drying, and freezing at extreme temperatures to rapidly induce swelling and shrinkage stresses, and cause wood fiber degradation (Chow et al. 1986). These exposure conditions were shown to be effective in reducing the hardness and modulus of elasticity perpendicular to the grain. In a detailed comparison of Red Oak crossties ranging from new to more than 30 years old and those subjected to the accelerated aging procedure, it was determined that six cycles of the accelerated aging is roughly equivalent to 20 years of field exposure (Chow et al. 1987). A six cycle accelerated aging protocol similar to the one developed by Chow et al. is described in ASTM D1037-12 Standard Test Methods for Evaluating Properties of Wood-Base Fiber and Particle Panel Materials (ASTM 2012). The ASTM standard consists of similar exposure conditions but does not call for vacuum or pressurized soaking. Since it is difficult to create vacuum or pressurized conditions for large timber specimens, the ASTM procedure was used in this study. The accelerated aging procedure adopted in this study is described in Table 3.5.

Table 3.5 ASTM D 1037 accelerated aging procedure adopted in this study

Condition	Duration	Purpose
Soaking (49 ± 2℃)	1 hour	Causes swelling
Steaming (93 ± 3℃)	3 hours	Degradation of wood fibers
Freezing (-12 ± 3℃)	20 hours	Simulates winter conditions
Oven Drying (99 ± 3℃)	3 hours	Causes shrinkage and splitting
Steaming (93 ± 3℃)	3 hours	Degradation of wood fibers
Oven Drying (99 ± 3℉)	18 hours	Causes shrinkage and splitting

The setup for the accelerated aging procedure consisted of a large tank fitted with a temperature controlled water heater, a steam box fitted with a steam generator, a chest freezer, and a conventional aggregate oven as shown in Figure 3.4.

a) **b)** **c)** **d)**

Figure 3.4 Test setup for the ASTM D 1037 accelerated aging procedure adopted in this study **a)** Heated water tank **b)** Steam box with steam generator **c)** Chest freezer **d)** Aggregate drying oven

In order to prevent any moisture ingress through the ends of the pile specimens during the accelerated aging procedure, and to ensure level surfaces for load testing, a thin layer (< 5 mm) of quick-setting mortar was applied to both ends. The mortar had a specified compressive strength of 28 MPa after 24 hours. The mortar layer was not intended to be load carrying.

Visual inspection of the FRP strengthened specimens after accelerated aging revealed no significant damage to the FRP composite itself except for some discoloration due to the seepage of creosote. In the as-is timber pile specimens, splitting was more prevalent but there were no other visual signs of major deterioration. However, as shown in Table 3.4, the accelerated aging procedure led to increased stress wave transmission times in specimens SP17-M5dA, SP18-M5wA, SP21-M10dA and SP22-M10wA. This is an indication of the additional damage induced in the timber piles by the accelerated aging.

3.4 TEST RESULTS

Each specimen was tested in uniaxial compression using a 2,670 kN MTS servo-controlled machine. The testing frame was instrumented with an internal load cell and a linear variable differential transducer (LVDT). An additional 250 mm gauge extensometer was attached to the side of the specimen. The load was applied at a constant cross-head rate of 1.27 mm per minute. In total, 20 FRP wrapped specimens were tested. However, when tested under load, it was revealed that four specimens: SP5-P5A, SP8-P10A, SP11-E5A, and SP20-M5wU were severely decayed at the core which could not have been caused by the accelerated aging procedure. These specimens are not included in the discussions because they failed prematurely.

3.4.1 As-is Timber Piles

Unretrofitted timber pile specimens SP3-NU and SP4-NU were tested as-is to examine their behavior. The failure of the wood occurred in two stages: 1) splitting of the grains, and 2) crushing and buckling of the wood fibers. These failure patterns are illustrated in Figure 3.5. The stress-strain relationships observed in the unretrofitted timber specimens are shown in Figure 3.6.

Figure 3.5 Failure of unretrofitted timber specimens

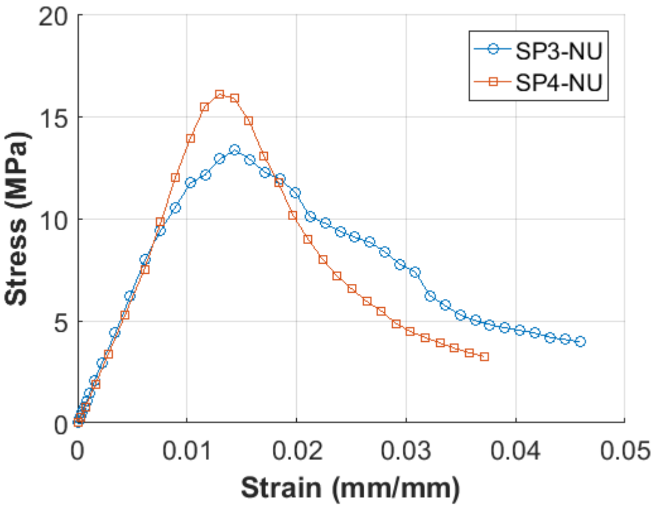

Figure 3.6 Stress-strain behavior of unretrofitted as-is timber piles

Externally, both specimens were in relatively good condition prior to the testing without extensive checking or splitting. An inspection of the failed specimens revealed no signs of internal decay. The average peak stress of specimens SP3-NU and SP4-NU was 14.7 MPa, and the average elastic modulus was 1,515 MPa. The average peak stress of the two specimens is almost two times higher than the reference design allowable compressive stress shown in Table 3.1. However, the average elastic modulus is about 65% lower than the reference elastic modulus, E_{min}.

3.4.2 FRP Retrofitted Piles without Accelerated Aging

In many cases during the testing of FRP strengthened timber piles, small localized ruptures developed in the FRP composite at various points in the test that led to sudden but minor drops in the stress. Since FRP composites are brittle, complete rupture of the FRP occurred very suddenly. However, it was noted that even when the FRP has failed, the timber inside was still relatively sound. Therefore, the specimens were loaded until the timber pile itself failed. A typical test progression up to failure is illustrated in Figure 3.7 for specimen SP19-M5dU.

a) **b)** **c)** **d)**

Figure 3.7 Typical FRP strengthened specimen damage progression: **a)** beginning of loading **b)** initial longitudinal rupture of the FRP **c)** rupture propagation **d)** complete rupture of the FRP and crushing of the timber pile

Test results of two unretrofitted specimens and seven FRP wrapped specimens, all without accelerated aging, are plotted in Figure 3.8. In comparison to the as-is timber piles, the

FRP strengthened specimens performed considerably better. Both the strength and ductility were significantly improved. Ductility in this study was assessed based on the ductility ratio which was defined as the ratio between the ultimate strain and the strain at onset of nonlinear behavior. Ultimate strain is defined in this study as the strain at the post-peak stress stage corresponding to 20% drop from the peak stress.

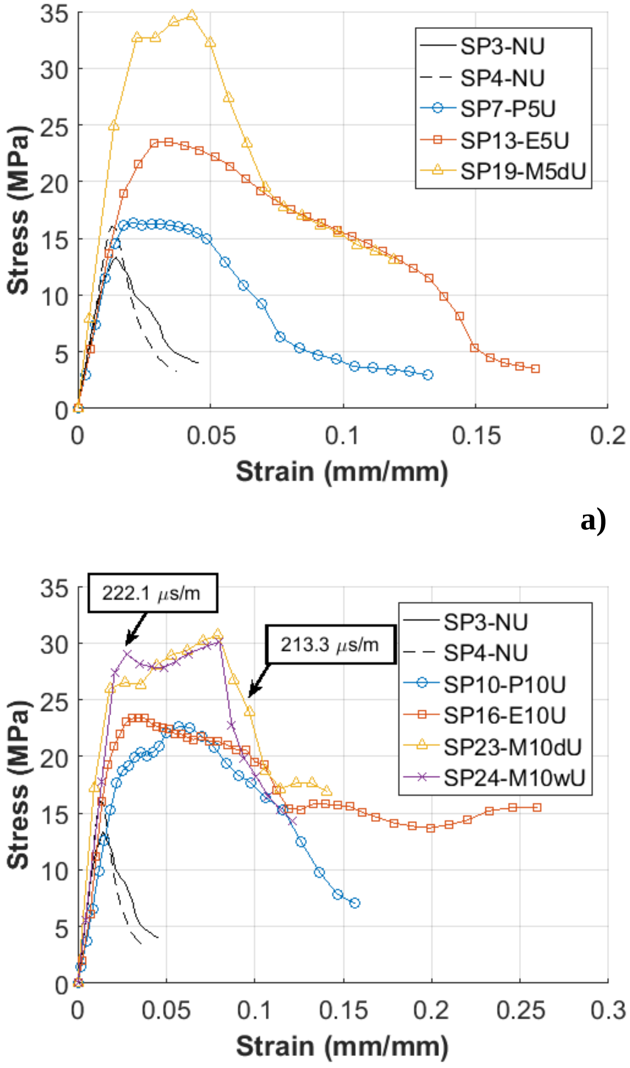

Specimen	Ductility Ratio
SP3-NU	1.5
SP4-NU	1.4
SP7-P5U	2.9
SP13-E5U	2.4
SP19-M5dU	2.8

a)

Specimen	Ductility Ratio
SP3-NU	1.5
SP4-NU	1.4
SP10-P10U	3.6
SP16-E10U	3.7
SP23-M10dU	4.5
SP24-M10wU	4.5

b)

Figure 3.8 Performance of FRP strengthened timber piles not subjected to accelerated aging **a)** 5 layers **b)** 10 layers

The 5 layer and 10 layer FRP specimens had average peak stresses of 25.0 MPa and 26.7 MPa, respectively. On average, this represents an increase of 70% and 82% compared to the unretrofitted specimens. As illustrated in the figure, increasing the thickness of the FRP did not yield a proportional increase in the peak stress but the 10 layer FRP specimens were considerably more ductile compared to the 5 layer specimens. The average ductility ratio of the 5 layer and 10 layer specimens were 2.7 and 4.0, respectively. Compared to the average ductility of 1.4 observed in the as-is specimens, the ductility is improved by more than 90%. Compared to the increase in peak stress, the FRP strengthening did not lead to drastic changes in the modulus of elasticity. The average elastic modulus in the 5 and 10 layer specimens was 1,629 MPa, and 1,530 MPa, respectively. As mentioned above, this can be attributed to the fact that the primary function of the FRP composite under the axial load was to provide confinement in the radial direction. Although the glass fabric used was bi-directional, the fibers in the longitudinal direction were not directly bearing and consequently did not provide any additional stiffness.

For specimens SP23-M10dU, and SP24-M10wU, the average stress wave transmission times through the timber pile are noted in Figure 8b as 213.3 μs/m and 222.1 μs/m, respectively. These values are comparable to the reference values presented in [19] and indicate that both timber piles were in good condition. Since both piles were in similar initial condition and retrofitted with the same amount of FRP, it is clear that the surface condition of the timber prior to applying the FRP did not have a significant effect on the performance of the moisture tolerant epoxy resin.

3.4.3 Effect of Accelerated Aging

Although the internal effects of the accelerated aging on the unretrofitted timber piles could not be directly observed, the aging procedure caused extensive splitting. Test results for unretrofitted specimens with and without accelerated aging are compared in Figure 3.9. From these results, it is clear that the accelerated aging leads to reductions in the strength.

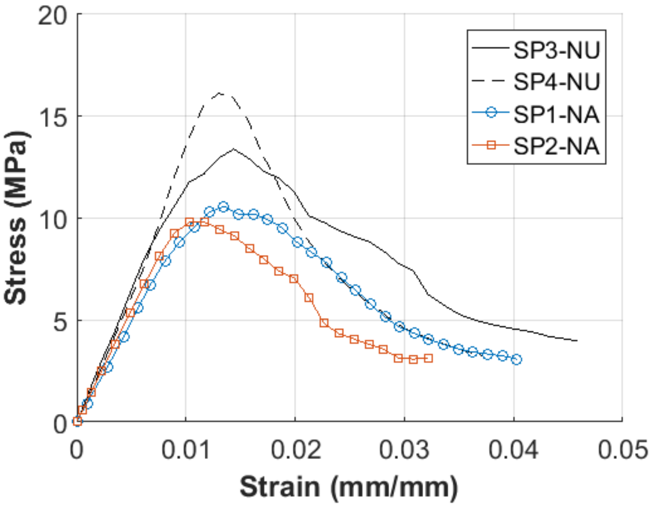

Figure 3.9 Unretrofitted timber piles, as-is and after accelerated aging

Compared to the specimens that did not go through accelerated aging, the aging procedure led to an average reduction of 31% in peak stress and 17% in the elastic modulus for the as-is specimens. Stress wave timing indicated that both specimens SP1-NA and SP2-NA shown in Figure 3.9 were initially in very good condition before the accelerated aging procedure.

As discussed previously, the accelerated aging procedure did not visibly damage the FRP composites. However, an increase in the stress wave transmission time suggests that additional degradation was induced in the timber piles (see Table 3.4). The test results for the FRP retrofitted timber piles subjected to accelerated aging are shown in Figure 3.10. It could be noted that with the exception of the 5 layer polyester resin specimens, the accelerated aging led to a loss in peak stress between 10% and 34% in the FRP retrofitted specimens compared to the unaged specimens.

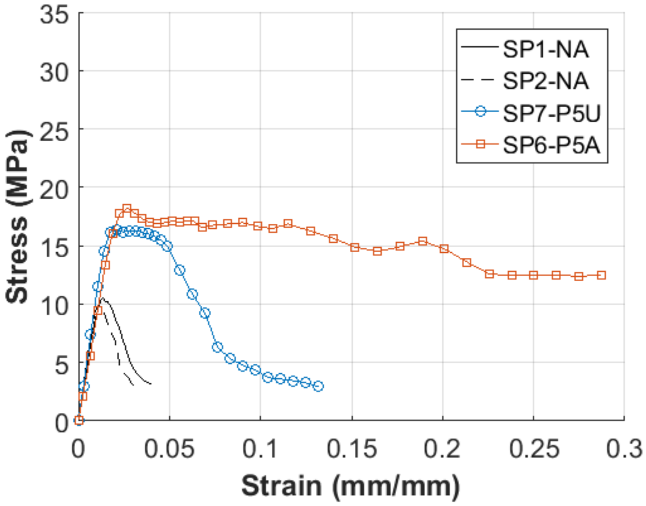

Specimen	Ductility Ratio
SP1-NA	1.5
SP2-NA	1.4
SP3-NU	1.5
SP4-NU	1.4
SP6-P5A	5.9
SP7-P5U	2.9

a)

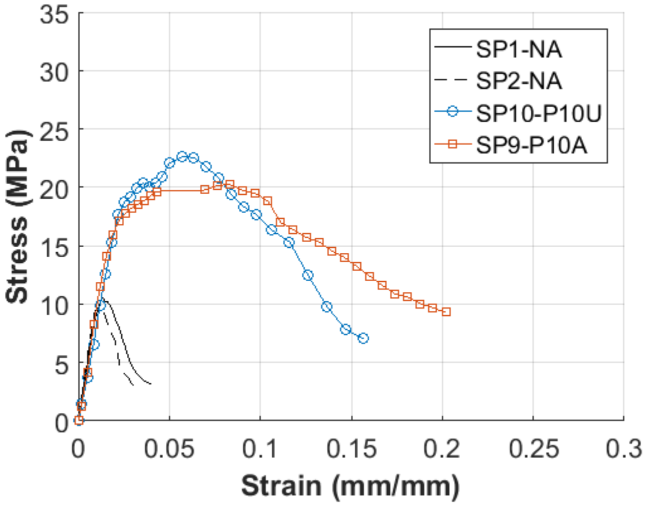

Specimen	Ductility Ratio
SP1-NA	1.5
SP2-NA	1.4
SP3-NU	1.5
SP4-NU	1.4
SP9-P10A	4.4
SP10-P10U	3.6

b)

Figure 3.10 Stress-strain behavior of unretrofitted and FRP strengthened timber piles subjected to accelerated aging **a)** 5 layer polyester resin **b)** 10 layer polyester resin **c)** 5 layer standard epoxy resin **d)** 10 layer standard epoxy resin **e)** 5 layer moisture tolerant epoxy **f)** 10 layer moisture tolerant epoxy

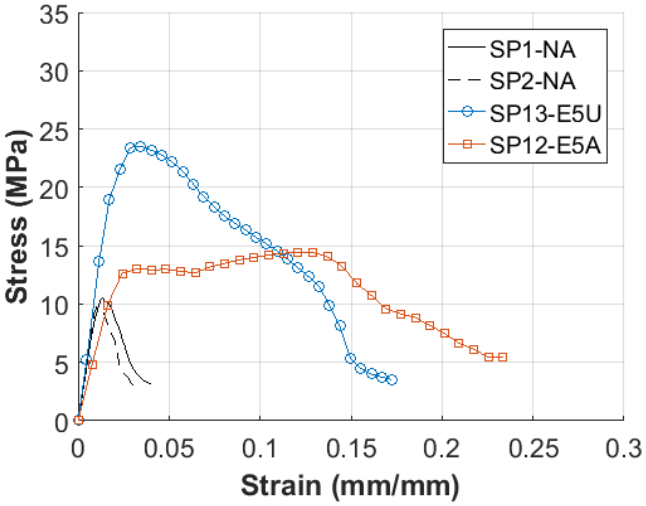

Specimen	Ductility Ratio
SP1-NA	1.5
SP2-NA	1.4
SP3-NU	1.5
SP4-NU	1.4
SP12-E5A	6.0
SP13-E5U	2.4

c)

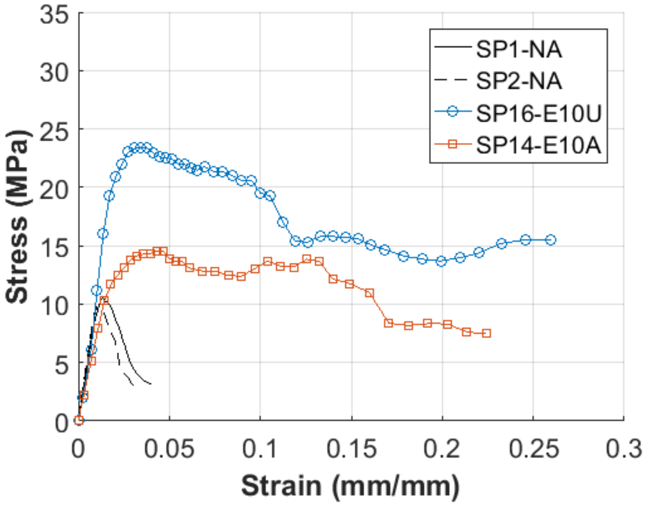

Specimen	Ductility Ratio
SP1-NA	1.5
SP2-NA	1.4
SP3-NU	1.5
SP4-NU	1.4
SP14-E10A	5.6
SP16-E10U	3.7

d)

Figure 3.10 (cont.)

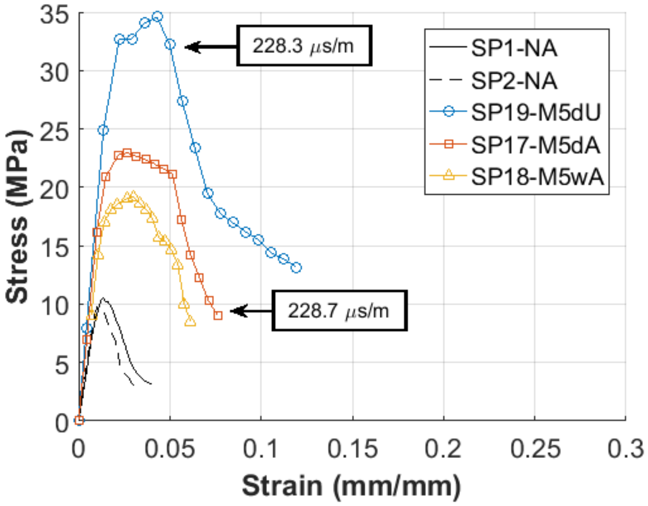

Specimen	Ductility Ratio
SP1-NA	1.5
SP2-NA	1.4
SP3-NU	1.5
SP4-NU	1.4
SP17-M5dA	2.8
SP18-M5wA	2.4
SP19-M5dU	2.8

e)

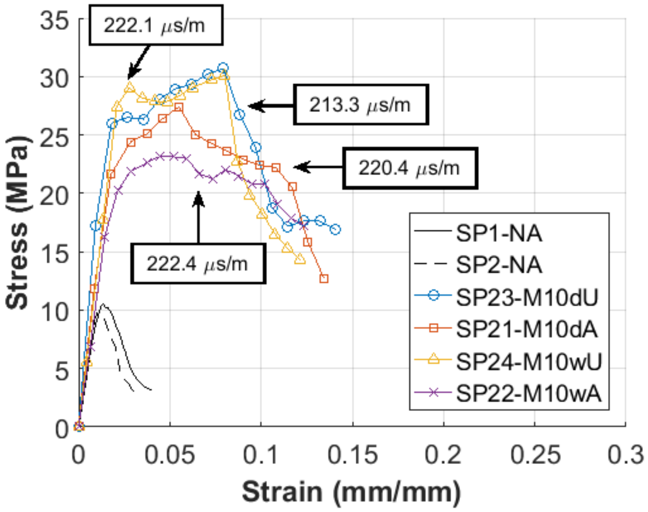

Specimen	Ductility Ratio
SP1-NA	1.5
SP2-NA	1.4
SP3-NU	1.5
SP4-NU	1.4
SP21-M10dA	3.8
SP23-M10dU	4.5
SP22-M10wA	4.4
SP24-M10wU	4.5

f)

Figure 3.10 (cont.)

Comparing the plots for each resin type in Figure 3.10, it can be seen that in general, higher levels of ductility were obtained from FRP composites fabricated with polyester and standard epoxy resin than the moisture tolerant epoxy. However, the moisture tolerant epoxy specimens attained higher peak stresses both before and after accelerated aging. Overall, with the exception of the standard epoxy specimens, increasing the FRP thickness led to improved strength retention after accelerated aging. The average strength loss due to aging in the 5 layer specimens was 35% compared to 15% in the 10 layer specimens. Therefore, applying a thicker FRP retrofit in the field may be beneficial for long-term environmental degradation. The accelerated aging did not affect the ductility of the FRP retrofitted specimens.

In Figure 3.10 a) it can be seen that specimen SP7-P5U failed at much lower strains compared to the other retrofitted specimens. The FRP in specimen SP7-P5U ruptured at lower strain levels and failed to properly confine the timber pile. In the 10 layer specimens, although the accelerated aging caused a drop in the peak stress, the ductility ratio and stiffness were unaffected. It can also be seen that the 10 layer specimen SP9-P10A retained a 10% higher peak stress compared to the 5 layer specimen SP6-P5A when subjected to accelerated aging.

Compared to the polyester or moisture tolerant epoxy FRP, the relatively poor performance of the standard epoxy resin specimens subjected to accelerated aging could be attributable to the poor initial condition of the timber. Specimen SP12-E5A shown in Figure 3.10 c) had an initial stress wave transmission time of 242.5 μs/m. In comparison, the initial stress wave transmission times for the two unretrofitted specimens SP1-NA and SP2-NA subjected to accelerated aging shown in Figure 3.10, were 215.6 and 211.0 μs/m, respectively. This suggests that specimen SP12-E5A was more severely deteriorated prior to testing. However, SP12-E5A achieved a 37% higher peak stress and showed a significant improvement in the ductility compared to the unretrofitted specimens.

It can be seen in Figure 3.10 e) that specimens SP19-M5dU and SP17-M5dA had almost identical stress wave transmission times, indicating that they were in similar initial condition. Similarly, in Figure 3.10 f), the initial condition of specimens SP22-M10wA and SP24-M10wU were comparable. However after the accelerated aging procedure, the peak stress of SP17-M5dA and SP22-M10wA were lower than their unaged counterparts by 34% and 23%, respectively.

Despite the reductions in peak stress observed after accelerated aging, the FRP wrapped timber piles still performed significantly better under accelerated aging than the unretrofitted timber piles. This shows that the FRP retrofit can effectively improve the structural properties of severely damaged timber piles and that this efficacy is expected to be maintained despite the harsh environmental and service conditions of the piles.

3.5 SUMMARY OF CHAPTER 3

The effectiveness of FRP strengthening of timber piles after long-term degradation was investigated by testing field-extracted Red Oak timber piles wrapped with GFRP composites. FRP thickness, resin type, and timber pile initial condition were the three main parameters examined in this study. An accelerated aging technique was used to induce artificial deterioration equivalent to approximately 20 years of field exposure. 20 timber pile specimens were wrapped with five or ten 0.635 mm thick layers of GFRP composite fabricated with polyester, standard epoxy, or a moisture tolerant resin. Prior to testing, the initial condition of the timber piles was evaluated using a nondestructive stress wave timing technique. Including four unretrofitted specimens, a total of 24 specimens were tested in uniaxial compression in the direction parallel to the grain. The following conclusions could be drawn from the study:

- The accelerated aging procedure was shown to cause substantial degradation in timber piles. The accelerated aging did not visibly damage the FRP composites.
- Without accelerated aging, using 5 and 10 layers of FRP improved the peak strength of the timber piles by 70% and 82%, respectively compared to the unretrofitted specimens.
- In general, increasing the thickness of the FRP did not result in a proportional increase in the strength but had a direct impact on the ductility. Since the primary function of the FRP composite was to provide confinement the retrofit did not affect the stiffness.
- The ductility ratios for each resin type were comparable. The surface condition did not have a major influence on the bonding of the moisture tolerant epoxy resin.
- On average, strength loss after accelerated aging was 35% in the 5 layer specimens and 15% in the 10 layer specimens. Despite the reductions in peak stress, the FRP wrapped timber piles still performed significantly better than the unretrofitted timber piles after accelerated aging. Therefore, applying a thicker FRP retrofit in the field may be beneficial for mitigating long-term environmental degradation.
- The average ductility ratio of the 5 layer and 10 layer specimens were 2.7 and 4.0, respectively. Compared to the as-is specimens, the ductility is improved by more than 90%. The accelerated aging did not affect the ductility of the FRP retrofitted specimens.

- The moisture tolerant epoxy resin attained higher strength than the polyester or standard epoxy resin. The peak strength of the moisture tolerant resin specimens was higher than the other FPR retrofitted specimens by at least 30% and 5% without and with accelerated aging, respectively.

CHAPTER 4

FULL-SCALE TESTING OF ABUTMENT TIMBER PILES RETROFITTED WITH FRP COMPOSITES

Experimental results in Chapter 3 showed that fully wrapping a timber pile with FRP composites can significantly improve its strength in both the short-term and long-term. In some cases, however, fully wrapping a pile may not be feasible. One such case is the case of abutments where the backing wall precludes full confinement of the piles. As a result, FRP retrofits to abutment timber piles may only be feasible in the form of stiffening strips or shells to the exposed side of the pile. Under typical conditions, this is the side under tension. Because common defects in wood such as knots and checks cause timber to be weaker in tension, the bending strength of timber piles is typically governed by the tensile strength. (Buchanan 1984). Therefore, reinforcing the exposed tensile face of the abutment timber piles with FRP composites can be an effective way to strengthen them. In this chapter, full-scale timber pile specimens were used to experimentally investigate this retrofit method. The piles were first inspected using SWT then retrofitted with FRP composites and tested using a unique setup which generated combined compression-bending loads representative of field conditions. The results showed that a good understanding of the timber condition is essential to design effective FRP retrofits. To investigate this further, a FE model of the experimental test was analyzed using material properties developed based on the SWT inspection and test results. SWT provides a valuable quantitative representation of timber condition that can provide the link between deterioration and repair decisions.

4.1 TIMBER PILE SPECIMENS

Three Red Oak piles removed from service were used in the study. The timber pile specimens are shown in Figure 4.1. It was unclear how long these piles were in service and what service conditions they were exposed to. Nevertheless, visual inspection of the piles found no signs of decay or damage to the exterior of the specimens. Minor splitting was common across all three specimens. Red Oak is a common species of wood used as piles and railroad sleepers. Reference design values for Red Oak listed in the National Design Specification for Wood Construction (NDS) are shown in Table 3.1

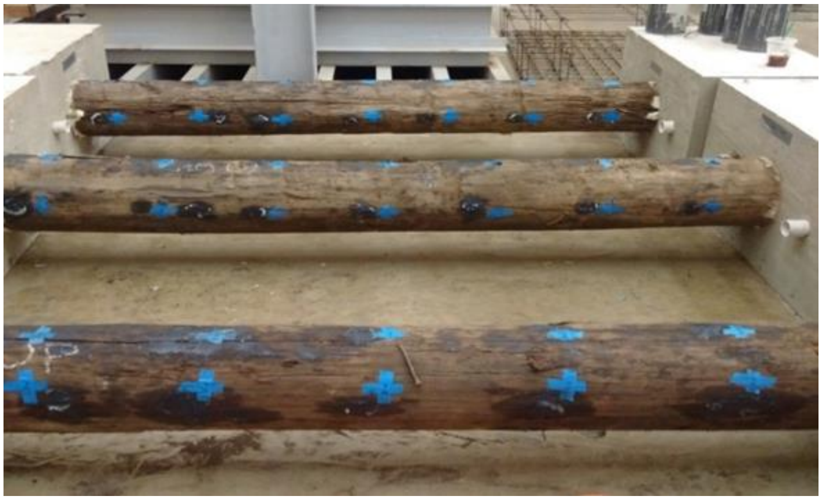

Figure 4.1 Timber pile specimens used in experimental testing of FRP retrofits

The specimens were denoted SP1, SP2, and SP3. The average diameter of SP1 and SP3 was approximately 271 mm, and the average diameter of SP2 was 279 mm. The average density of the specimens was approximately 740 kg/m^3. Specimen SP3 was tested as-is to determine the baseline performance, while specimens SP1 and SP2 were retrofitted using FRP composites before testing. In order to gain an understanding of the internal condition of the piles and obtain a quantifiable measure of the condition of the piles, a nondestructive testing method based on stress wave timing (SWT) was used.

4.2 CONDITION ASSESSMENT USING SWT

In this study, the same UPV instrument used in Chapter 3 was used to take six cross-sectional stress wave velocity measurements at seven equally spaced locations along the length of each of the three piles. Although the number of measurements was not sufficient to develop a detailed tomographic image of the cross-section, the values provided a good indication of the internal condition and a standard for comparing the three specimens. The average stress wave velocity at each cross-section along the length is plotted in Figure 4.2. A constant input stress wave frequency of 54 kHz was used for all measurements.

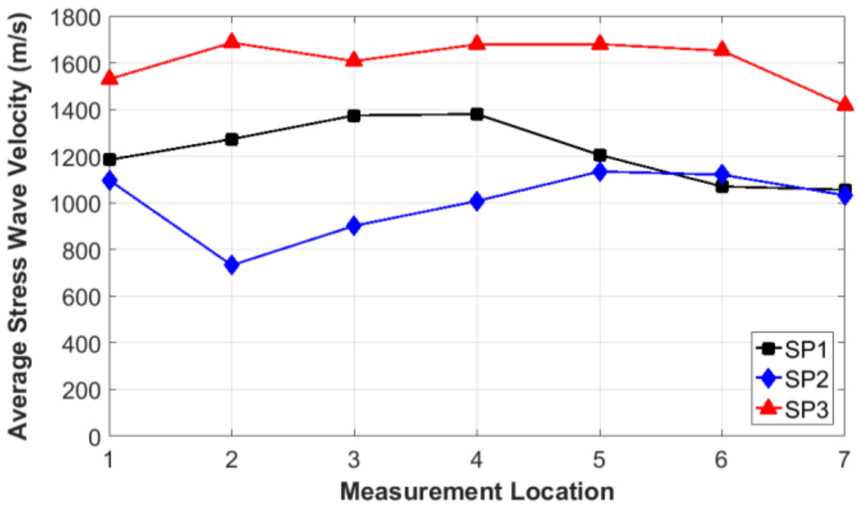

Figure 4.2 Average stress wave velocity perpendicular to the grain along the pile length

The average stress wave velocity in SP2 at location 2 was considerably lower compared to the rest of the pile. This suggests there exists some localized internal defect or damage at this location. Similarly, in SP1, the stress wave velocities drop near locations 6 and 7. Overall, the plot of average stress wave velocity clearly shows that the condition of specimens SP1 and SP2 were inferior compared to specimen SP3. The stress wave velocities averaged over the length for each specimen are 1,220 m/s, 1,003 m/s, and 1,607 m/s for SP1, SP2, and SP3, respectively. These values correspond to average stress wave transmission times of 917 μs/m, 1,124 μs/m, and 636 μs/m for SP1, SP2, and SP3, respectively. Compared to the values for stress wave transmission velocity perpendicular to the grain shown in Table 2.2, it can be seen that SP3 is within the range of undeteriorated Red Oak. SP1 and SP2 are well outside this range.

After all load tests were completed each pile was cut into five segments and stress wave timing measurements were taken in the direction parallel to the grain. As discussed above, these measurements offer a more direct representation of the structural condition of timber piles because they are illustrative of a pile's stiffness. The cut cross-sections of the pile specimens showed no visible signs of decay or wood fiber failures from the load testing. The average longitudinal stress wave velocities for SP1, SP2, and SP3 were 4.64×10^3 m/s, 4.33×10^3 m/s, and 4.98×10^3 m/s, respectively. Using Equation (2.5), these values correspond to dynamic moduli of 1.92×10^5 MPa, 1.67×10^5 MPa, and 2.18×10^5 MPa. Although this clearly shows that the condition of the timber piles in SP1 and SP2 was inferior to that of SP3, comparing these values to Table 1 suggests that the timber in SP1 and SP2 were in fair condition. Assessing the longitudinal stress wave timing results in light of the measurements taken perpendicular to the grain (Figure 4.2), suggests that the deterioration and defects may be more localized.

4.3 FIBER REINFORCED POLYMER RETROFIT

4.3.1 Material Properties

In this study the same GFRP woven roving fabric and standard epoxy resin used in Chapter 3 were used to fabricate the FRP composite. The FRP was applied to the timber piles using the hand-layup technique. The GFRP fabric was 0.635 mm thick with a modulus of 12,400 MPa and ultimate strain of 2%. Although the woven fabric consists of fibers in the longitudinal and transverse directions, the transverse fibers have no flexural stiffness contribution. The epoxy resin was a medium viscosity, two part resin with a pot life of 60 minutes. The characteristics of the materials used to fabricate the FRP composite are outlined in Table 4.2.

Table 4.1 FRP composite material properties

GFRP Woven Roving	Thickness: 0.635 mm Density: 0.67 kg/m^3 Elastic Modulus: 12,400 MPa Ultimate Strain: 2%
Epoxy Resin	Density: 1.1 kg/L Tensile Strength: 67.8 MPa Ultimate Strain: 1.9%

A coupon specimen was fabricated using the materials shown in Table 4.2 and tested in uniaxial tension. The composite showed an elastic modulus of 14,700 MPa and failed at a strain of 2.2%.

4.3.2 FRP Design

Currently there is no design guideline available for the design of FRP retrofits for timber structures. However, as introduced in Section 2.3, the study by Caiza et al. (2012) offers useful guidelines for using FRP composites to strengthen timber piles. In their experimental work, Caiza et al. (2012) used FRP materials and Red Oak timber pile specimens similar to the ones considered in this study and concluded that most of the pile specimens required 8 or 9 layers of GFRP composite to restore their flexural stiffness. Using this as the baseline, it was decided that 10 layers of GFRP (6.35 mm) would be used to retrofit two abutment timber pile specimens, namely SP1 and SP2. It is important to note that this design does not account for the initial timber pile condition.

As explained earlier, in the case of abutment timber piles, due to the retaining wall, only part of the pile will be exposed, hence it is not feasible to fully wrap the pile with FRP. Therefore, FRP retrofits for abutment timber piles can only be applied to the exposed side which corresponds to the tension side. The behavior of timber members in bending is typically governed by tension due to the fact that defects in the wood such as knots and checks greatly reduce the tensile strength. Compressive strength is not significantly affected by defects (Buchanan 1984). The FRP retrofit in this case would effectively improve the strength of the timber pile in bending but will not provide any additional strength or stiffness in compression.

Two FRP configurations were considered in this study as shown in Figure 4.3. The first configuration is a uniform half-shell encompassing one half of the timber pile. In the second configuration, 75 mm wide FRP strips of identical thickness are evenly spaced over the tensile half of the pile. In both cases the FRP is applied along the full length of the pile. Since it was shown that timber pile specimen SP3 was in the best condition, it was tested as-is and used as the control specimen. The half-shell FRP configuration was applied to specimen SP2, and the strip configuration to specimen SP1. Both configurations were comprised of 10 FRP layers which represents FRP volumetric ratios of 0.025 and 0.047 for SP1 and SP2 respectively. As discussed above, the FRP serves as tensile reinforcement in these retrofits. However, since stresses will be relatively low away from the extreme fibers the FRP may not necessarily contribute. The key idea behind the FRP strip retrofit is to reduce the FRP volume which reduces material cost and work required without a significant compromise in the performance.

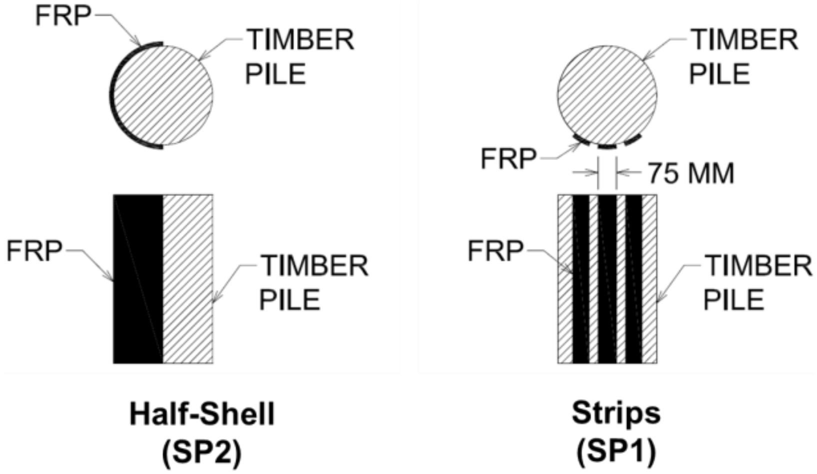

Figure 4.3 FRP retrofitting schemes used in the study

Prior to applying the FRP composite to the piles, the surfaces of the timber piles were cleaned with a wire brush to remove any dirt and debris. The fabric was cut to size and saturated with resin using rollers. Once applied, the FRP was allowed to cure for at least 72 hours before testing. Although the bond strength between the timber and FRP composites was not investigated in this study, insufficient bond strength may critically limit the performance of this retrofit. The effect of timber surface condition and polymer matrix type should be investigated to characterize the bond behavior of externally bonded FRP composites on timber. The retrofitted specimens are shown in Figure 4.4.

a) **b)**

Figure 4.4 FRP retrofitted timber pile specimens **a)** SP1 – GFRP strips **b)** SP2 – GFRP Half-Shell

4.4 EXPERIMENTAL TESTING

4.4.1 Test Setup

Experimental tests on timber piles under eccentric loading by Borello et al. (2010) showed that the presence of bending significantly reduces the axial capacity of the piles. Abutment timber piles are generally loaded concentrically in the axial direction but lateral loads imposed by earth pressure and surcharge loads generate bending moments. Based on a survey conducted on several existing timber pile bridges, it was decided to cut the specimens to a total length of 2,744 mm and have the two pile ends embedded 305 mm in reinforced concrete pile caps to facilitate the application of both axial and bending concurrently. To apply combined bending and axial loads to the pile specimens the post-tensioning scheme shown in Figure 4.5 was used.

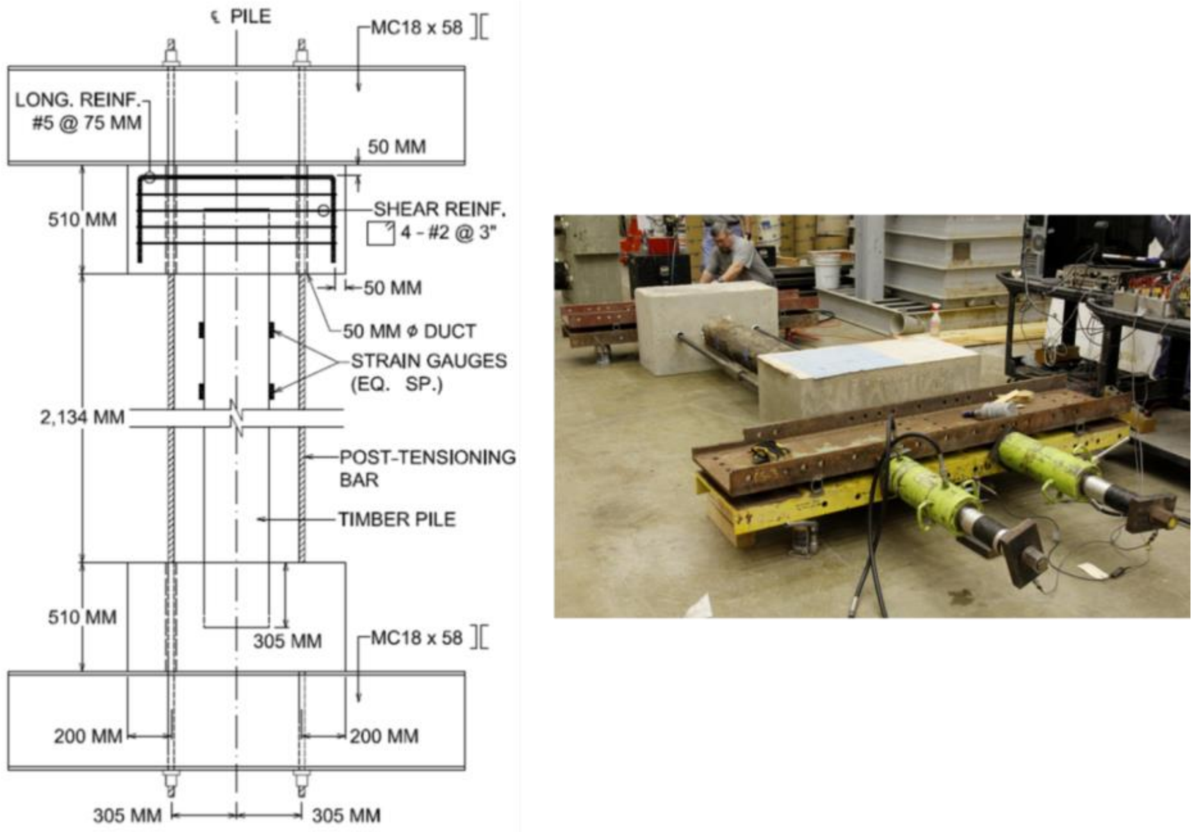

Figure 4.5 Combined axial-bending interaction setup used in testing the piles

As shown in Figure 4.5, back-to-back MC18×58 (AISC designation) steel sections were used on top of the pile-caps to prevent the piles from punching through. Two 38 mm diameter post-tensioning rods were fitted through the C-channels and pile-caps 305 mm away from the pile centerline on either side. The tests were conducted by first imposing a constant bending moment then applying a concentric axial force. The bending moment was induced by tensioning only one of the rods using a bolt stretcher. Once the desired bending moment is reached, the eccentric load was anchored off and both rods were then tensioned simultaneously from the opposite end using two hydraulic jacks. The concentric load was increased until the onset of nonlinear behavior. Each pile was tested up to the elastic limit under eccentric loads varying from 44.5 kN up to 155.7 kN in 22.2 kN increments. The forces applied on the piles were monitored using load cells. As shown in Figure 4.5, strains in the timber and FRP were measured at the extreme pile fibers at quarter and mid-length, and linear variable displacement transducers (LVDTs) were placed at the ends of the pile-caps to measure the total axial deformations. The tests were conducted with the timber piles lying horizontally. The interface between the pile caps and the floor was lubricated with form oil in order to minimize friction.

4.4.2 Test Results

As explained above, each specimen was loaded with a prescribed eccentric load applied through an eccentricity of 305 mm then an increasing concentric load up to the point of nonlinearity. The maximum total force at the proportional limit was taken as the ultimate load. This limit was based on the assumption of linear elasticity which forms the basis of the flexural design of timber piles and FRP retrofits. At high loads, significant bending in the timber piles was clearly noticeable with audible cracking of the FRP composite. The applied bending moment and resulting curvature at mid-height are plotted in Figure 4.6. The curvature was computed using strains measured at the extreme fibers of the specimen.

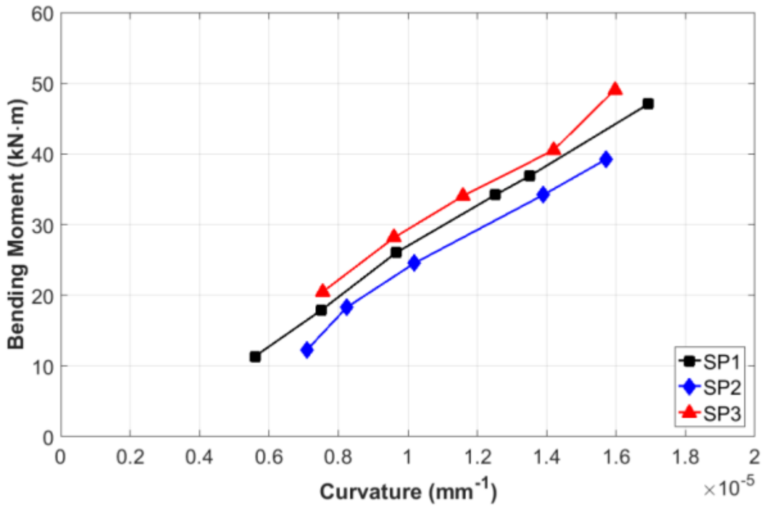

Figure 4.6 Mid-height curvature caused by the eccentric load

As can be seen, the curvature caused by the eccentric loads followed the same pattern for all three specimens. Compared to the unretrofitted specimen SP3, the curvatures in the retrofitted specimens SP1 and SP2 were 4% and 11% higher on average, respectively. This suggests that despite the additional stiffness provided by the FRP retrofit, the behavior is still strongly influenced by the timber pile condition. After each loading scheme, the specimens were fully unloaded and visually inspected. However, there was no visible damage to the timber piles or the FRP composite even at very high loads. The cracking of the FRP heard during testing was most likely from the resin as no visible fiber fractures were noted. Furthermore, there was no evidence of bond failure between the timber piles and FRP composites. The ultimate P-M interaction behavior is plotted in Figure 4.7.

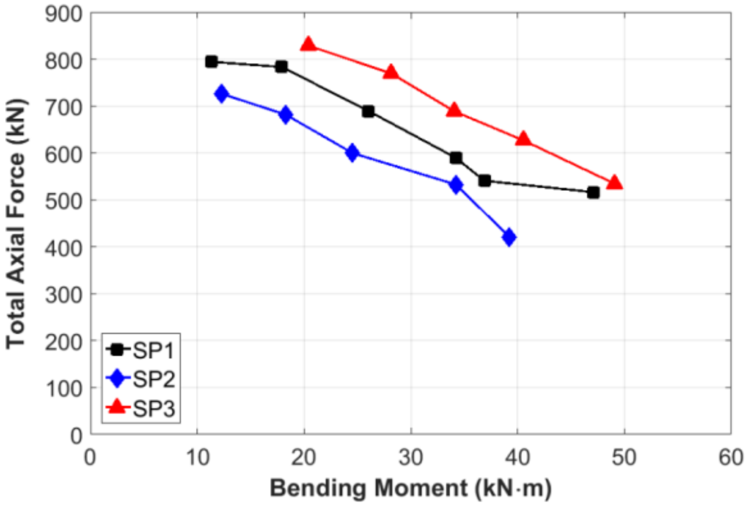

Figure 4.7 Peak total axial force attained under each bending moment

The observed P-M interaction follows the expected behavior with the peak axial force decreasing with increasing bending moment. For a given level of applied bending moment, the total axial force attained by the FRP half-shell specimen SP2 is approximately 30% lower than the unretrofitted specimen SP3. The difference is approximately 15% between the FRP strip specimen SP1 and SP3. However, direct comparison between the test results could be misleading due to the discrepancy in timber condition. Since the loading was kept in the linear elastic range, and the timber piles were very similar in size, these results suggest that the elastic modulus of the timber was significantly affected by the timber condition.

To neutralize the results based on the timber condition, the axial force and bending moment were normalized and nondimensionalized using Euler buckling load and design bending moment capacity. The normalization loads were computed as shown below.

$$P = \alpha \frac{\pi^2 EI}{L^2} \tag{4.2}$$

$$M = \alpha F_b S \tag{4.3}$$

In Equation (4.2), E is the reference minimum elastic modulus for Red Oak obtained from the NDS, I is the moment of inertia of each timber pile, and L is the effective length. In Equation (4.3), F_b is the design allowable bending stress for Red Oak from the NDS, and S is the timber pile section modulus. In both equations, α is a condition normalization factor computed as the ratio of the dynamic elastic modulus of a specimen to a reference value. For $\alpha = 1.0$, Equation (4.2) represents the design Euler buckling strength of an undeteriorated pile, and Equation (4.3) is the undeteriorated bending moment capacity. In this case, it was assumed that SP3 represented the ideal timber condition and was used as the reference timber pile. The condition normalization factors and resulting normalization loads are summarized in Table 4.3.

Table 4.2 Condition normalization factors and normalization loads

Specimen	**Dynamic Elastic Modulus (MPa)**	**Normalization Factor, α**	**Euler Buckling Load (kN)**	**Normalized Euler Buckling Load (kN)**	**Bending Moment Capacity (kN·m)**	**Normalized Bending Moment Capacity (kN·m)**
SP1	1.92×10^5	0.87	721.5	627.7	33.1	28.8
SP2	1.67×10^5	0.76	804.6	611.5	35.9	27.3
SP3	2.18×10^5	1.0	721.5	721.5	33.1	33.1

The Euler buckling strength and design bending moments are reasonable normalization factors in this case since they are both based on elastic behavior. In effect, dividing the test results by the normalized values in Table 4.3 standardizes the results to the reference timber condition. Therefore, the normalized values represent the magnitude by which the FRP retrofits would have improved the strength if all three timber piles were in identical initial condition to SP3. Furthermore, they are nondimensionalized with respect to design strengths defined in the NDS which shows how the test results compare to the design equations. The normalized test results are shown in Figure 4.8.

These results show that had SP1 and SP2 been in the same condition as SP3, the 6.35 mm thick (10 layers) FRP retrofit would have increased the axial capacity of SP1 and SP2 beyond that of SP3 by an average of approximately 7%. The performance improvement provided by the FRP retrofits appears marginal, but increasing the thickness of the FRP retrofits or using materials with higher strength could improve the strength further. Overall, the normalized results suggest that at the elastic limits to which the specimens were tested, the difference in the performance of the FRP half-shell and FRP strips is not significant. The test results also clearly show that a good understanding of the timber pile condition is necessary to design an effective retrofit.

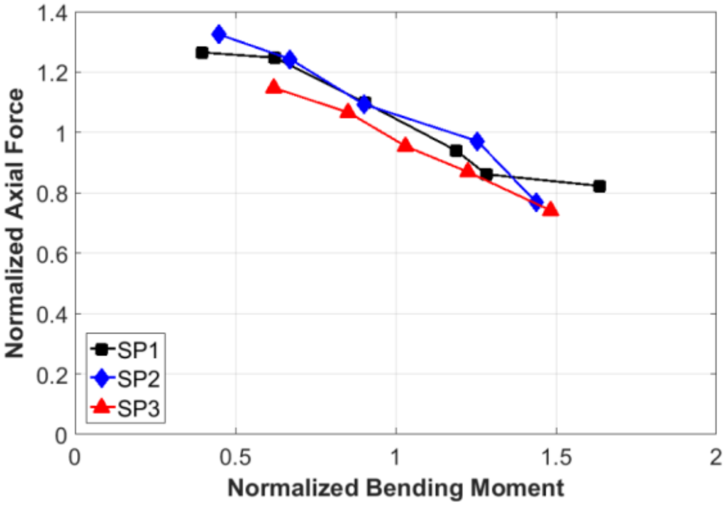

Figure 4.8 Peak total axial force attained under each bending moment

4.5 NUMERICAL ANALYSIS

4.5.1 Finite Element Model

A simplified finite element (FE) model of the experimental test setup was developed using ABAQUS (Dassault Systèmes Simulia Corp. 2011) to numerically evaluate the proposed FRP retrofit design method. The test specimens were replicated as uniform, prismatic parts. Assuming symmetry, only one half of the test setup was modeled. The FE model is shown in Figure 4.9.

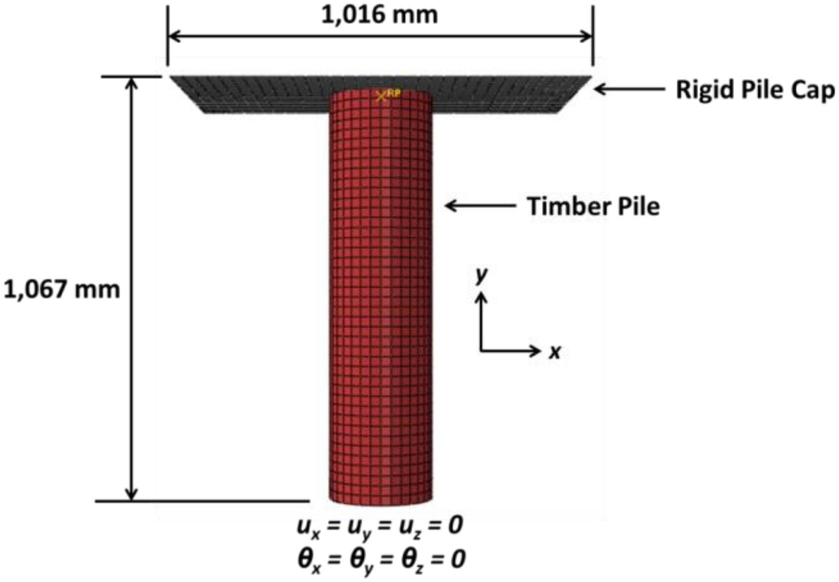

Figure 4.9 Abutment timber pile test FE model

The pile cap reinforced concrete and steel beam pile cap used in the experimental testing was modeled using discrete rigid shells. The timber pile was discretized using 8-node linear brick elements. The loads were applied through the pile cap as concentrated loads in the same sequence as in the experiments, 305 mm away from the pile centerline. As shown in Figure 4.9, the end of the pile was constrained against rotations and translations. Tie constraints were used to constrain the timber pile to the rigid pile cap. 4-node linear shell elements were used to model the FRP composites. The FRP was assumed to behave linearly up to brittle failure with an elastic modulus of 12,400 MPa and failure strain of 2%.

4.5.2 Timber Material Models

Under pure compression timber behaves in a nonlinear ductile manner. However under tension it behaves in a linear elastic manner until brittle fracture occurs. Based on the experimental test results, timber material models for SP1, SP2, and SP3 were calibrated. The timber stress-strain behavior adopted in the FE model is shown in Figure 4.10.

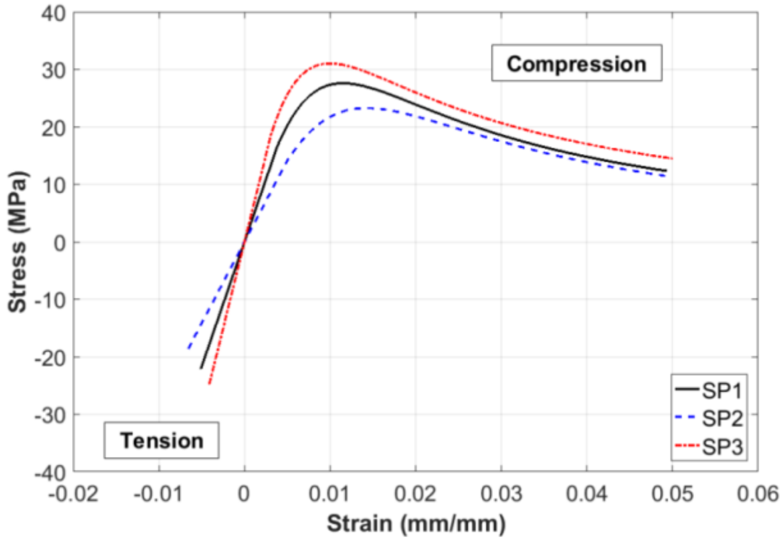

Figure 4.10 Timber stress-strain behavior calibrated from the experimental results

Compared to SP3, the elastic moduli of SP1 and SP2 were lower by 28% and 53%, respectively. The material models shown in Figure 4.10 are indicative of the stress wave timing results which showed that the timber piles in SP1 and SP2 were in much more deteriorated conditions compared to SP3. Figure 4.11 presents relationships between the dynamic moduli obtained from SWT for each specimen and the elastic moduli and peak compressive stress of the specimens. There appears to be a clear linear correlation between timber material properties and the dynamic modulus. These observations by no means constitute conclusive evidence of a relationship between timber material properties and dynamic modulus given the small sample size considered in this study. However, more detailed studies in this area would be beneficial for many different structural engineering applications.

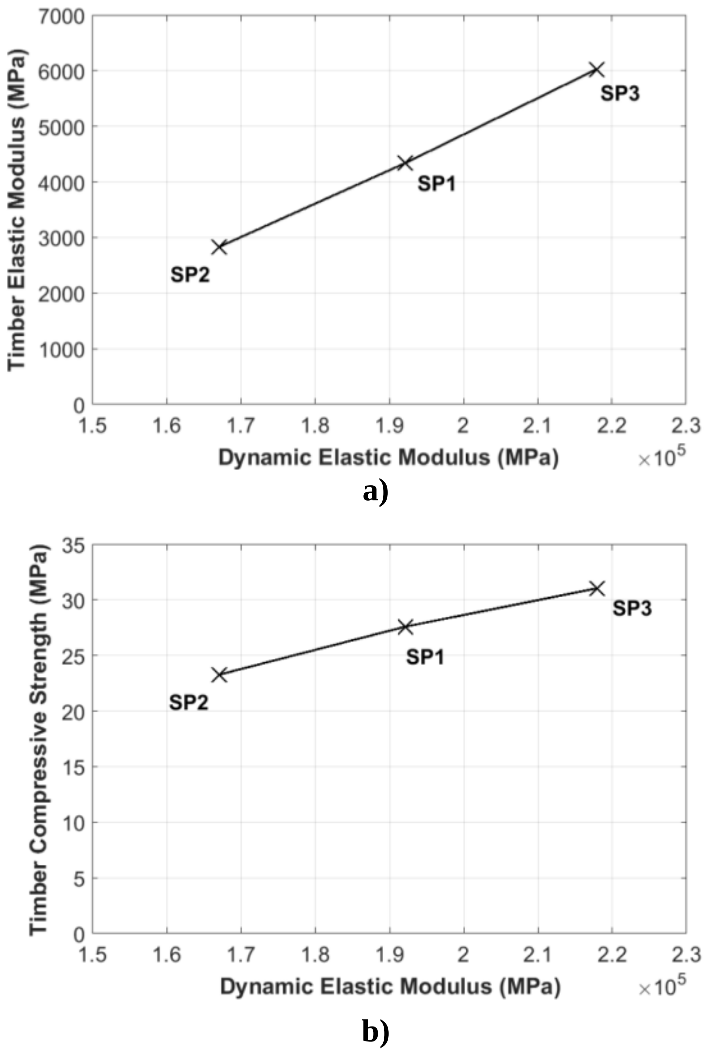

Figure 4.11 Calibrated timber pile material elastic modulus **a)** and compressive strength **b)** compared to dynamic elastic moduli computed from SWT measurements

Finally, Figure 4.12 shows how the FE model with the calibrated timber material properties compares to the experimental results. SP1 and SP2 were retrofitted with 6.35 mm thick FRP in the same configurations used in the experimental tests. Initial eccentric loads varying from 44.5 kN up to 155.7 kN were considered. As shown in Figure 4.12, the calibrated timber materials shown in Figure 4.10 yielded results in good agreement with the experimental tests.

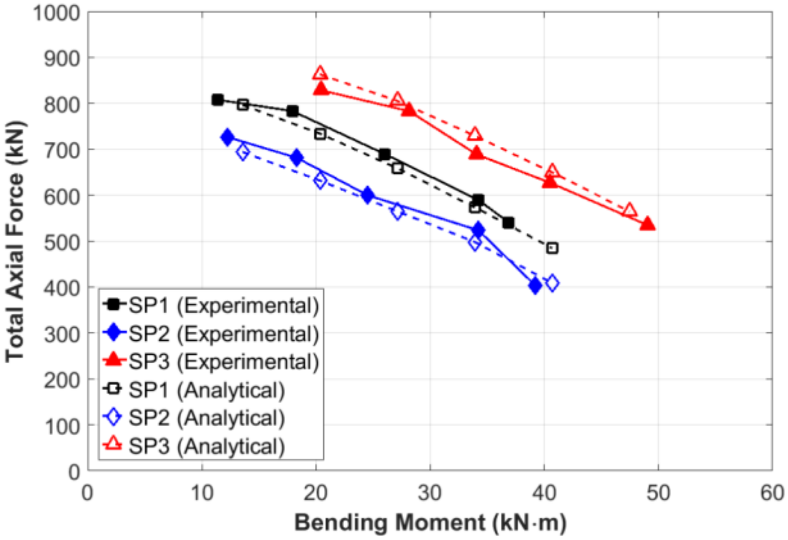

Figure 4.12 Comparison of FE model analysis results to experimental test results

4.5.3 FRP Retrofit Design

Since the stress wave velocity measurements and load test results both showed that the timber pile for SP3 was in the best condition compared to the other two piles, the capacity of SP3 was adopted as the target performance level for the FRP retrofit designs for SP1 and SP2. The FE model was used to incrementally increase the FRP thickness until the target performance levels were achieved. To compare the effectiveness of the two retrofit configurations used in the experimental study both configurations were considered in modeling SP1 and SP2. The performance improvements in SP1 and SP2 with increasing FRP ratio are illustrated in Figure 4.13.

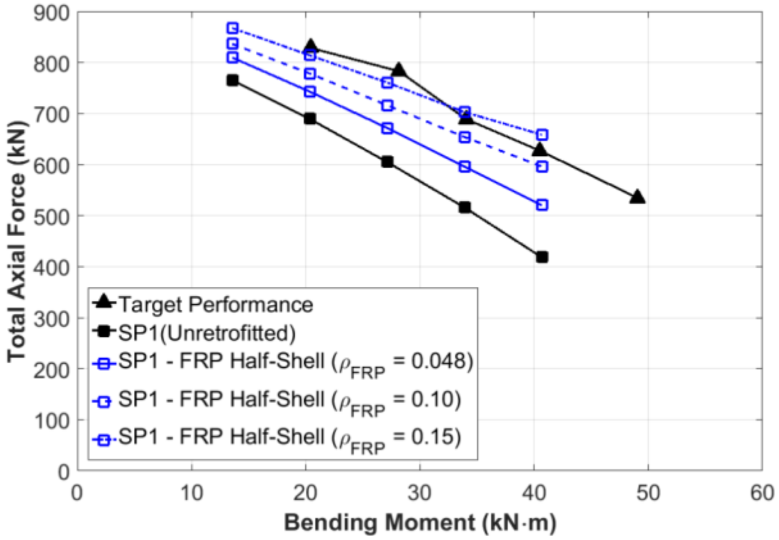

a)

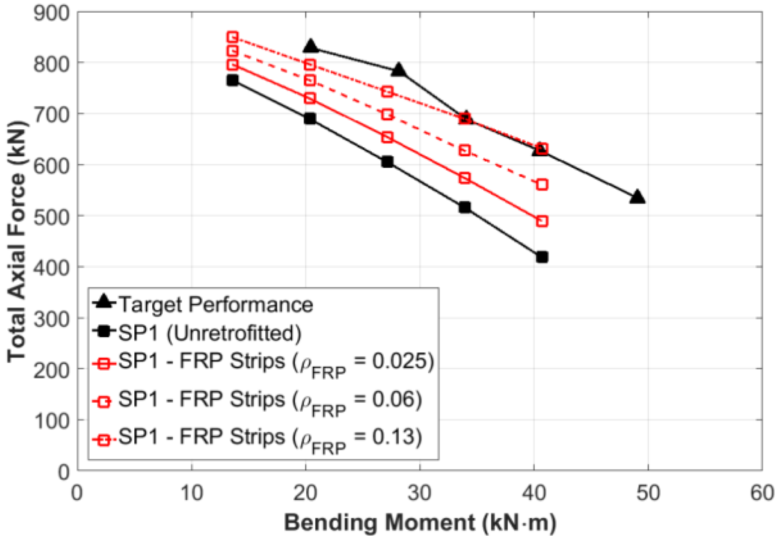

b)

Figure 4.13 FRP retrofit designs for **a)** SP1 with FRP half-shell **b)** SP1 with FRP strips **c)** SP2 with FRP half-shell **d)** SP2 with FRP Strips

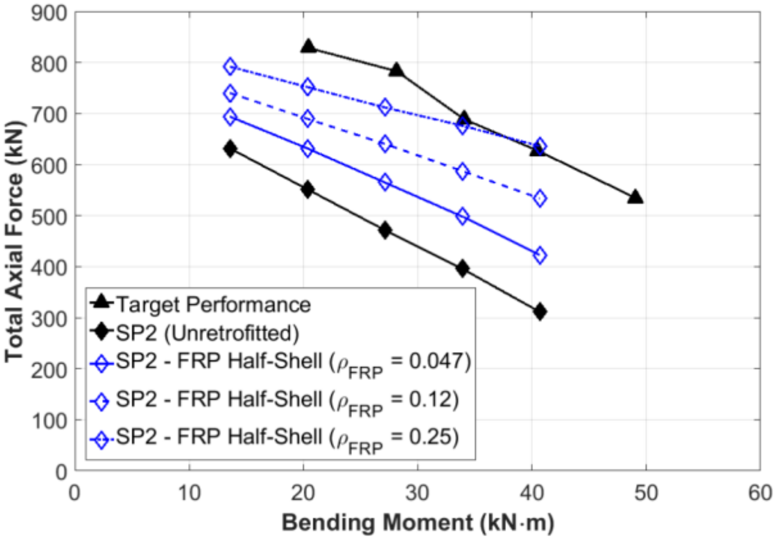

c)

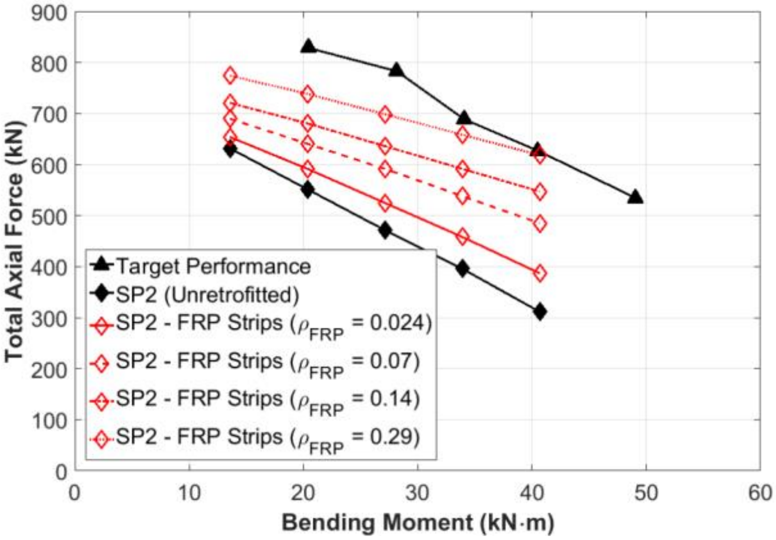

d)

Figure 4.13 (cont.)

In general, it is clear that both SP1 and SP2 required significantly higher FRP thicknesses than the 6.35 mm used in the experiments to restore their strength to levels comparable to SP3. Since the basic function of both retrofit configurations is to provide tensile reinforcement and neither provide significant stiffness in axial compression, it can be seen that the retrofits are more effective under higher bending moments. This is especially evident in SP2 shown in Figures 4.13 c) and d). As discussed above, SP2 was in a more deteriorated state than SP1. Under relatively low bending moments, the axial capacity could not be recovered even with high levels of ρ_{FRP}. However, when the P-M interaction is more flexure dominated at high bending moments, the FRP retrofits sufficiently improved the axial capacity. This disparity in the behavior is acceptable because should failure occur, the failure mode of timber in compression is very ductile whereas failure under bending governed by the tension capacity of unretrofitted timber is brittle.

In SP1, the half-shell retrofit at ρ_{FRP} = 0.15 increased the axial capacity by an average of 30%. The strip retrofit at ρ_{FRP} = 0.13 yielded an average improvement of 27%. Given the level of deterioration in SP2, significantly higher levels of FRP were needed to achieve the target performance. Comparing the FRP configurations, it can be seen that in SP1 the strip retrofit yielded similar results to the half-shell retrofit at a slightly lower ρ_{FRP}. The difference in axial capacity between the half-shell retrofit at ρ_{FRP} = 0.15 and strip retrofit at ρ_{FRP} = 0.13 was less than 4%. In contrast, for SP2, a volumetric ratio of 0.29 was required in the strip retrofit to improve the strength of SP2 to that of SP3 compared to 0.25 in the half-shell configuration. At these FRP volumes, the half-shell retrofit outperformed the strip retrofit by approximately 2%. This observation suggests that the choice of FRP configuration should be based on the level of timber deterioration.

Overall, the experimental tests and analytical models developed in this study show that a clear, quantified understanding of the timber pile condition is necessary to design effective retrofits.

4.6 SUMMARY OF CHAPTER 4

For deteriorated bridge abutment timber piles, full confinement using FRP is not possible due to the backing wall. Therefore, FRP retrofits can only be applied to the tension face of the piles. In this study, the effectiveness of this retrofitting technique was experimentally tested using three full-size timber piles. The experimental test results showed that in order to design effective FRP retrofits, detailed knowledge about the in-situ timber condition and level of deterioration is needed. The retrofit design needs to be tailored to the specific condition of a pile and the target performance level. An FE model was developed with timber material properties calibrated using the experimental test results to iteratively determine the volumetric ratio of FRP that would be required to sufficiently restore the capacities of the deteriorated piles. The main observations and findings from the study are summarized below.

- Stress wave velocity measurements taken perpendicular to the grain prior to load testing showed that timber pile specimen SP3 was in very good condition. In comparison, both SP1 and SP2 showed localized deterioration. Overall, SP2 was in the most deteriorated condition.
- Under bending moments, the mid-height curvatures were comparable between all three specimens. On average, the curvature in specimens SP1 and SP2 were 4% and 11% higher than SP3, respectively. This suggests that despite the additional stiffness provided by the FRP retrofit, the behavior is still strongly influenced by the timber pile condition.

- The P-M interaction curves generated for each pile showed that for a given level of applied bending moment, the axial load capacity of SP2 was approximately 30% lower than that of SP3 and the capacity of SP1 was 15% lower than SP3.
- The dynamic elastic moduli computed from stress wave velocity measurements taken in the direction parallel to the grain reflected correctly the condition of the three tested specimens.
- Normalized test results suggest that if the timber piles for both SP1 and SP2 were in the same condition as SP3, the FRP strip and half-shell retrofits would have increased the axial capacity by 7%.
- FE analysis showed that significantly higher amounts of FRP was required to adequately retrofit SP1 and SP2 compared to the actual FRP thickness that was used in the experiments (6.35 mm). This shows that a reliable assessment of the timber pile condition is critical in designing an effective retrofit.
- The effectiveness of the FRP half-shell and strip retrofits were comparable for SP1 which showed less deterioration than SP2. For SP2, higher strength was achieved with less material using the half-shell retrofit. This suggests that the FRP configuration should be chosen based on the level of deterioration.

CHAPTER 5

LOAD RATING OF DETERIORATED AND FRP RETROFITTED ABUTMENT TIMBER PILES

One of the most critical design simplifications in the design of most existing timber pile bridges is that the piles are assumed to carry axial loads only. The assumption that bending moments can be neglected was primarily based on experience and still forms the basis of the typical load rating method used today. There is a definite need to address this issue, especially for abutment timber piles which carry large lateral loads in addition to axial loads. In this study a load rating method is developed specifically for abutment timber piles. The new method takes into consideration varying pile length, dead load and earth pressure as well as accounting for pile deterioration. The study also introduces FRP composites as a means for reinforcing deficient timber piles and uses the new load rating method as a basis for design. The primary outcome from this study is a series of charts that can be used to estimate the allowable stress due to live loads in abutment timber piles and a design chart determining the required FRP thickness for deficient piles.

5.1 LOAD RATING PROCEDURE FOR AXIALLY LOADED PILES

The National Bridge Inspection Standards (NBIS) require all highway bridges with spans longer than 6.1 m to be load rated to determine safe loading capacities (Mertz 2012). Accurate load rating requires careful consideration of the as-built plans as well as information from field inspections. In the case of bridges supported on timber pile substructure, it is highly likely that the timber piles are the weakest link given their simplified design and susceptibility to deterioration.

The conventional timber pile load rating method is defined simply in terms of axial loads. It is calculated as the ratio of the pile capacity to the demand imposed by design truck live load (e.g. HS20-44 design truck) as shown below

$$Load\ Rating = \frac{Pile\ Capacity - Dead\ Load}{HS20\text{-}44\ Live\ Load} \tag{5.1}$$

where the pile capacity is limited by the allowable compressive strength of the timber or the geotechnical capacity, and the dead and live load demands can be determined through structural analysis. The underlying assumption is that all loads are applied concentrically and bending moments carried by the pile are negligible. In most multi-span timber pile bridges where the spans are simply-supported, timber piles supporting intermediate piers or bents may experience eccentric loading. In an investigation preceding the current study, Andrawes & Caiza (2011) showed that Equation (5.1) critically overestimates the capacity of piles under eccentric loading and proposed the following modifications:

$$Modified\ Load\ Rating = \frac{Live\ Load\ Stress\ Capacity,\ \ f_{cLL}|_{max}}{Stress\ due\ to\ Live\ Load} \tag{5.2}$$

Where, $f_{cLL}|_{max}$, the maximum allowable live load stress capacity in Equation (5.2) is obtained by solving for f_{cLL} in Equation (5.3) below.

$$\left(\frac{f_{cDL}}{F'_{cDL}} + \frac{f_{cLL}}{F'_{cLL}}\right)^2 + \frac{f_{cLL}(6e_{LL}/d)[1 + 0.234(f_{cLL}/F_{cE})]}{F'_b[1 - (f_{cLL}/F_{cE})]} \leq 1.0 \tag{5.3}$$

Equation (5.3) is based on the NDS design P-M interaction equation (AFPA 2005). In Equations (5.2) and (5.3), load demands and allowable stresses are represented using lower and upper case variables, respectively. Subscripts cLL and cDL denote the stress at the pile centroid due to live and dead loads, respectively. F_b' is the allowable bending stress, F_{cE} is the Euler buckling stress, e_{LL} is the eccentricity of the live load, and d is the pile diameter. The NDS design equations are used to determine the allowable stresses in which the allowable stress under dead and live loads are distinguished by the load duration factor. For F_{cDL}', the load duration factor, $C_D = 0.9$, and for F_{cLL}', $C_D = 1.15$. These values correspond to permanent and two month loading durations respectively and agree with AASHTO guidelines (AASHTO 2011).

5.2 PROPOSED LOAD RATING METHOD FOR ABUTMENT PILES

The modified load rating equations developed by Andrawes & Caiza (2011) are not directly applicable to piles supporting the abutment where deck eccentricity is typically not critical. Instead, abutment timber piles are subjected to lateral earth pressure and surcharge loads as shown in Figure 5.1.

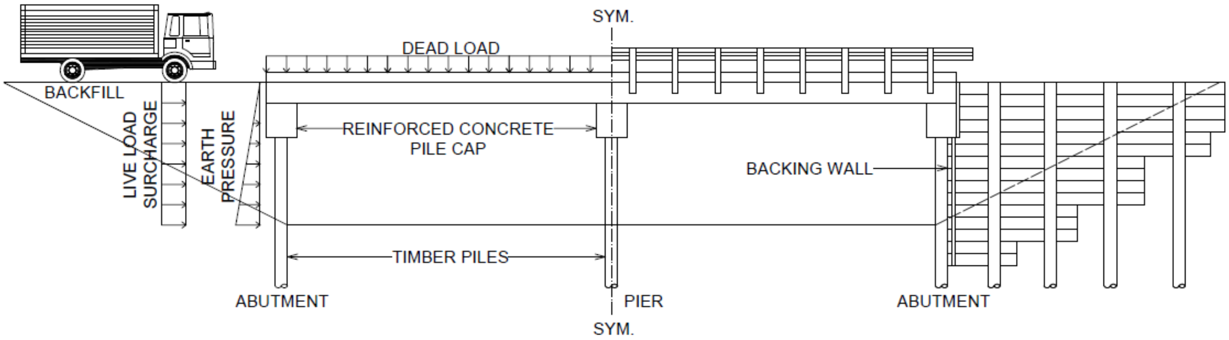

Figure 5.1 Loads applied on abutment timber piles

AASHTO guidelines require a live load surcharge to be applied to retaining walls when a vehicle load is applied on the surface of the backfill within a distance equal to one-half the wall height (AASHTO 2002). Live load surcharge can be idealized as a uniformly distributed horizontal pressure as shown in Figure 5.1. Currently, there does not exist a load rating method directly applicable to abutment timber piles that takes lateral loads into consideration.

5.2.1 Modified P-M Interaction Equation

Taking an approach similar to Andrawes & Caiza (2011), the NDS design P-M interaction equation was modified and used to determine the maximum allowable live load for abutment timber piles. The allowable live load stress capacity, $f_{cLL}|_{max}$ can be computed from:

$$\left(\frac{f_{cDL}}{F'_{cDL}}+\frac{f_{cLL}}{F'_{cLL}}\right)^2+\frac{(f_{bEP}/F'_{bEP}+f_{bLS}/F'_{bLS})}{1-[(f_{cDL}+f_{cLL})/F_{cE}]}\leq 1.0 \tag{5.4}$$

where f_{bEP} and F'_{bEP} are the bending stress demand and capacity, respectively due to earth pressure. f_{bLS} and F'_{bLS} are the bending stress capacity and demand, respectively due to vehicle surcharge. The allowable compressive stress under dead and live loads (F'_{cDL} and F'_{cLL}), and the allowable bending stress under earth pressure and live load surcharge (F'_{bEP} and F'_{bLS}) can be determined using design equations in the NDS. The equations are reproduced below.

$$F'_c = F_c C_D C_t C_u C_p C_{cs} C_{sp} \tag{5.5}$$

$$F'_b = F_b C_D C_t C_u C_F C_{sp} \tag{5.6}$$

In Equation (5.5), F_c is the reference allowable compression stress, C_p is the column stability factor, C_{cs} is the critical section factor, and C_{sp} is the single pile factor. In Equation (5.6), F_b is the reference allowable bending stress, and C_F is the size factor. In both equations C_D is the load duration factor, C_t is the temperature factor, C_u is the wood treatment factor (AFPA 2005). As mentioned above, F'_{cDL} and F'_{cLL} are distinguished by the load duration factor, C_D. F'_{bEP} and F'_{bEP} are also computed using duration factors equal to 0.9 and 1.15 respectively. The maximum stress developed in a pile cross-section due to applied loads namely, f_{cDL}, f_{bEP}, and f_{bLS} can be determined from analysis. Substituting these values into Equation (5.4) and solving for f_{cLL} yields the maximum allowable live load stress on an abutment timber pile.

5.2.2 Load Rating of FRP Retrofitted Piles

In this study, the half-shell FRP retrofit which was experimentally tested in Chapter 4 was considered as the primary strengthening measure. The thickness of the composite was varied as a parameter to quantify the relationship between FRP volume and the load rating. The retrofit scheme is illustrated in Figure 5.2.

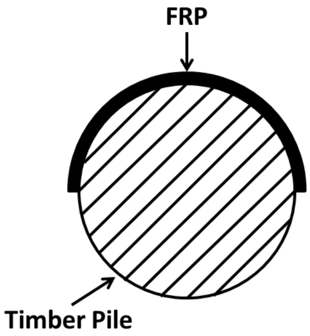

Figure 5.2 Half-shell FRP retrofit scheme considered in this study

The true bending strength of timber is difficult to estimate due to material nonlinearity and size effects (Buchanan 1984). Traditionally for timber members in bending, linear elastic behavior is assumed and the modulus of rupture is used as the allowable bending stress. The AASHTO LRFD Bridge Design Specifications use the modulus of rupture to define the nominal bending moment capacity of timber structural members (AASHTO 2012). A similar elastic design approach was adopted to compute the bending moment capacity of FRP retrofitted timber piles. The approach is illustrated in Figure 5.3 where E and A denote elastic modulus and cross-sectional area respectively, and n is the modular ratio of E_{FRP} to E_{wood}.

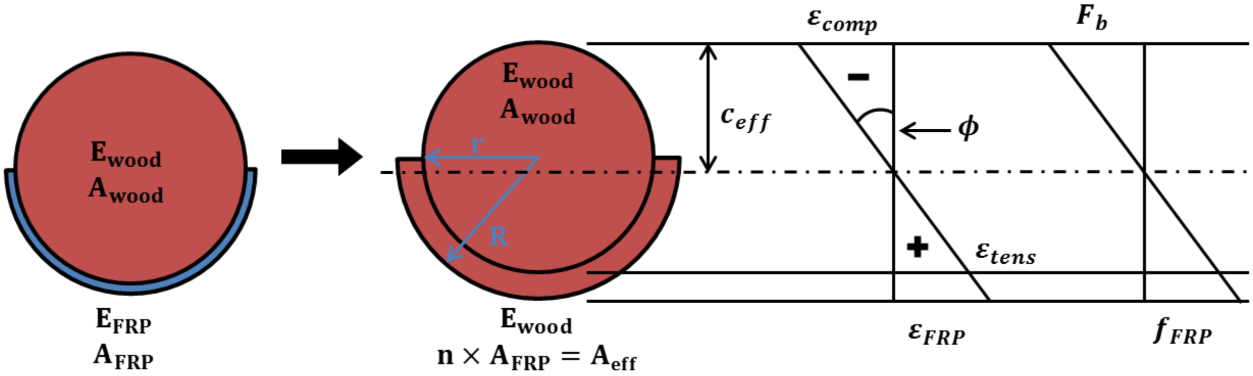

Figure 5.3 Elastic design approach for abutment pile FRP retrofit design

As shown, the bending moment capacity is computed assuming linear stress-strain behavior. The FRP composite is first transformed into an equivalent timber section using the modular ratio. Then the section moment capacity is determined from basic mechanics as

$$M = E_{wood} I_{eff} \phi = E_{wood} I_{eff} \frac{\varepsilon_{comp}}{c_{eff}} = E_{wood} I_{eff} \frac{(F_b / E_{wood})}{c_{eff}} \tag{5.7}$$

where, M is the bending moment capacity of the retrofitted section, E_{wood} is the timber pile elastic modulus, I_{eff} is the transformed section moment of inertia, c_{eff} is the distance from the extreme compressive fiber to the neutral axis, and ε_{comp} is the elastic strain at the extreme compressive timber fiber under bending computed using the allowable bending stress F_b and E_{wood}. Using FRP composites as tensile reinforcement as in this case can improve the strength of timber piles in bending but it will not directly improve their capacity under pure axial loading. The improved bending moment capacity can be translated into a modified allowable bending stress F_b^* by projecting the moment onto an unretrofitted timber pile section as shown in Figure 5.4.

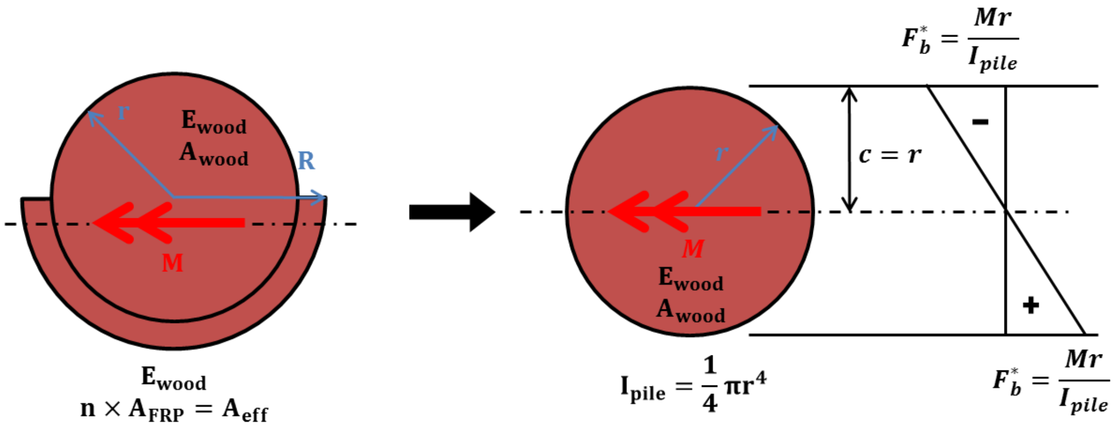

Figure 5.4 Projection of the bending moment obtained from transformed section analysis onto an unretrofitted timber pile section

The method described above assumes perfect bond between the FRP composite and timber pile. When evaluating the load capacity of FRP retrofitted timber piles, care should be taken to ensure adequate bond strength especially when the retrofitted pile has been exposed to deteriorative conditions for a long period of time.

5.3 ABUTMENT TIMBER PILE ANALYSIS

As seen above, load rating is a function of material strength, sectional properties, pile length, and the applied loads. In order to present the new load rating method in a more convenient manner without losing its generality, a simplified finite element (FE) model of an abutment timber pile was used to compute the load rating for a wide range of parameters. The results are compiled into a series of charts from which the maximum allowable live load stress can be conveniently estimated.

5.3.1 FE Model

The finite element analysis software, ABAQUS (Dassault Systèmes Simulia Corp. 2011) was used to develop a model of a single abutment timber pile. The dimension and detailing of the pile were based on a survey of existing timber pile bridges in the state of Illinois. Typical values were adopted from as-built construction drawings. Some of these drawings are provided in the Appendix. The standard pile was assumed to be prismatic with a diameter of 305 mm and 6.70 m in length from tip to pile head. In all consulted drawings the piles were embedded 305 mm into the pile cap with a specified minimum pile penetration depth of 4.57 m below grade.

The primary purpose of the FE model was to compute stresses in the timber pile under various load cases, namely, f_{cDL}, f_{bEP}, and f_{bLS}. The results were used in Equation (5.4) to determine the maximum allowable live load stress and develop the load rating charts. The load rating charts are based on a single pile in order to isolate the effect of global bridge geometric parameters such as skew and span length, which will influence the magnitude and distribution of axial loads among the piles. However, this is not a critical factor since each timber pile is load rated individually. The single abutment timber pile model is shown in Figure 5.5.

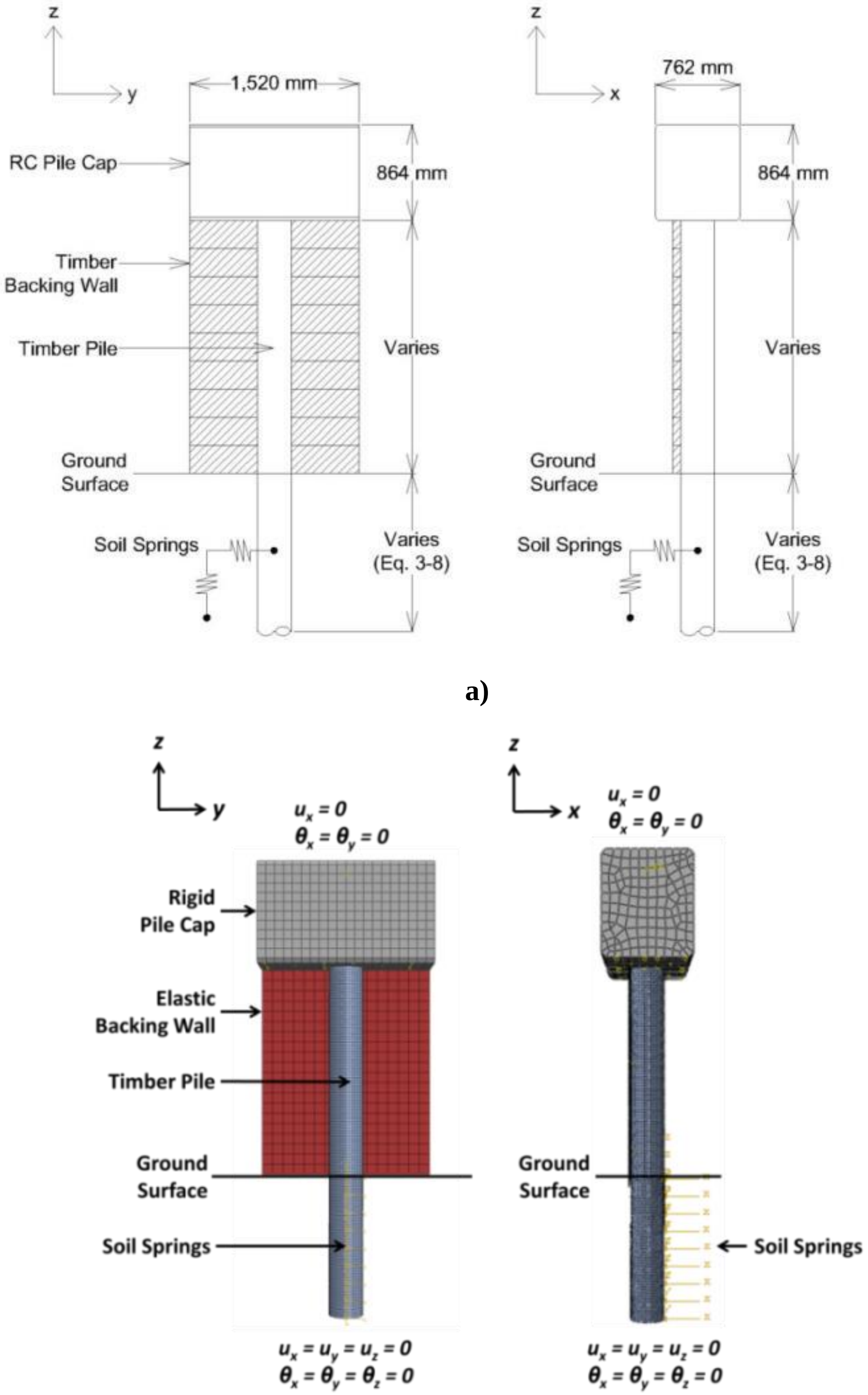

a)

b)

Figure 5.5 Single abutment timber pile model **a)** Schematic **b)** FE model showing boundary conditions at the top of the pile cap and at the pile tip

The timber pile was discretized using reduced integration 8 node linear brick elements. The material model was based on the numerical model from Borello et al. (2010). The material behavior of timber adopted in this study is plotted in Figure 5.6. This behavior is representative of typical timber stress-strain behavior applicable to many different species.

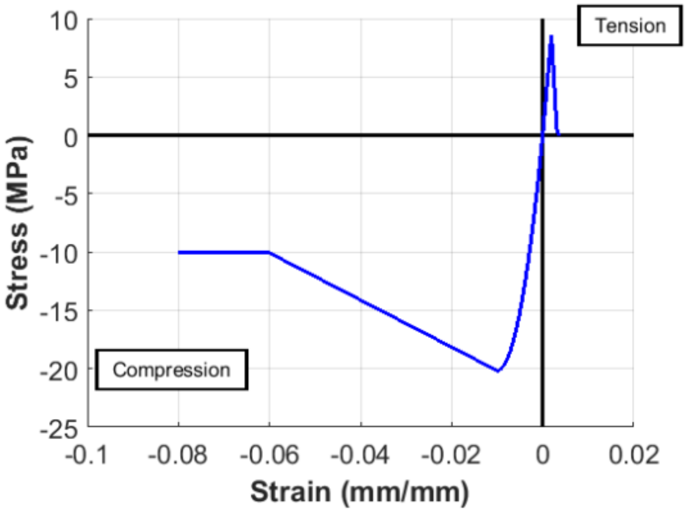

Figure 5.6 Timber material model

5.3.2 Soil-Structure Interaction

The soil-pile interaction was modeled as a Winkler foundation where discrete springs are used to represent skin friction and lateral resistance. Similar approaches were used by Borello et al. (2009) and Andrawes & Caiza (2011). The mechanical properties for the soil type used in this study (stiff to very stiff, low plasticity glacially overridden loams with variable gravel and cobble content) were obtained from field tests by Borello et al. (2009). The test results were used to develop simplified *p*-*y* curves. The trilinear model used for the lateral soil springs is shown in Figure 5.7.

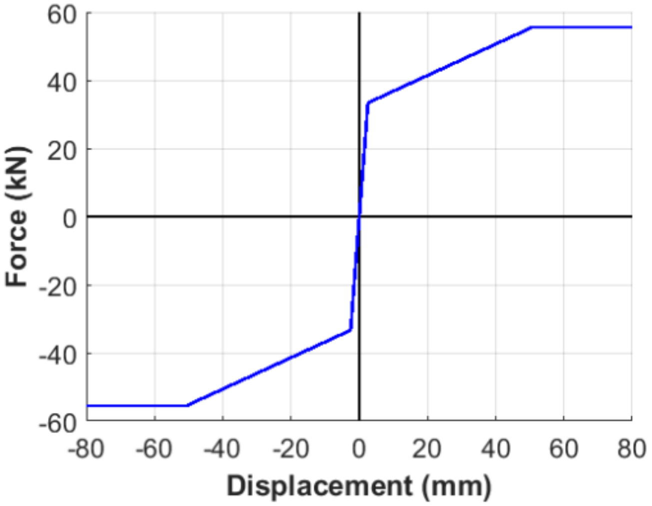

Figure 5.7 Soil spring model

To minimize the computational cost, it was assumed that the timber pile reaches fixity at a depth, f, based on Equation (5.8) rather than modeling the entire embedded length. This depth corresponds to the point where the maximum bending moment develops and a plastic hinge forms when sufficiently long piles in cohesionless soils are subjected to a lateral load (Broms 1964).

$$f = 0.82\sqrt{\frac{P}{\gamma D K_p}} \qquad (5.8)$$

In Equation (5.8), P is the total lateral force, γ is the soil unit weight, D is the pile diameter, and K_p is the Rankine passive earth pressure coefficient. Klaiber et al. (2004) showed that this approximation developed by Broms (1964) yields sufficiently accurate results in analyzing bridge timber piles. The soil springs were modeled using Cartesian connector elements in ABAQUS. Friction and lateral resistance spring pairs were spaced at 152 mm along the embedded length. The friction springs were assumed to behave in an elastic-perfectly plastic manner. The behavior of the friction springs was depth dependent. A yield force of 0.444 kN and yield displacement of 2.5 mm was used from the ground surface to a depth of 762 mm. From 914 mm to fixity a yield force of 10.453 kN and yield displacement of 2.5 mm were used.

5.3.3 Loading and Analysis Parameters

Four key parameters were considered in developing the load rating and FRP retrofit design charts: 1) dead load (DL), 2) unbraced pile length above the ground surface, 3) backfill soil unit weight, and 4) timber pile deterioration. The dead load acting on the single pile model was varied from 44.5 kN to 178 kN in 22.2 kN increments to capture a wide range of cases that may arise due to varying superstructure types, span length, and skew angle. The dead load was applied as a uniformly distributed pressure on the top surface of the pile cap.

The pile length extending above the ground surface can be a critical factor on the performance of abutment timber piles because it directly affects the magnitude of the lateral load from the backfill and also impacts its stability. The unbraced pile length was varied from 1.22 m to 2.44 m in 0.305 m increments.

The backfill dictates the magnitude of both the earth pressure (EH), and live load surcharge (LS) applied to the abutment backing. The equivalent-fluid method outlined in the AASHTO LRFD Bridge Design Specifications (AASHTO 2012) was used to calculate the earth pressure assuming level backfill. The equivalent soil unit weight was varied in 0.785 kN/m^3 increments from 4.713 kN/m^3 to 9.425 kN/m^3 to cover a range of soil conditions. Whereas the earth pressure varies linearly with depth, the live load surcharge is applied as a uniform lateral pressure. In accordance with the AASHTO Standard Specifications for Highway Bridges (AASHTO 2002), the magnitude of the live load surcharge was determined from a constant surcharge pressure equal to 610 mm of earth. For each equivalent soil unit weight, the coefficient of lateral earth pressure was back-calculated and used to determine the live load surcharge pressure. Both the earth pressure and live load surcharge were applied over the abutment backing wall and the backfill side of the abutment pile cap.

5.3.4 Deterioration of Timber Piles

Timber pile abutments are especially susceptible to severe cracking and decay due to soil-water-air interaction (Dahlberg et al. 2012). Based on an inspection of several field-extracted timber pile specimens, three common deterioration profiles were identified for consideration in this study. Each profile represents a pattern of section loss as illustrated in Figure 5.8. The severity of the damage in each profile was varied by changing the dimensions indicated. The overall level of damage was expressed as a percentage of the gross cross-sectional area, increasing by 10% of the gross cross-sectional area up to 30%.

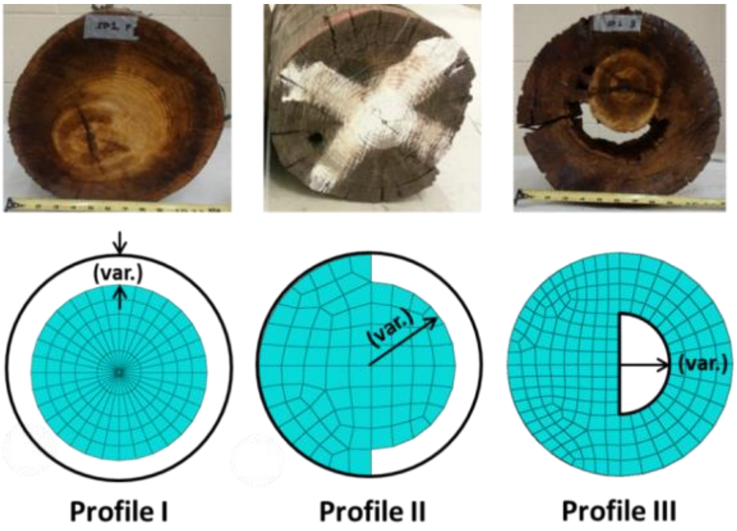

Figure 5.8 Timber pile deterioration profiles

Profile I is an external damage pattern uniformly affecting the entire pile circumference. Profile II represents external deterioration affecting only one half of the pile. Profile III represents a case of internal deterioration with a semi-circular profile centered at the pile geometric center. It was assumed that the damage does not affect the strength or mechanical properties of the wood in the remaining timber pile cross-section. When considering deterioration Profiles II and III in the FE analysis, the piles were oriented such that the voids were on the tension side since the strength of timber piles in bending is governed by tension. This also maximized the stresses in the cross-section. Although timber deterioration is a concern when the timber pile is exposed to wet-dry cycles both above and below grade, it was assumed to only affect the exposed portion of a pile above the ground surface (AWPI 2002). Where this assumption is not valid, load rating can still be performed using the same approach.

5.4 LOAD RATING CHARTS

The FE model shown in Figure 5.5 was used to compute the load rating of abutment timber piles with varying length, dead load, deterioration and backfill soil unit weight. Initially, the isolated effect of each parameter was considered by holding the other parameters constant. Results showed that the allowable centroidal live load stress varied almost linearly with respect to changes in the dead load. The effect of pile length on the load rating could be captured conservatively with a bilinear approximation. Therefore, it was established that the load rating charts could be limited to minimum and maximum dead loads of 44.5 kN and 178 kN, and pile lengths of 1.22 m, 1.83 m, and 2.44 m. Linear interpolation can be used for intermediate pile lengths and dead loads. The behavior was nonlinear with respect to backfill soil unit weight and the level of deterioration. In general, bending has a larger contribution to the P-M interaction in

Equation (5.4) than the axial loading. This is attributable to second-order amplification effects and the axial components being squared to capture the shifting of the neutral axis (Steiger & Fontana 2005). In addition, to generalize the load rating the charts are presented in terms of the allowable centroidal live load stress. The allowable live load stress (f_{cLL}) obtained from the charts can be used in Equation (5.2) to compute the load rating for any live load applied by the user. The load rating charts for 1.22 m, 1.83 m, and 2.44 m timber piles are plotted in Figures 5.9, 5.10, and 5.11, respectively.

Each curve in Figure 5.9, 5.10, and 5.11 represents the maximum allowable live load stress which the abutment timber pile can sustain for a given dead load, type/extent of deterioration, and backfill condition. As shown, the maximum allowable centroidal live load stress changes nonlinearly over the spectrum of backfill soil unit weight. The curves become shorter with increasing deterioration as the failure mode tends toward bending failure, significantly reducing the live load capacity.

Overall, a 1.22 m pile can sustain much higher lateral loads from earth pressure and live load surcharge even with high dead loads and damage to the pile cross-section compared to 1.83 m or 2.44 m piles. It is also important to note that increasing the length of abutment timber piles may have an impact on stability. Since abutment timber piles are typically not braced in the out-of-plane direction, second-order effects may cause long piles to become unstable. Considering undeteriorated timber piles under the same loading conditions, the allowable live load stress in a 1.83 m pile is up to 32% lower than that of a 1.22 m pile. Compared to a 1.83 m timber pile, the allowable live load stress for an undeteriorated 2.44 m timber pile is up to 87% lower.

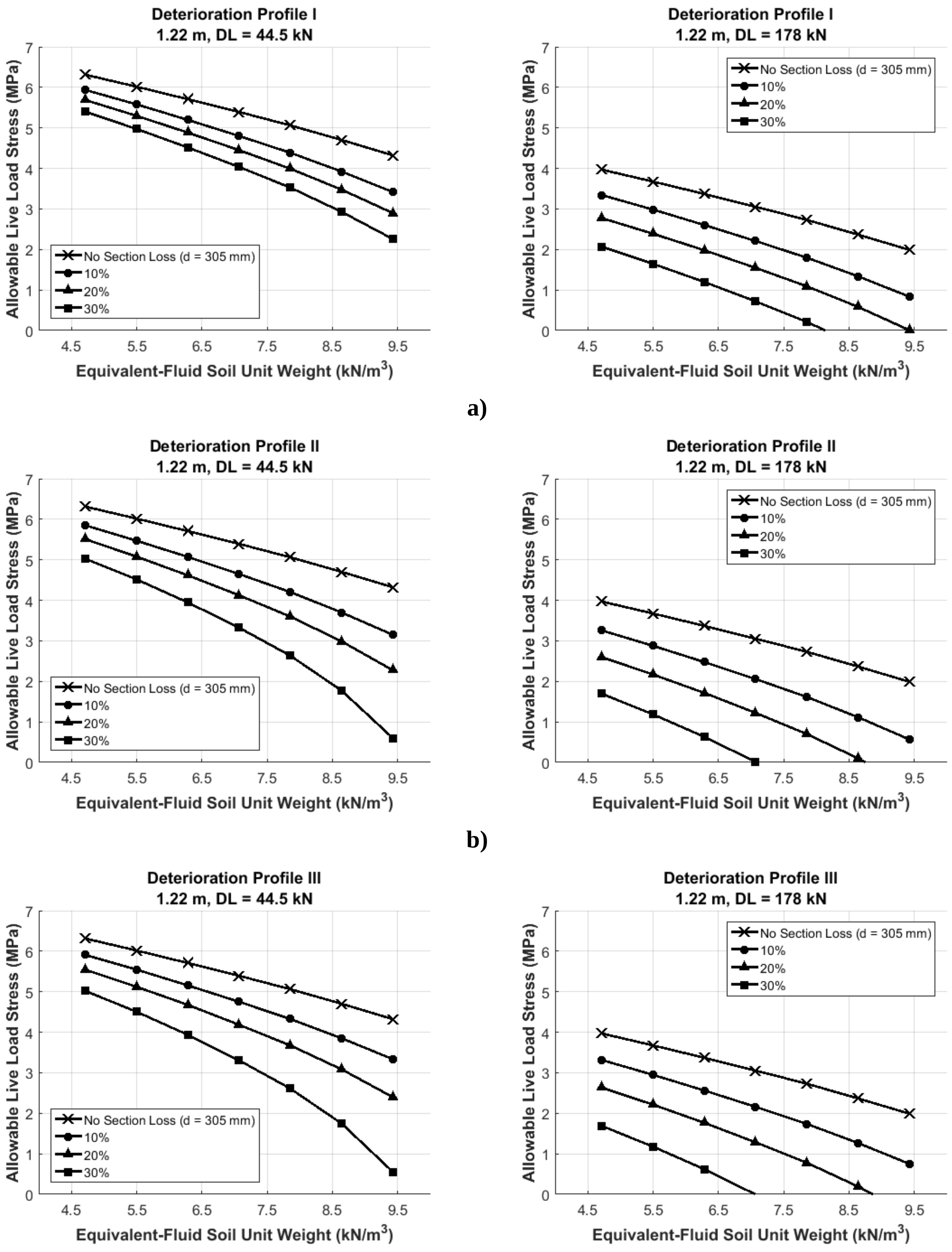

a)

b)

c)

Figure 5.9 Allowable live load stress charts for 1.22 m abutment timber piles with different dead loads and deterioration profiles **a)** Profile I **b)** Profile II **c)** Profile III

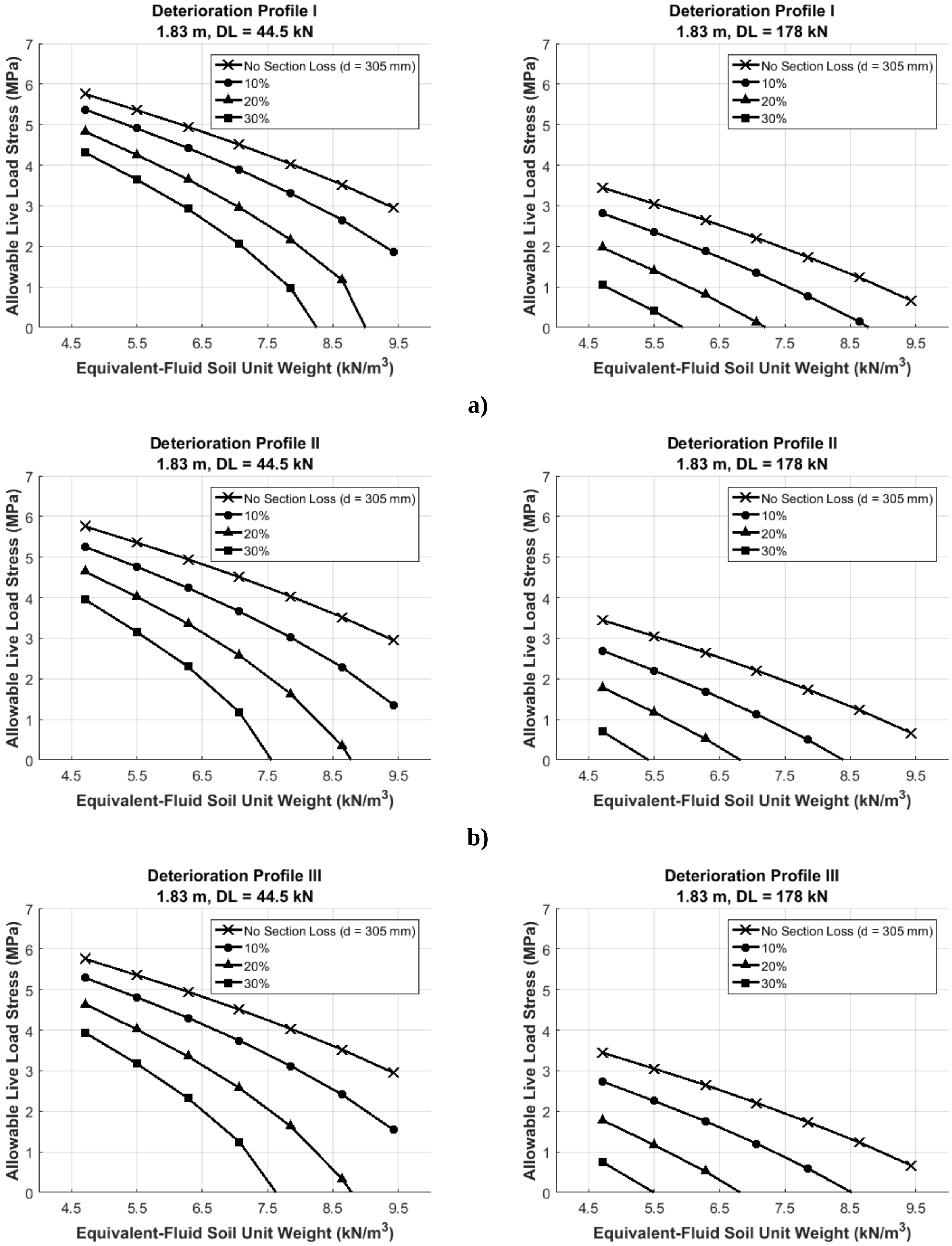

a)

b)

c)

Figure 5.10 Allowable live load stress charts for 1.83 m abutment timber piles with different dead loads and deterioration profiles **a)** Profile I **b)** Profile II **c)** Profile III

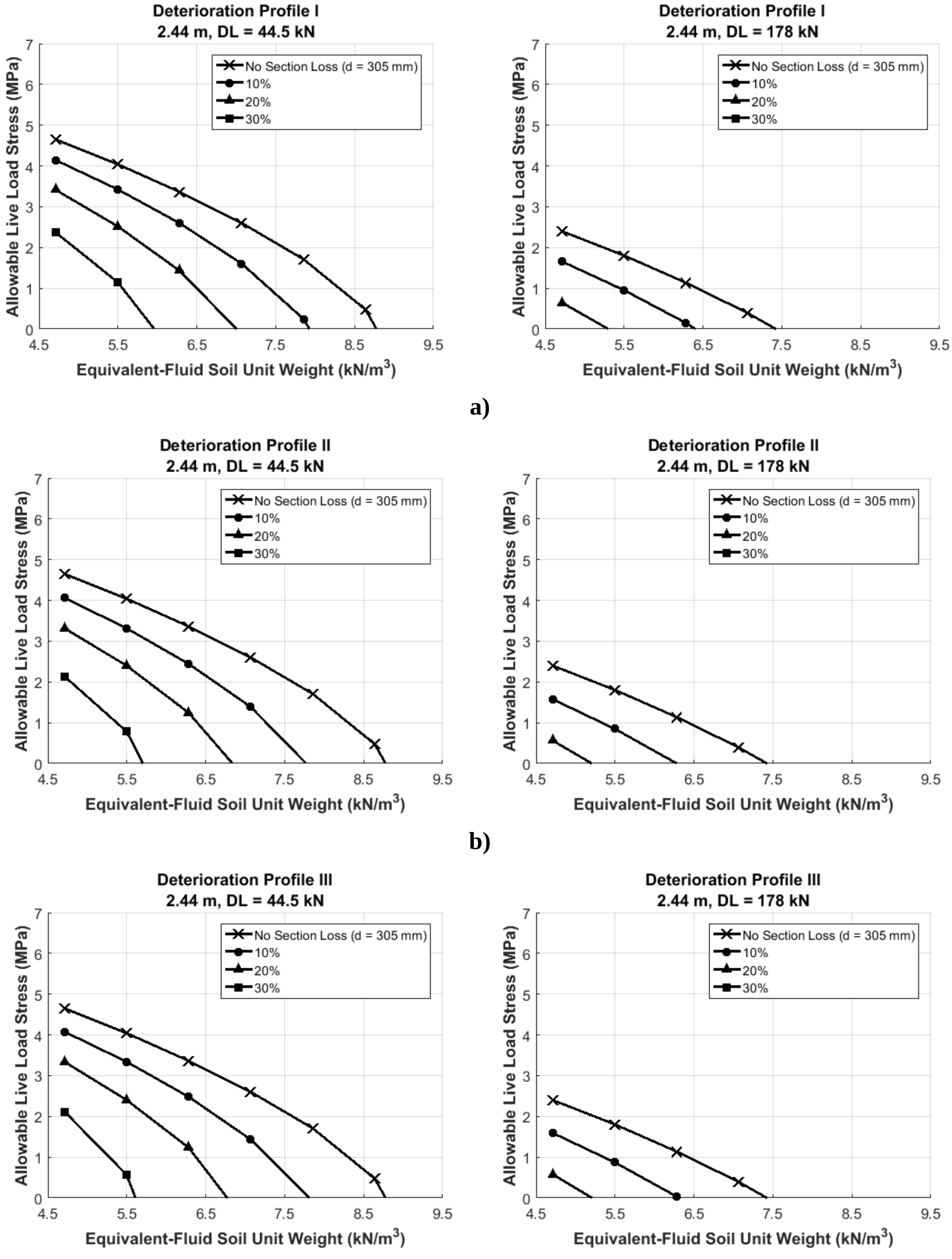

a)

b)

c)

Figure 5.11 Allowable live load stress charts for 2.44 m abutment timber piles with different dead loads and deterioration profiles **a)** Profile I **b)** Profile II **c)** Profile III

In general, for all three deterioration profiles, the allowable live load stress decreases exponentially with increasing level of deterioration. The reductions are most noticeable in Profiles II and III. Comparing the deterioration profiles, it can be seen that Profile I generally yields less critical results in comparison to Profiles II and III. Profiles II and III show similar results overall. For the 44.5 kN dead load case, the allowable live load stress for a pile with deterioration Profiles II or III can be up to 75% lower than if the same pile had deterioration Profile I. Increasing the dead load even further amplifies this effect. Internal deterioration as depicted by Profile III can be especially problematic as they may be very difficult to detect without specialized tools.

The dead load can also have a considerable effect on the load rating. For the 1.22 m and timber pile cases with no deterioration, increasing the dead load from 44.5 kN to 178 kN, reduces the allowable live load stress by at least 37%. For the 2.44 m pile case it is reduced by at least 48%. With increasing deterioration, this reduction becomes even more severe.

To use the load rating charts in Figures 5.9, 5.10 and 5.11, the user must first determine the abutment height, dead load, backfill soil unit weight, and the type and extent of deterioration to the pile cross-section. Based on these parameters, linear interpolation can be used between the appropriate charts with respect to pile length and dead load to determine the maximum allowable live load stress. This value can be compared to the applied live load stress using Equation (5.2) to determine the structural adequacy of the abutment pile. This load rating procedure is demonstrated in the next section. Although the load rating charts in Figures 5.9, 5.10, and 5.11 can be used for a wide range of typical timber pile bridge abutments, their applicability to each specific case must be evaluated. For cases where the load rating charts cannot be used, load rating can still be performed using Equation (5.4).

5.5 LOAD RATING EXAMPLE

5.5.1 Prototype Bridge

To demonstrate the proposed load rating technique, a prototype bridge model was developed based on typical characteristics of timber pile bridges in the state of Illinois. The bridge model consists of two 9.36 m long spans supported on timber pile substructure with seven round Red Oak timber piles. A constant diameter of 305 mm was assumed for all timber piles in the model. The precast deck slab-beams are 406 mm thick with a 127 mm thick wearing surface. The deck is connected to the reinforced concrete pile-cap by dowel bars. The prototype timber pile bridge is illustrated in Figure 5.12.

As shown in Figure 5.12, the deck measures 9.14 m from edge to edge and carries two 3,048 mm wide traffic lanes. The timber abutment backing walls extend from the bottom of the pile cap to the top of the soil. It was assumed that all abutment piles had deterioration Profile II with 20% damage to the cross-section. The timber piles supporting the bent were assumed to be undeteriorated with 305 mm diameter.

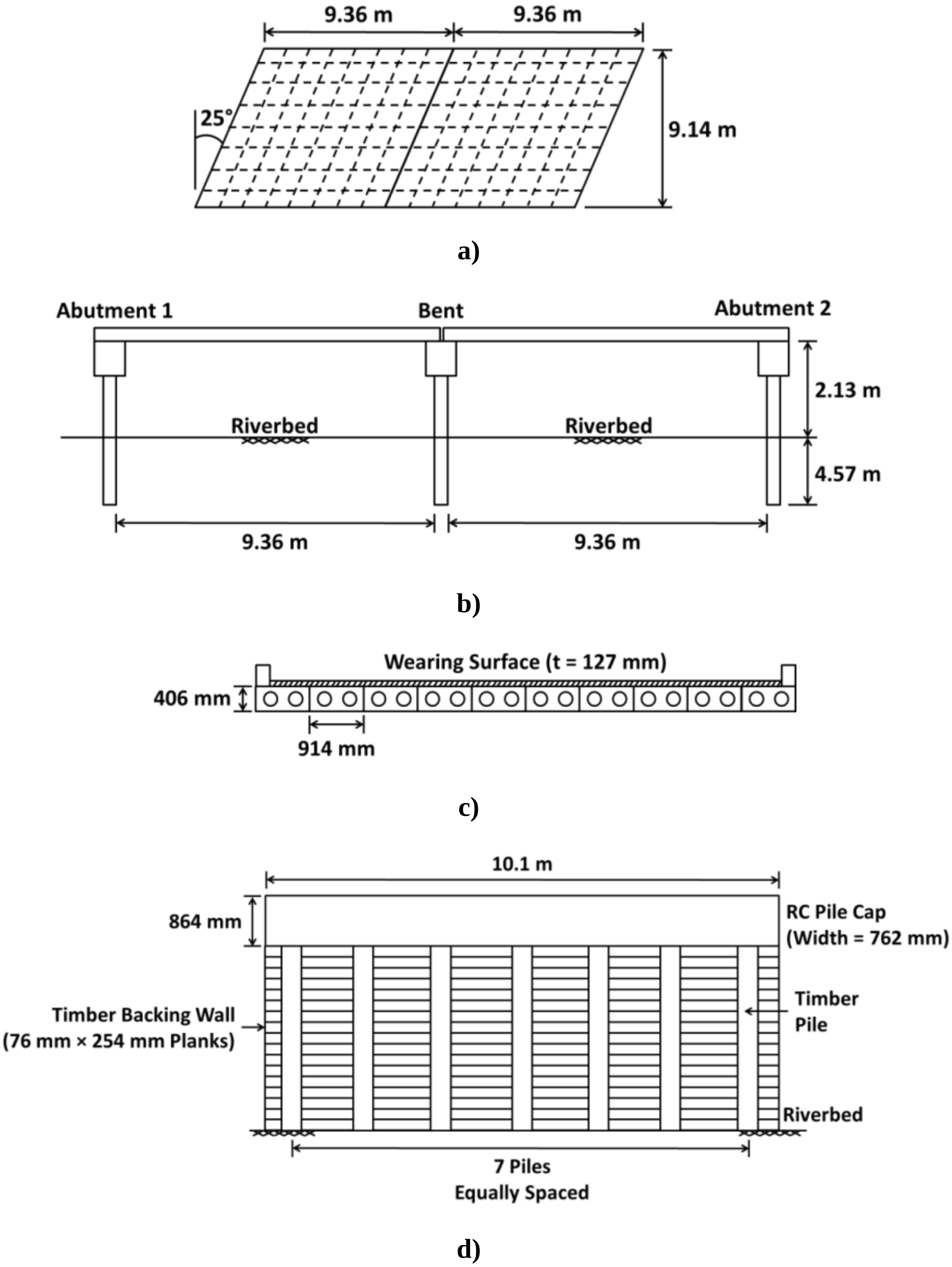

Figure 5.12 Prototype timber pile bridge **a)** Plan view of deck **b)** Elevation **c)** Typical concrete slab-beam superstructure **d)** Timber pile abutment

5.5.2 FE Model and Analysis

The FE bridge model was developed and analyzed using ABAQUS. The full FE model is shown in Figure 5.13.

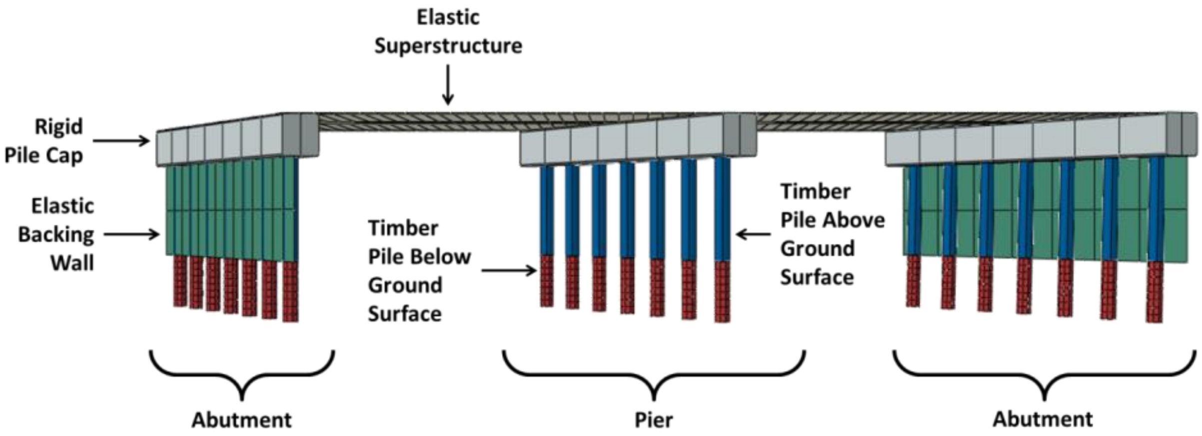

Figure 5.13 Prototype timber pile bridge FE model

The same material properties and soil-structure interaction assumed in the abutment pile model was adopted. The precast concrete deck was modeled using linear elastic shell elements with elastic modulus equal to 26,200 MPa, a typical value for concrete. An equivalent shell thickness was estimated from the flexural stiffness of the precast slab-beam. Tie constraints were used to constrain the deck to the pile-cap. This is a reasonable assumption since the relative deformation between the deck and substructure is very small under normal loading conditions. An equivalent-fluid soil unit weight of 6.283 kN/m^3 was assumed for the earth pressure and live load surcharge. The HS20-44 design truck with rear axles spaced at 4,267 mm was adopted for the live load. To maximize the live load effects on the abutment piles two design trucks were configured as shown in Figure 5.14.

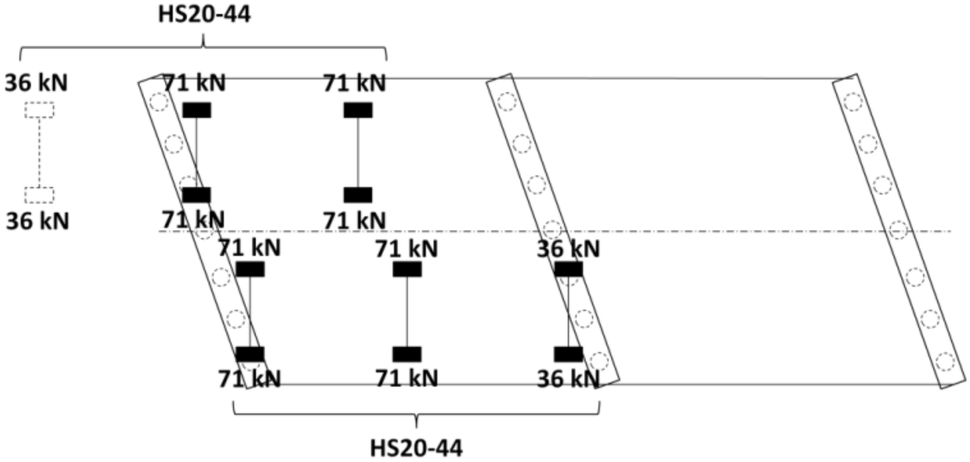

Figure 5.14 Live load vehicle load pattern

Using NDS reference design values for Red Oak, the allowable compressive stresses, F'_{cDL}, and F'_{cLL}, are calculated using Equation (5.5) to be 6.76 MPa and 8.51 MPa, respectively for 2.13 m long piles. The allowable bending stress under earth pressure, F'_{bEP} is equal to 15.20 MPa. The allowable bending stress under live load surcharge, F'_{bLS}, is equal to 19.43 MPa. Analysis showed that the centroidal compressive stress demand under live load, f_{cLL}, ranged for all seven piles between 0.65 MPa and 1.19 MPa. The centroidal dead load stress, f_{cDL}, ranged for the seven piles from 0.57 MPa to 1.52 MPa, this yields a dead load between 51.8 kN and 137.9 kN. To determine the allowable live load stress, linear interpolation was used to first interpolate for the dead load between the 1.83 m and 2.44 m pile curves corresponding to 20% deterioration with Profile II (shown in Figure 5.10 b) and 5.11 b)). Then linear interpolation was used between these values for the length. The results from the proposed load rating technique are compared to the conventional approach in Table 5.1.

Table 5.1 Analysis results and load rating of the prototype bridge model

	f_{cDL} **(MPa)**	f_{cLL} **(MPa)**	$f_{cLL}\|_{max}$ **(MPa)**	**Proposed Load Rating**	**Conventional Load Rating**
Pile	From Analysis	From Analysis	Charts	Eq. (5.2)	Eq. (5.1)
1	0.57	0.65	2.47	3.80	9.52
2	0.72	0.74	2.34	3.16	8.16
3	0.86	0.83	2.21	2.66	7.11
4	1.00	0.92	2.09	2.27	6.26
5	1.14	1.01	1.96	1.94	5.56
6	1.29	1.10	1.83	1.66	4.97
7	1.43	1.19	1.70	1.43	4.40

Pile 1 is at the acute angle side of the deck and Pile 7 is at the obtuse end. Due to the bridge skew, dead and live load stress demands are unevenly distributed. As can be seen, Pile 7 is the most critical. Compared to the conventional method, load ratings obtained using the proposed load rating method is lower by up to 67%. This shows that evaluating the allowable live load capacity of bridge timber piles based solely on axial loads is highly unconservative.

5.6 FRP RETROFIT DESIGN

The proposed load rating method and the modified allowable bending stress procedure outlined earlier were used to determine the thickness of FRP required (t_{FRP}) to restore the critical load rating of deficient piles to the minimum acceptable threshold of 1.0. The single abutment pile model used to develop the load rating charts was used. It was assumed that the FRP is applied over the entire length of the pile above the ground. Only deterioration Profile I and the half-shell FRP retrofit shown in Figure 5.2 are discussed here. An undeteriorated timber pile diameter of 305 mm was used as the basis. The HS20-44 live load pattern shown in Figure 5.14 was assumed. To develop the design charts, the load rating procedure for FRP retrofitted abutment timber piles discussed above was applied in reverse. First the modified allowable bending stress, F_b^*, required to increase the load rating to the minimum acceptable level of 1.0 was determined. Then, the FRP thickness needed to achieve this value was computed. Similar to the load rating charts in Figure 5.9, 5.10 and 5.11, FRP design charts are provided for 1.22 m, 1.83 m, and 2.44 m piles only under 44.5 kN and 178 kN dead loads. Linear interpolation can be used for other values. The timber pile was assumed to be Red Oak with an elastic modulus of 4,550 MPa and reference allowable bending stress, F_b, of 16.89 MPa. Since FRP composites vary in stiffness and strength depending on the constituents, the FRP thickness in the design charts are normalized with respect to the FRP composite elastic modulus. To obtain the actual FRP thickness, the normalized thickness shown on the y-axis must be divided by the FRP elastic modulus (E_{FRP}). Figure 5.15 shows the FRP thickness required to retrofit timber abutment piles with varying levels of deterioration.

In Figure 5.15, the different line types represent pile length and the markers indicate the level of damage. FRP retrofitting is needed for 1.22 m piles only in cases with high dead load and earth pressure. For the 1.83 m pile case with 44.5 kN dead load, FRP retrofits are required for damage exceeding 20%. Even at low dead loads, a 2.44 m timber pile may require retrofitting if the deterioration exceeds 10% of the cross-sectional area. For a given backfill soil condition, increasing the dead load from 44.5 kN to 178 kN increases t_{FRP} by more than 90% for 1.83 m and 2.44 m piles. Increasing the pile length from 1.22 m to 1.83 m increases the required FRP thickness by at least 45%. Increasing the pile length from 1.83 m to 2.44 m leads to a minimum of 20% increase in t_{FRP}. The half-shell FPR retrofit offers a relatively cheap and simple retrofitting method and the charts plotted in Figure 5.15 provide design estimates for various situations.

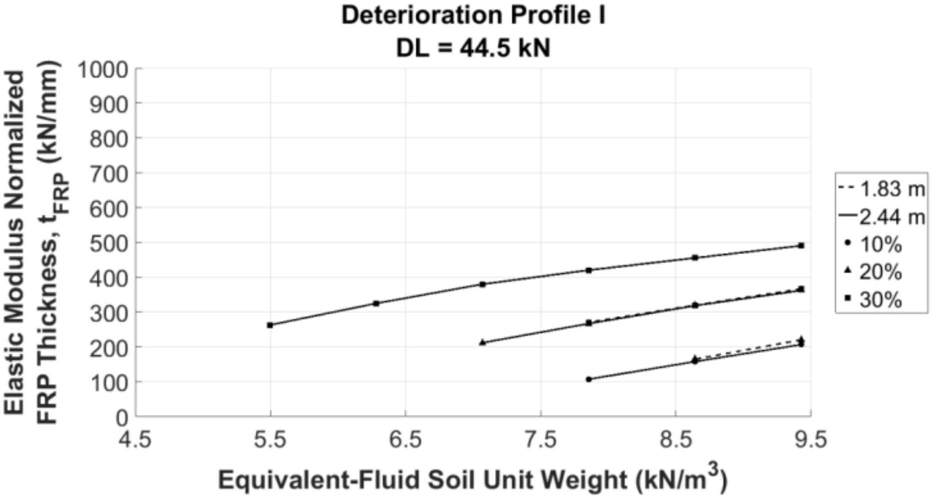

a)

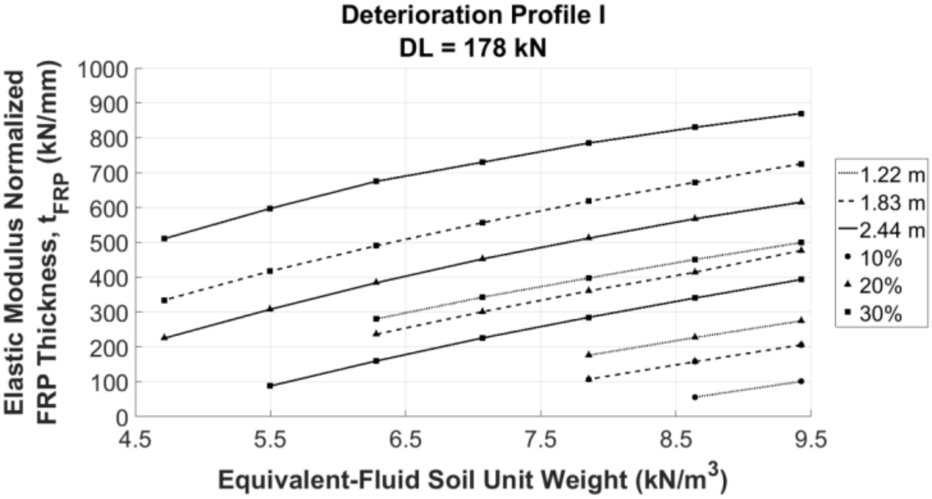

b)

Figure 5.15 Volumetric ratio of FRP required to retrofit deficient abutment timber piles with deterioration Profile I **a)** 44.5 kN dead load **b)** 178 kN dead load

5.7 SUMMARY OF CHAPTER 5

This chapter presented a modified allowable stress load rating method for deteriorated and FRP retrofitted abutment timber piles which accounts for combined axial-flexural loading. The load rating method and FRP retrofitting approach introduced in this chapter can be applied to different bridge geometries, loading conditions, and timber pile conditions to estimate the in-situ structural capacity, and develop FRP retrofit design charts that engineers can use to make repair/retrofit decisions. The main outcomes from the study are summarized below.

- Both pile length and the magnitude of dead load can have considerable effects on the load rating of an abutment timber pile. Up to 87% reduction in the allowable live load stress can occur in undeteriorated timber piles if the pile length is increased from 1.83 m to 2.44 m. Increasing the pile dead load from 44.5 kN to 178 kN can reduce the allowable live load stress in an undeteriorated timber pile by at least 37%.
- Overall, deterioration Profile I yields less critical results compared to Profiles II and III. For severe deterioration, Profiles II and III can yield up to 75% lower allowable live load stress than Profile I with a 44.5 kN dead load.
- Results of the load rating example of the prototype bridge with deteriorated abutment timber piles showed that compared to the conventional load rating method, the proposed load rating method gives lower ratings by up to 67%.
- For 1.22 m piles, FRP retrofitting is not needed with dead loads less than 44.5 kN. For 1.83 m piles with a 44.5 kN dead load, FRP retrofits are needed if the deterioration exceeds 20%. Overall, increasing the pile length from 1.83 m to 2.44 m will lead to a minimum of 20% increase in FRP thickness.

CHAPTER 6

MULTI-HAZARD ASSESSMENT AND RETROFIT OF DETERIORATED TIMBER PILE BRIDGES

Structural design has always been based on typical service loading conditions and isolated hazards such as earthquake loading or wind loads. However, recent natural and man-made disaster events have highlighted the need to consider multiple hazards in structural design. In particular, earthquake-tsunami events such as the 2004 Indian Ocean Earthquake-Tsunami and the 2011 Tohoku Earthquake-Tsunami, clearly demonstrated that many existing structures simply did not have the capacity to withstand the sequential action of these two hazards. While the isolated risk of earthquakes has been studied thoroughly over the years, there is a comparative lack of knowledge when it comes to the response of structures to tsunami loading. Although most recent earthquake-tsunami scenarios have occurred elsewhere in what is known as the Ring of Fire, vulnerability of the Pacific Coast of the United States to such events is well understood.

The number of timber pile bridges in the Pacific Coast states of Alaska, Washington, Oregon, and California number in the several thousands, most of which are at high risk of failure in the event of an earthquake-tsunami scenario given their age and simple design lacking in robustness and redundancy. This study investigates the performance of a typical unbraced timber pile bent under a suite of earthquake-tsunami scenarios. A prototype bridge is developed based on existing designs and the effects of pile section loss, and FRP retrofitting are also evaluated. OpenSees and with its new PFEM capabilities is used to conduct sequentially simulate the earthquake and tsunami hazards. Results show that even a modest level of timber deterioration can considerably affect the capacity of timber pile bridges under earthquake-tsunami loading. However, the FRP retrofitting technique considered in this study shows significant improvements can be achieved in terms of earthquake and tsunami capacity by strengthening a few selected timber piles. Although this specific study is focused on timber pile bridges, the methods and findings are not limited by the type of material and can be fully extended to other coastal structures.

6.1 PFEM CODE DEVELOPMENT

PFEM was chosen as the ideal method for earthquake-tsunami simulations because of its efficiency in solving FSI problems and it is a natural extension of conventional solid finite element formulations. However, no analysis program was readily available at the early stages of this research and an analysis code was initially developed in MATLAB to solve FSI problems with incompressible fluids. The code follows the fundamental PFEM formulation described in detail in many different sources in the literature (Idelsohn et al. 2004; Oñate et al. 2004; Idelsohn et al. 2006 among others). The governing equations are discretized using linear, equal-order interpolations for velocity and pressure. At each time step, a new mesh is generated using a very efficient algorithm called *Triangle* (Shewchuk, 1996), and the boundaries of the fluid domain are identified using the alpha shape method (Edelsbrunner & Mücke 1994).

There are two main difficulties involved in the solution of the discretized PFEM equations. First is the fact that elements with equal-order approximations for velocity and pressure are known to be unstable in the incompressible limit which can lead to pressure oscillations (Idelsohn et al. 2006). In the classical PFEM formulation, stabilization of the incompressibility condition is achieved using a finite calculus (FIC) formulation where a stabilizing term is added to the conservation of mass equation (Oñate et al. 2004). The second issue with the PFEM solution procedure is that the discretized system is ill-conditioned due to the coupling of the velocity and pressure fields. The fractional step method (FSM) is used to resolve this issue. The FSM is a staggered solution scheme where the velocity and pressure are separated into smaller systems that are better conditioned and simpler to solve (Idelsohn & Oñate 2010). Several patch test and validation problems were solved during the development of the PFEM code to verify its accuracy. Three illustrative examples are shown below.

6.1.1 Dam-Break Flow

The dam-break problem is a widely studied verification problem in fluid mechanics. The example considered here consists of a 146 mm × 292 mm column of water breaking and flowing under gravity. Water density, ρ_f, and viscosity, μ, were taken as 1,000 kg/m^3 and 0.001 kg/m·s respectively. The water column was discretized using 800 fluid particles and the simulation proceeded with a time step of 0.001 seconds. This problem was originally examined experimentally and analytically by Koshizuka and Oka (1996). The initial problem setup and simulation are shown in Figure 6.1.

As can be seen, the analysis fully captures splashing and spraying of the water as the flow breaks on the impermeable boundary at the downstream end. To verify the accuracy of the simulation, the evolution of the flow was compared to the experimental results in Koshizuka and Oka (1996). Figure 6.2 a) and b) show the location of the leading edge and the top of the water column over time respectively. The results show good agreement.

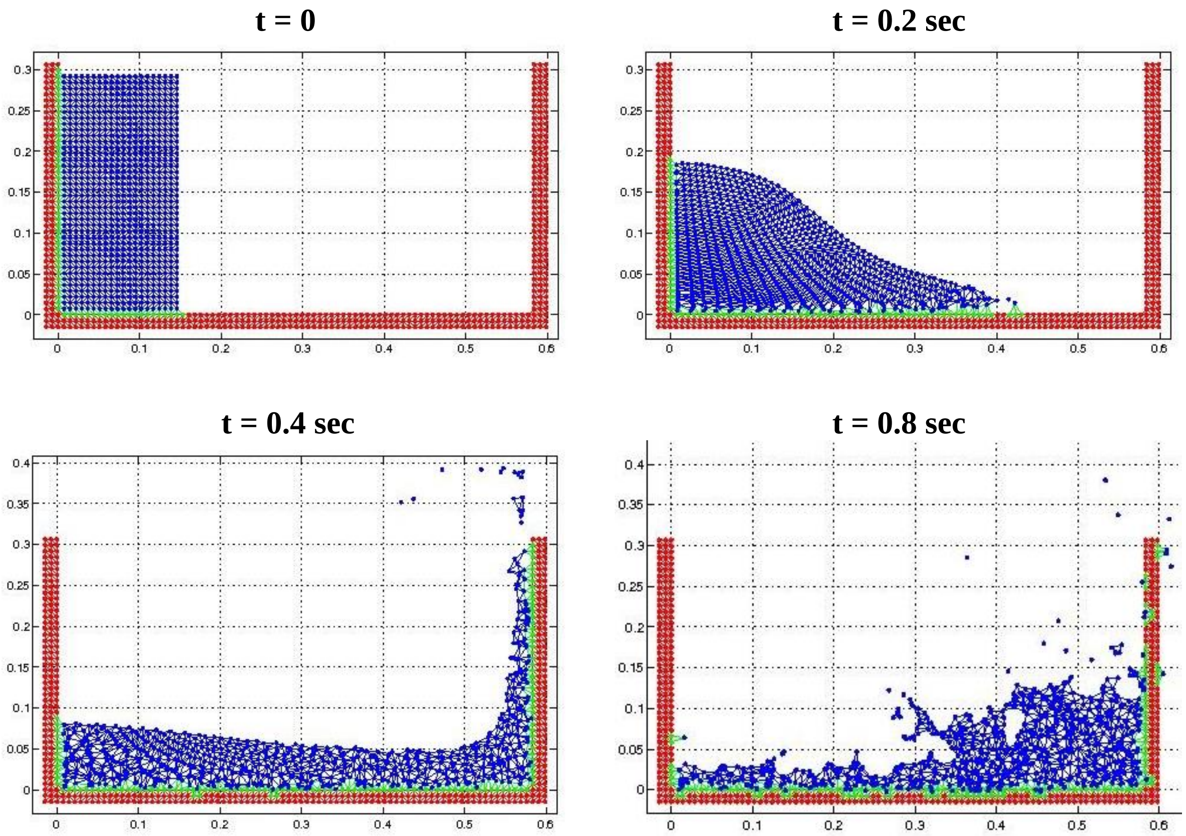

t = 0

t = 0.2 sec

t = 0.4 sec

t = 0.8 sec

Figure 6.1 Dam-break simulation

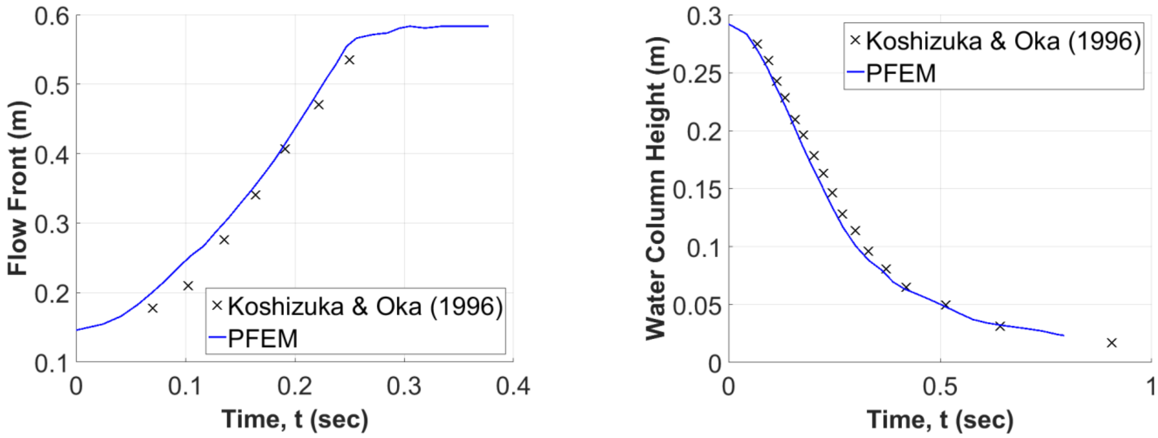

a)

b)

Figure 6.2 Comparison of PFEM dam-break simulation to Koshizuka & Oka (1996) experimental results

6.1.2 Elastic Column Impact

In this example the same water column considered in the example above impacts an elastic column. The column measures 0.012 m in width, 0.08 m in height, and is made up of a material with density, $\rho_s = 2{,}500$ kg/m^3, elastic modulus, $E = 10^6$ MPa, and Poisson's ratio, $\nu = 0$. The column was discretized using 120 linear triangular elements. Snapshots from the simulation are shown in Figure 6.3.

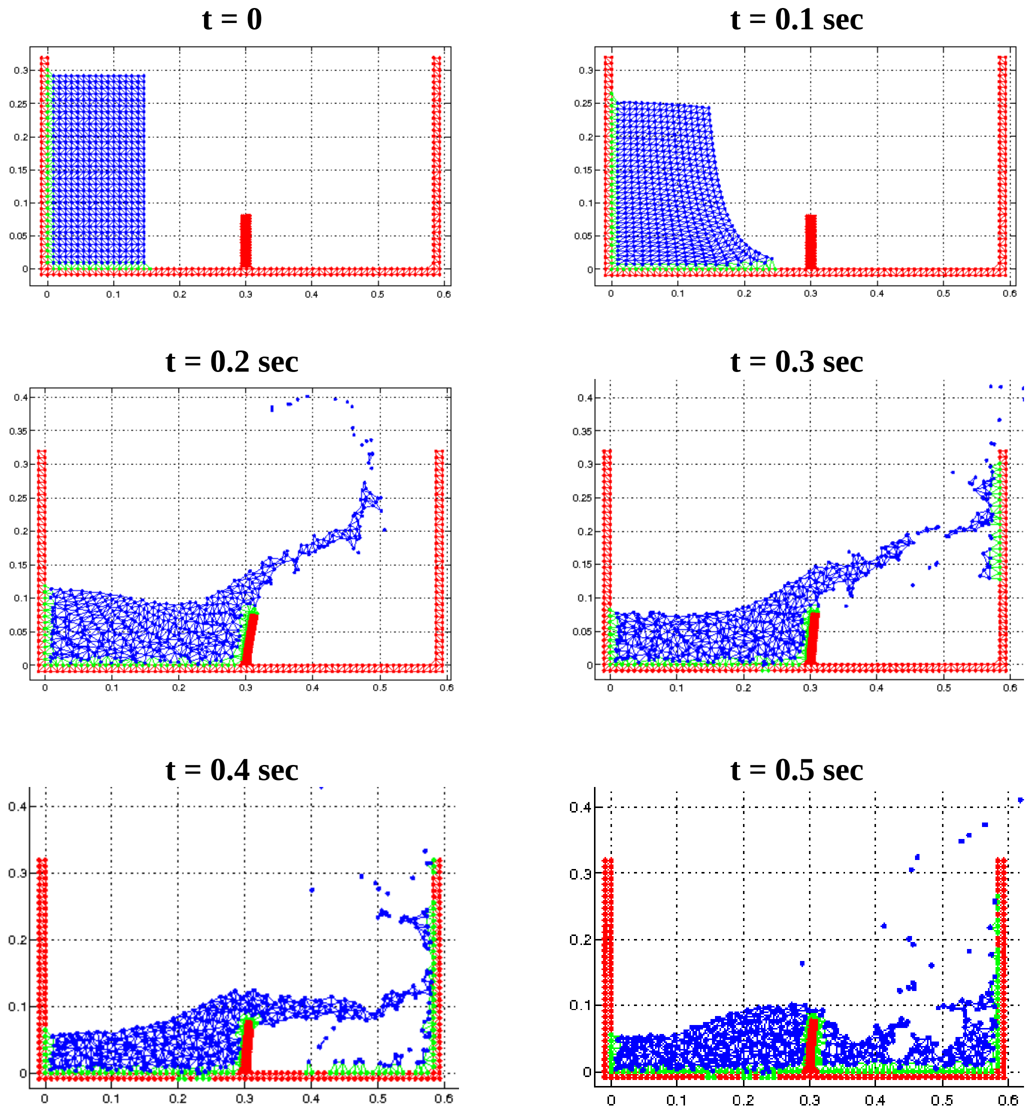

t = 0

t = 0.1 sec

t = 0.2 sec

t = 0.3 sec

t = 0.4 sec

t = 0.5 sec

Figure 6.3 Dam-break flow impacting an elastic column

The column response was compared to the results by Walhorn et al. (2005) which used space-time finite element method to solve the problem. To provide another point of comparison, the problem was also analyzed using arbitrary Lagrangian-Eulerian (ALE) formulation in LS-DYNA, a commercially available finite element analysis software (LSTC 2015). The deflection of the column tip is compared in Figure 6.4.

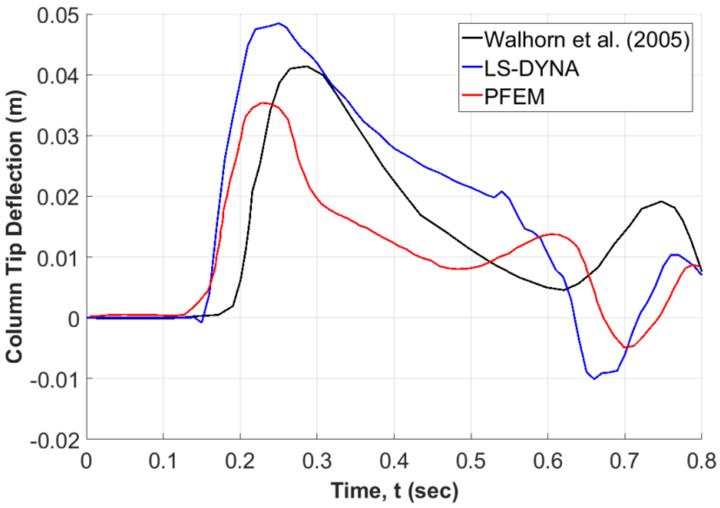

Figure 6.4 Elastic column tip deflection

The results from all three simulations are in general agreement with each other but there is a notable difference in the magnitude of the column displacement with the column response from the PFEM code appearing to be stiffer than the other two cases. This may be due to the combination of poor performance of three-node triangles in bending and the relative coarseness of the mesh used in PFEM.

6.1.3 Free-Surface Flow with Small Waves

The last example was considered to test the conservation of mass. The problem consists of a 1 m × 1 m volume of water with small initial waves at the free surface with a height of 0.1 m.

The density, ρ_f, and viscosity, μ, of the water were taken as 1,000 kg/m^3 and 0.001 kg/m·s respectively. The fluid domain was discretized into a coarse 20 × 20 mesh of triangular elements with no remeshing. Slipping conditions were applied on the bottom and side boundaries of the fluid domain. The simulation is shown in Figure 6.5.

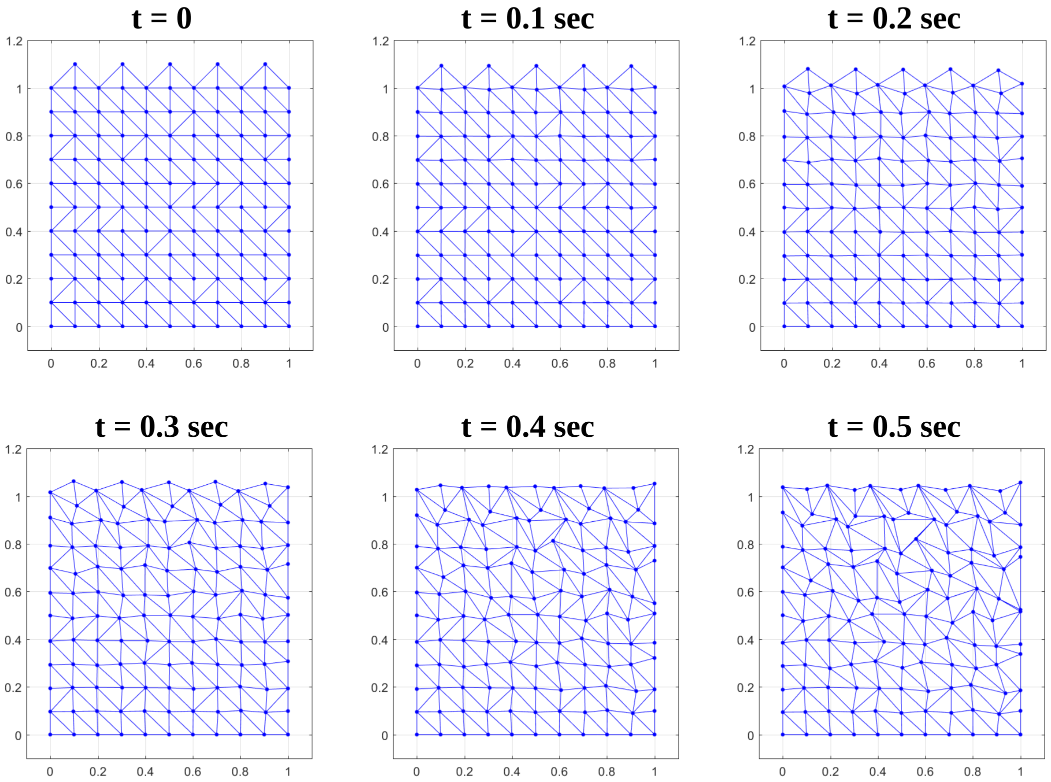

Figure 6.5 Small wave problem at different time steps

As noted in Idelsohn & Oñate (2010), although it appears simple, this is a very difficult problem to solve. The analysis was terminated at approximately 0.5 seconds due to excessive mesh distortion. It is well known that the classic FSM leads to mass loss in free-surface flow problems. Figure 6.6 shows the fluid pressure at t = 0.5 sec, and the mass loss represented as change in fluid volume. While the mass loss effect was not as severe as reported in Idelsohn &

Oñate (2010) by the end of the simulation, the fluid domain lost approximately 1.5% of its original mass.

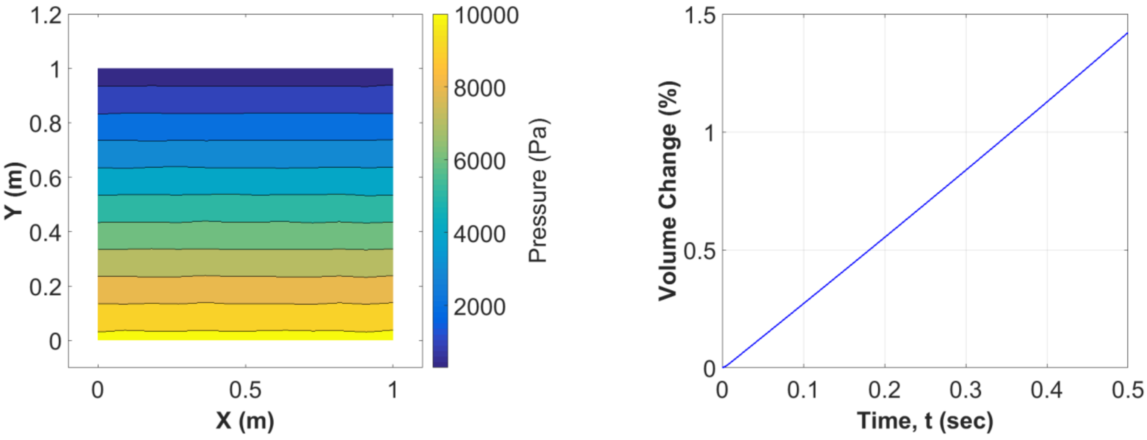

a) **b)**

Figure 6.6 a) Fluid pressure at t = 0.5 sec **b)** Fluid volume change

6.1.4 Remarks on the MATLAB Code

The PFEM implementation in MATLAB was used to test the applicability of PFEM to earthquake-tsunami simulations as well as serve as a prototype for developing a more robust and computationally efficient PFEM code. The code satisfied these ends but some crucial limitations in its capability should be noted. Firstly, it is difficult to define problems that are geometrically complex and the only element type available is the three-node triangle. Secondly, as shown above, the traditional FSM is known to suffer mass loss problems. Improved FSM are described in Idelsohn & Oñate (2010), and Zhu & Scott(2014a) but these methods were not implemented. Lastly, MATLAB was used for its simplicity and built-in libraries but for executing a large number of complex subroutines or functions it is very inefficient because MATLAB is an interpreter.

Even with its limitations, developing this code was an enormous task but provided critical insight into how it can be applied to earthquake-tsunami simulations and how it can be improved. However, expanding its capabilities or translating it into a different programming language was outside the scope of this research. In 2015 Zhu & Scott (2014b) implemented a robust PFEM formulation into OpenSees which provided a comprehensive platform on which to carry out this research. OpenSees is an open source finite element analysis software widely used for earthquake simulations. Taking advantage of the newly incorporated PFEM capabilities, the earthquake-tsunami simulations in this study were all completed using OpenSees.

6.2 PROTOTYPE TIMBER PILE BRIDGE

6.2.1 Description

The as-built drawings of several existing timber pile bridges were studied to establish a prototype bridge for this study by merging the most common characteristics. The prototype bridge is illustrated in Figure 6.7. The prototype bridge consists of precast deck slabs supported on timber pile substructure with reinforced concrete pile caps. The deck slabs are simply-supported on the pile caps with fabric bearing pads and dowel connections. In this study, only the transverse response of the bridge is considered. Since tsunami impact in the transverse direction will likely induce the highest forces, the accumulation of damage in earthquake-tsunami hazards could be the most extreme in the transverse direction. Furthermore, majority of the forces generated by a transverse tsunami flow will be resisted by the bent. Therefore, the numerical simulations in this study were focused on the response of the bent only. The span length and deck width assumed for the bridge were 11 m, and 10.67 m, respectively. The timber pile bent model is shown in Figure 6.7 b). All existing drawings consulted in developing the bridge model specified a minimum pile penetration depth of 4,570 mm independent of soil condition and required test piles to be driven to ascertain the adequacy. The bent is supported by seven round Red Oak timber piles. Red Oak is a common wood species used for piles in North America. An exposed pile length of 2,135 mm was assumed for the prototype bridge. It was assumed that the piles were prismatic with a constant diameter of 300 mm. The piles were embedded 305 mm into the pile cap which has out-of-plane width of 760 mm.

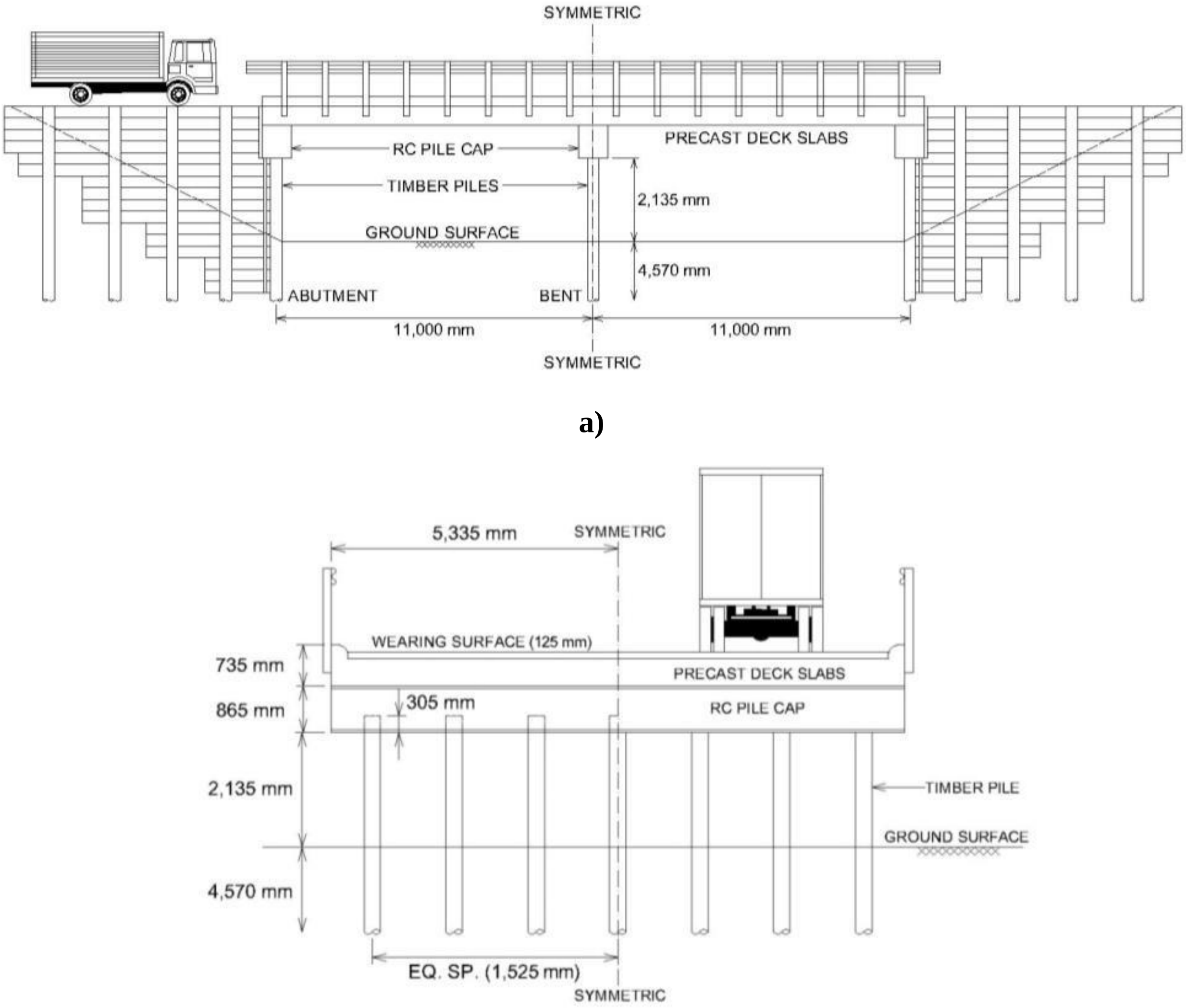

a)

b)

Figure 6.7 Prototype timber pile bridge **a)** Bridge elevation **b)** Bent

6.2.2 Numerical Model

In OpenSees, the timber piles were discretized using beam-column elements with fiber sections and discrete elastic springs were used to represent soil lateral resistance and skin friction. Soil behavior was adopted from geotechnical data obtained by Borello et al. (2010) as part of a forensic investigation carried out on a timber pile bridge. The p-y springs were characterized by a trilinear force-deformation relationship with an ultimate capacity of 55.6 kN while the behavior of the t-z springs varied by depth. This approach is commonly used in modeling bridge foundations and has been shown to yield accurate results in seismic response analyses (Kornkasem et al. 2001). Liquefaction and soil erosion were not considered in this study.

The behavior of the timber pile-to-pile cap joint is characterized by the flexural strength of the timber piles and crushing of timber fibers in the direction perpendicular to grain. Shama & Mander (2004) carried out extensive experimental testing of timber bridge substructure and noted that the joint possesses effective residual rocking capacity even at high levels of drift and after the timber-to-concrete bond breaks down. Based on experimental observations, Shama et al. (2007) derived a simple approach to accurately model the joint behavior. Adopting this approach, a bilinear rotational spring was used to model the timber pile-pile cap joint. The yielding moment, M_y, is given by

$$M_y = 0.415Pd_p \tag{6.1}$$

where P is the gravity load in each pile, and d_p is the pile diameter. A value of 1×10^{-5} rad was assumed for θ_y to capture the high initial stiffness demonstrated by joints and the post-yield stiffness was taken to be 0.3% of the initial stiffness (Shama et al. 2007). Since the main focus of this study is evaluating the performance of the timber piles, it was assumed that the pile cap and superstructure components were not critical. To simplify the model, the deck and RC pile cap were assumed to be rigid, and the deck-to-pile cap connections were not explicitly modeled. It is important to note that failure of bridges due to excessive deck displacement or unseating was frequently observed in past tsunami events (Chock et al. 2013). However, these failure modes were not considered in this study. Mander et al. (2000) showed that the damping ratio of timber piles can range from 3% to approximately 7.5% at high levels of drift, but a constant viscous damping ratio of 5% was assumed throughout the study. This value is in agreement with recommendations in the AASHTO LRFD Bridge Design Specifications (AASHTO 2012).

6.3 TIMBER PILES

6.3.1 Timber Material Behavior

To establish representative material models for this study, specimens were cut from a random selection of field-extracted round Red Oak piles and tested in uniaxial tension and compression. There was no information available on the service duration or site conditions for any of the piles but all specimens were treated with creosote and there were no visible signs of decay or other significant defects. For compressive behavior parallel to the grain, seven specimens were cut from different piles and tested under uniaxial compression. The compression specimens were 610 mm in length and ranged in diameter from 250 mm to 295 mm. For tensile behavior parallel to the grain, ten coupon specimens were fabricated and tested in accordance with ASTM D143-14 (ASTM 2014). At the time of testing, the moisture content of the specimens was between approximately 19% and 21%. The test specimens and results are shown in Figure 6.8.

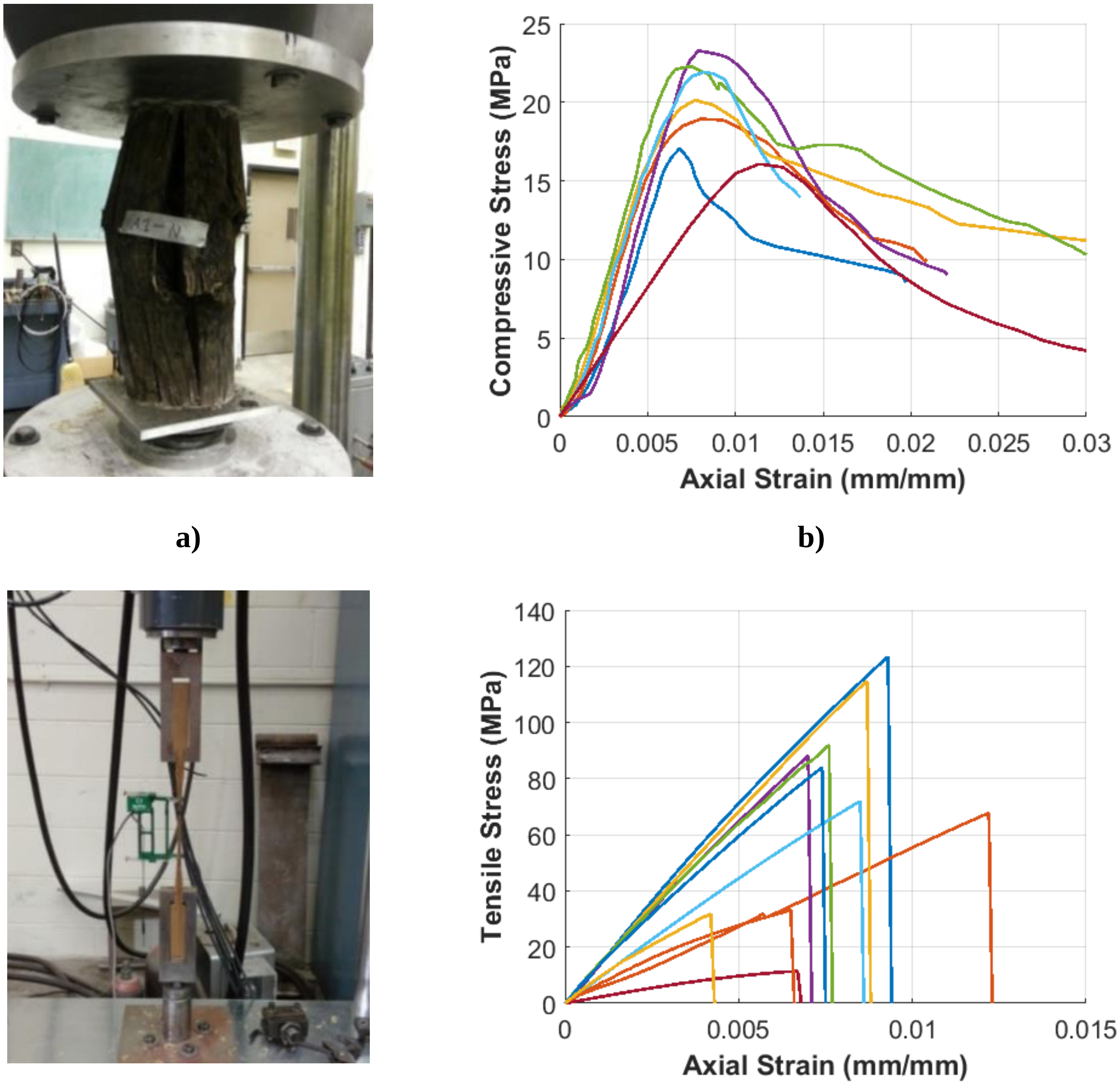

a) b)

c) d)

Figure 6.8 Timber material testing **a)** Compression specimen **b)** Compressive behavior parallel to grain **c)** Tension specimen **d)** Tensile behavior parallel to grain

Overall, the specimens displayed considerable variability in both tension and compression. This is a characteristic of timber as a structural material and primarily attributable to differences in fiber condition. As the plots in Figure 6.8 show, timber behaves in a nonlinear, ductile manner under axial compression, and in a linear, brittle manner in tension. It is worth noting that the compressive strength of the piles was significantly higher than the reference design compressive strength of 7.6 MPa for Red Oak piles provided in the National Design Specification (NDS) for Wood Construction (AFPA 2005). The strength of wood fibers was also significantly greater in tension than in compression. The basic unconfined timber material model used in this study was formulated by averaging the test results shown in Figure 6.8. The average peak stresses in tension and compression were 82.7 MPa and 19.0 MPa, respectively. In tension, the post-peak capacity degrades rapidly enough to capture the brittle nature of tensile failure. The averaged stress-strain curves are shown in Figure 6.9 along with the material model generated in OpenSees using the Concrete07 material, which best replicates the unloading and reloading behavior that was observed.

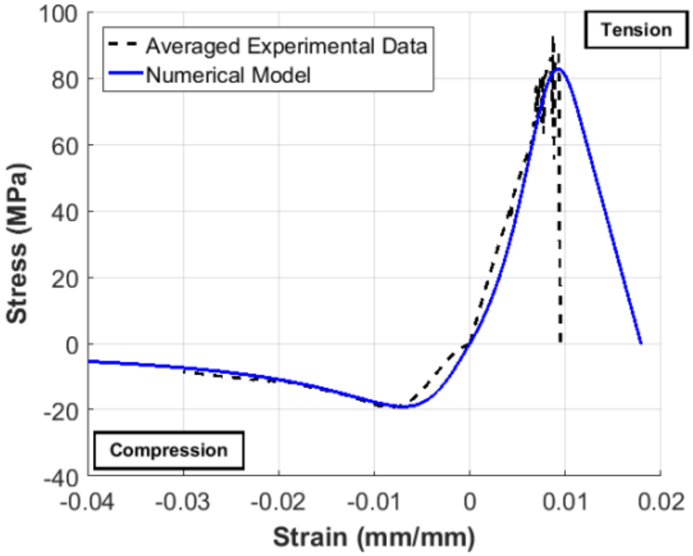

Figure 6.9 Timber material model created in OpenSees

6.3.2 Timber Deterioration

In this study, deterioration was modeled as section loss since section loss represents the ultimate manifestation of deterioration mechanisms such as weathering and decay. Profiles I and III from Chapter 5 (see Figure 5.8) were adopted and it was assumed that the section loss affects the entire exposed length of the pile. In both cases, it was assumed that 25% of the gross cross-sectional area was lost. At 25% section loss, the moment of inertia of section loss Profile III is approximately 50% greater than that of Profile I. The section loss was applied to the entire exposed length of the exterior pile that is farthest downstream from the simulated tsunami. This was identified to be the most critical deterioration case because overturning causes the highest compressive force demands in this pile and despite being ductile in compression, the strength of timber was observed to be considerably higher in tension than in compression. When considering section loss Profile III, the pile was oriented such that the side of the pile with the semicircular void was under compression when tsunami loads are applied. It was also observed in field inspections of various timber pile bridges that exterior piles generally degrade at a faster rate because they are more exposed to weathering mechanisms.

6.3.3 FRP Retrofitting

The effectiveness of using FRP composites to strengthen timber structural components has been demonstrated in numerous studies (Plevris & Triantafillou 1992; Najm et al. 2007; Zhang et al. 2011). In this study, fully confining the timber piles with FRP composites was considered as a retrofitting strategy. Using the GFRP fabric and epoxy resin described in Table 4.2, FRP confinement with a 10 layer composite was adopted. As mentioned previously, Caiza et al. (2012) used similar materials to retrofit eccentrically loaded bridge timber piles and experimentally showed that sufficient load capacity and flexural stiffness could be recovered in damaged timber piles with confinement provided by 8 or 9 layers of GFRP.

Coupon specimens of the 10 layer (6.35 mm thick) GFRP composite demonstrated an average elastic modulus of 14,700 MPa and ultimate tensile strain of 2.2%. GFRP composites behave in a linear elastic manner up to brittle fracture. Similar to the unconfined timber material model discussed above, five 610 mm long timber pile specimens were wrapped with the GFRP composite and tested to establish a material model for the study. The compressive test results are shown in Figure 6.10.

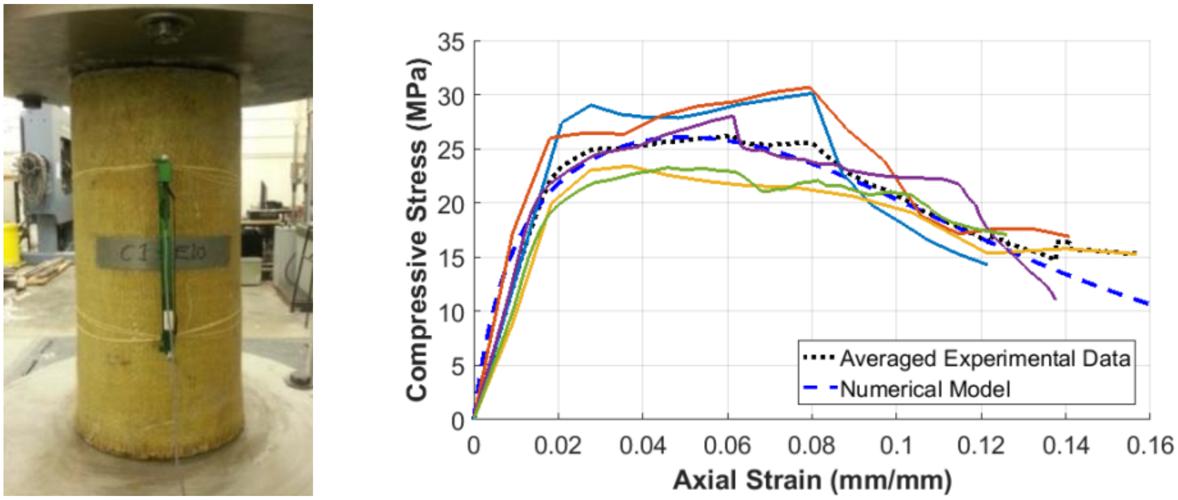

a) b)

Figure 6.10 FRP confined timber pile tests **a)** Test specimen **b)** Compression test results

The overall behavior of FRP confined timber is analogous to that of concrete. It is evident in Figure 6.10 that the FRP confinement provides a substantial improvement in both the peak strength and ductility. Confinement does not affect the tensile strength of the timber itself but the GFRP composite does provide tensile reinforcement in bending. It was assumed that the composite itself has no capacity in compression. As in the unconfined case, the test results were averaged to derive the material model for FRP confined timber. The averaged experimental results and the FRP confined timber material behavior adopted in the numerical model are also shown in Figure 6.10.

Despite the performance improvement the FRP confinement provides, it was observed that retrofitting just the deteriorated timber pile does not provide an appreciable system level improvement. Pushover analysis showed load redistribution influences the structure performance with demands being amplified on the piles immediately adjacent to one affected with section loss. Therefore, it was deemed necessary to also retrofit the sound piles adjacent to the deteriorated pile. The FRP retrofit was applied over the entire exposed length of the timber piles. A schematic of the timber pile bent is shown in Figure 6.11 with the section loss and FRP retrofitting arrangements discussed above.

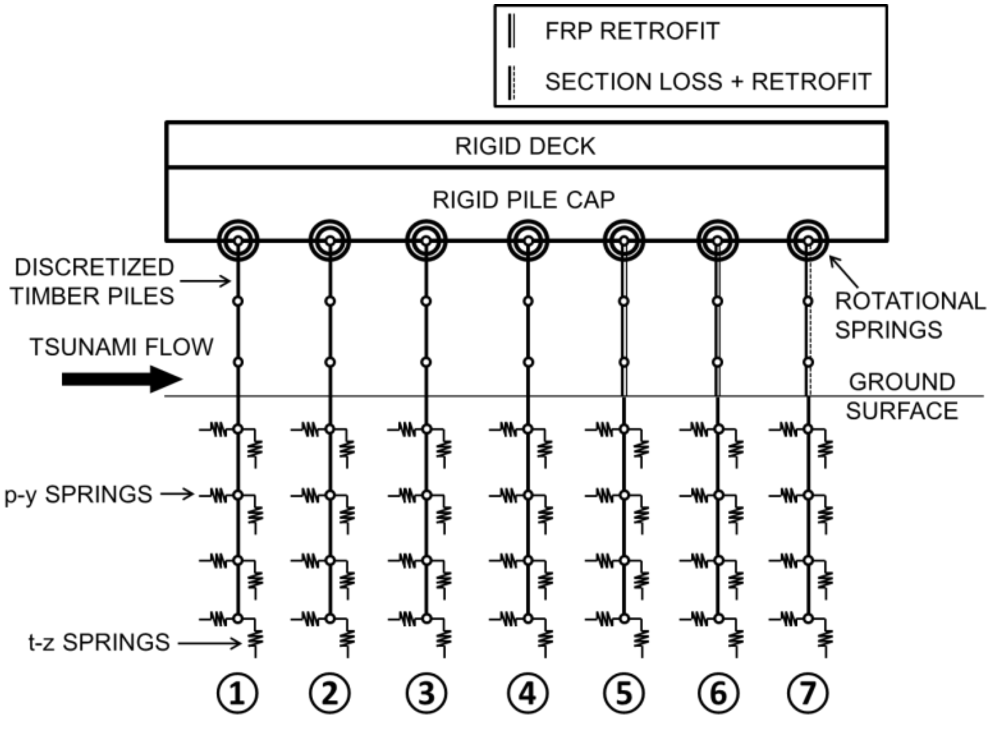

Figure 6.11 Schematic of the timber pile bent model created in OpenSees

With the piles numbered as shown in Figure 6.11, the section loss was assumed to be concentrated in Pile 7 which is the furthest pile downstream in the tsunami simulations. FRP retrofits were applied to Piles 5, 6, and 7. Although the timber pile section loss considered in this study was limited to the exposed regions above the ground surface, decay and fiber deterioration can also occur below grade if piles are exposed to wet-dry cycles. In real life applications, it may be necessary to assess the condition of timber piles below grade and implement strengthening measures.

6.4 MULTI-HAZARD SIMULATION

6.4.1 Limit States

Prior to running full multi-hazard simulations, pushover analyses were conducted to define drift limits that will define failure. In total, there are five different cases of the timber pile bridge model. The pushover curve for each case is presented in Figure 6.12 along with the corresponding fundamental natural periods.

Fundamental Period, T_1 (s)		
No Section Loss		0.783
Profile I	Unretrofitted	0.807
	Retrofitted	0.801
Profile III	Unretrofitted	0.792
	Retrofitted	0.786

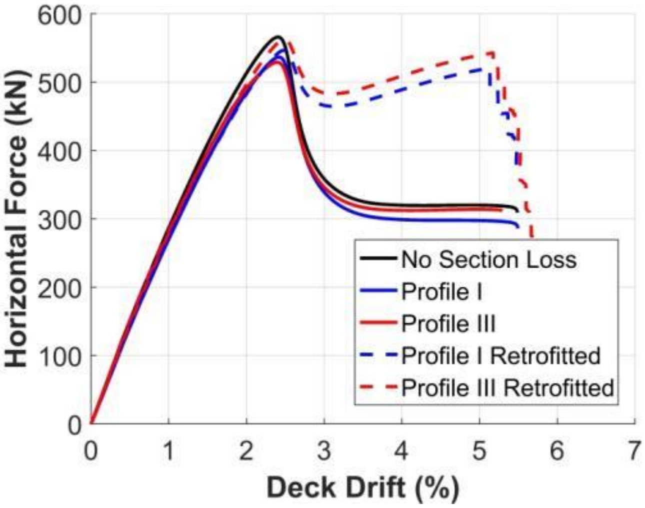

Figure 6.12 Timber pile bent fundamental periods and pushover curves

Without FRP retrofits, section loss clearly reduces the peak strength of the bent but does not affect the drift capacity. Profile I and Profile III led to 5% and 7% reductions in the peak strength respectively. The behavior was largely elastic up to approximately 75% of the peak strength but in the unretrofitted cases, there is also a significant post-peak softening behavior that coincides with yielding and rupturing of wood fibers. The overall timber pile behavior is consistent with experimental results in Allicock (1999) and Shama et al. (2007). Although the unretrofitted bent does demonstrate noticeable post-peak residual capacity, the structure was determined to be inadequate at this point as the loss of capacity exceeds 40% of the peak strength. Therefore, a drift limit of 2.4% was imposed on the unretrofitted timber pile bridge with and without section loss. This corresponds to the drift level at peak strength.

When FRP retrofits are applied there is a significant improvement in the residual strength. The post-peak softening is much less severe and as the load redistributes to the FRP retrofitted piles, the bent displays a stiffening behavior. The initial post-peak decline in the capacity is less than 15% of the peak strength and the FRP retrofitting provides additional ductility capacity. For the FRP retrofitted case with either section loss profile, the ultimate drift was more than doubled to 5% compared to the unretrofitted case. It is also shown that section loss Profile III yielded a peak strength that is 3% higher than that from section loss Profile I. In the simulations performed in this study, the bridge was considered to have failed if the deck drift ratio exceeded 2.4% with unretrofitted piles, and 5% with FRP retrofitted piles.

6.4.2 Earthquake Records

The risk of earthquake events along the Pacific Coast of the United States is relatively well documented and understood. Although tsunamis have historically been associated with subduction zone earthquakes, the possibility of shallow crustal earthquakes generating localized tsunamis cannot be discounted. In particular, the Seattle Fault Zone and other active faults in Western Washington are known to have the potential to generate tsunamis (Koshimura & Mofjeld 2001; Geist et al. 2006). In this study, six shallow crustal earthquake ground motions and three subduction zone earthquake ground motions were considered as part of the earthquake-tsunami scenario. The subduction zone ground motions were from the 2011 Tohoku Earthquake which generated the now infamous tsunami. The goal was to generate a suite with a wide variation in characteristics. The records were not scaled based on a specific site or design spectrum. The ground motion records used in this study are listed in Table 6.1.

Table 6.1 Earthquake ground motions used in the multi-hazard simulations

	Earthquake	Station	Predominant Period (sec)	Significant Duration, $D_{5\text{-}95}$ (sec)	PGA (g)
Shallow Crustal Earthquakes	Coalinga (1983)	Parkfield – Fault Zone 4	0.66	17.35	0.172
	Loma Prieta (1989)	Richmond City Hall	0.88	11.835	0.123
	Northridge (1994)	LA – Pico & Sentous	0.20	20.17	0.108
	Kobe (1995)	Yae	0.84	36.03	0.152
	Chi-Chi (1999)	CHY039	0.72	37.47	0.106
	Hector Mine (1999)	Joshua Tree	0.36	13.95	0.183
Subduction Zone Earthquakes	Tohoku (2011)	FKSH14 Iwaki – E	0.20	72.21	0.121
	Tohoku (2011)	IWTH14 Taro	0.54	103.61	0.040
	Tohoku (2011)	MYGH12 Shizugawa	0.14	83.81	0.253

The ground motion records were filtered using a fourth order Butterworth filter and truncated down to the significant duration yielding between 5% and 95% of the Arias Intensity. It is generally known that subduction zone earthquakes have longer durations and release more energy compared to shallow crustal earthquakes. It should be noted that the size of the tsunamis generated in this study were not correlated to the earthquake ground motions in any way. As discussed below, the size of the tsunami was increased incrementally to determine the intensity at which the bridge failed after being subjected to each ground motion.

6.4.3 Tsunami Simulation

The tsunami simulation in this study was performed using the Particle Finite Element Method (PFEM). The accuracy and efficiency of PFEM in solving FSI problems has been demonstrated in several studies (Oñate et al. 2004; Idelsohn et al. 2006). Recently, the OpenSees framework was expanded to include PFEM analysis capabilities by Zhu & Scott (2014). This not only allows the flexibility to use existing OpenSees commands and material models but also enables a seamless transition which captures damage accumulation between the earthquake and tsunami hazards.

The mechanics for tsunami generation are relatively well understood and researchers have studied the relationship between seismic activities and tsunamis (Geist 1998; Satake & Tanioka 1999). However, accurately modeling tsunami run-up and propagation onshore is still a challenge. Tsunami waves generally tend to break offshore and approach the shore as a hydraulic bore (FEMA 2012). Experimental and numerical studies in the literature have reproduced the tsunami bores as dam-break flows with good results (Yeh 1991; Chanson 2006; Arnason et al.

2009; Nistor et al. 2011). In this study, the tsunami was represented as an idealized bore. The tsunami simulation setup is shown in Figure 6.13.

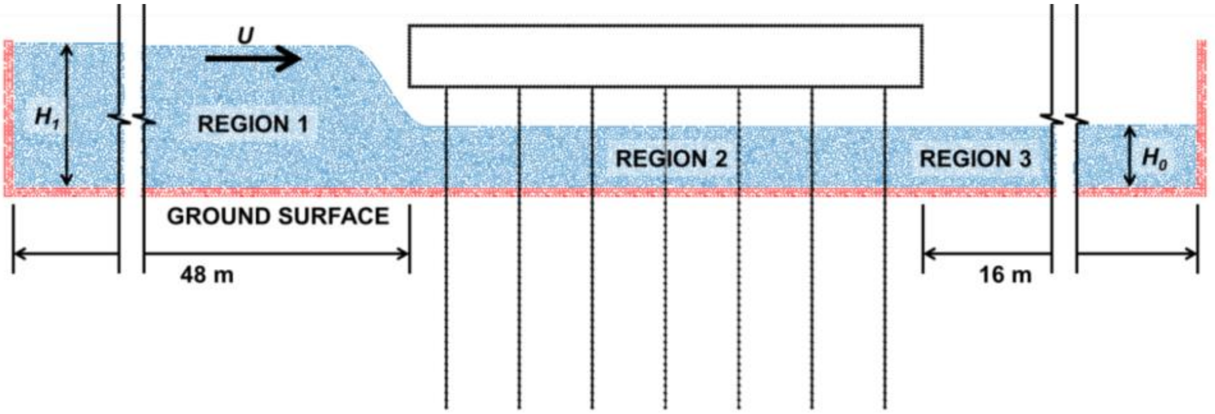

Figure 6.13 Idealized bore used to simulate tsunami loading

The tsunami bore is defined by three distinct regions. Region 1 is the bore with height H_1 moving at a prescribed velocity, U, Region 3 represents stagnant flooding downstream, and Region 2 is a transition region with a linear velocity gradient. The tsunami simulation is confined by impermeable, fixed boundaries which precludes fluid-soil interactions. As indicated in Figure 6.13, the simulation domain was 48 m long on the tsunami side and 16 m long at the downstream end. These dimensions were adequate to generate sufficiently large tsunami bores throughout the study and ensure waves reflecting off the fixed boundary at the downstream end did not interfere with the tsunami impact.

The velocity, U, is related to the downstream inundation depth, H_0, through the Froude number, F_r.

$$F_r = \frac{U}{\sqrt{gH_0}} \tag{6.2}$$

where g is the gravitational acceleration constant. A constant F_r of 1.43, and H_1/H_0 ratio of 2.3 were adopted to generate fully developed tsunami bores with constant initial energy (Carey et al. 2014).

The fluid domain was discretized into a 75 mm × 75 mm mesh. The fluid was assumed to be incompressible and inviscid. Given the fact that the timber piles represent an insignificant contact area compared to the longitudinal dimension of the bridge, the interaction between the tsunami and timber piles was neglected. Therefore, the tsunami simulation only involves interactions between the tsunami and the bridge superstructure. In addition to this simplification, the three-dimensionality of the model was resolved into two dimensions by scaling the fluid density by the out-of-plane tributary span length of 11 m. This effectively scales the hydrodynamic forces. However, it should be noted that this dimensional simplification may not be adequate in cases where three-dimensional effects are important. The tsunami simulations in this study were typically less than two seconds long. Snapshots from a sample tsunami simulation are shown in Figure 6.14.

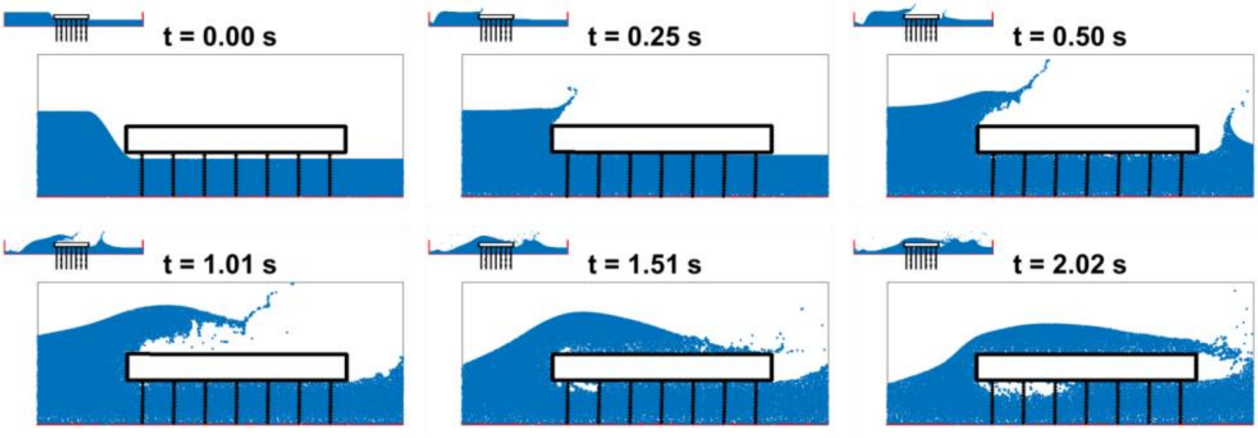

Figure 6.14 Tsunami simulation captured at various time points

In this study, the multi-hazard simulations were performed using an incremental sequential approach similar to the approach used by Carey et al. (2014). The timber deterioration hazard is introduced in the initial model definition. The earthquake intensity was linearly scaled based on the spectral acceleration at the structure fundamental period and for each case a series of tsunami simulations were carried out to determine the tsunami intensity that results in failure.

6.5 ANALYSIS RESULTS

6.5.1 Multi-Hazard Interaction

Results of simulations performed in this study are presented in Figure 6.15 in the form of multi-hazard interaction diagrams. A total of 351 earthquake-tsunami scenarios were involved. The interaction diagrams provide an overview of damage accumulation across hazards and express the capacity of a structure in terms of hazard intensities. The earthquake and tsunami hazards are described using the spectral acceleration at the bridge fundamental period and momentum flux, respectively. Momentum flux is defined as the rate of transfer of momentum over a unit area and is a direct measure of the force that a fluid flow can impart on a body (Yeh 2006). As discussed above, the limit states for the timber pile bridge were defined in terms of the deck drift ratio (2.4% with no retrofits and 5% with FRP retrofits). Figure 6.15 a) shows the results for the bridge without timber deterioration, each curve representing a different earthquake. The bridge models with pile section loss are featured in Figures 6.15 b) and c) with solid and dashed curves signifying the cases with and without FRP retrofitting, respectively.

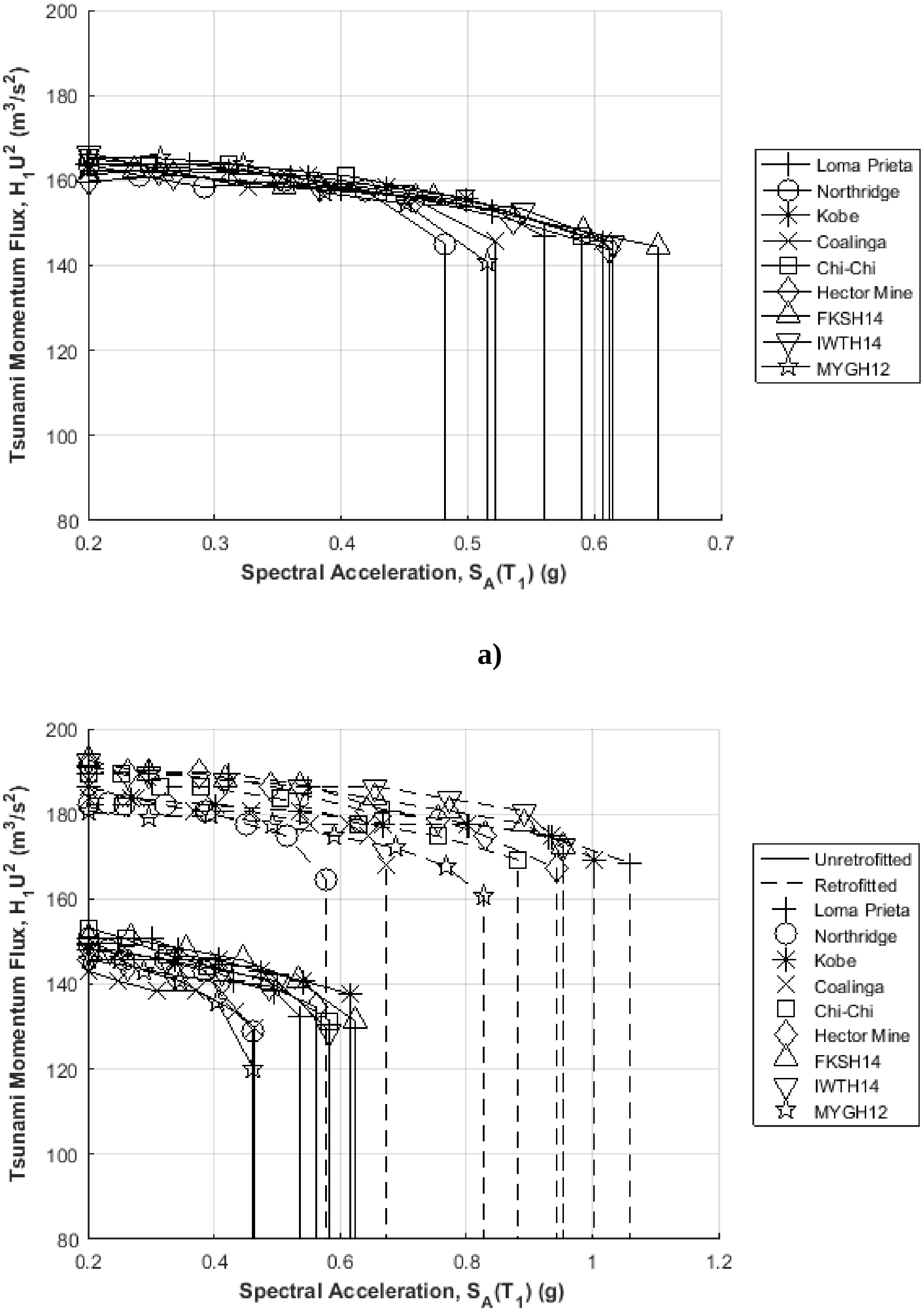

a)

b)

Figure 6.15 Multi-hazard interaction diagrams **a)** Bridge with no timber pile deterioration **b)** Bridge with pile section loss (Profile I) **c)** Bridge with pile section loss (Profile III) **d)** Typical behavior

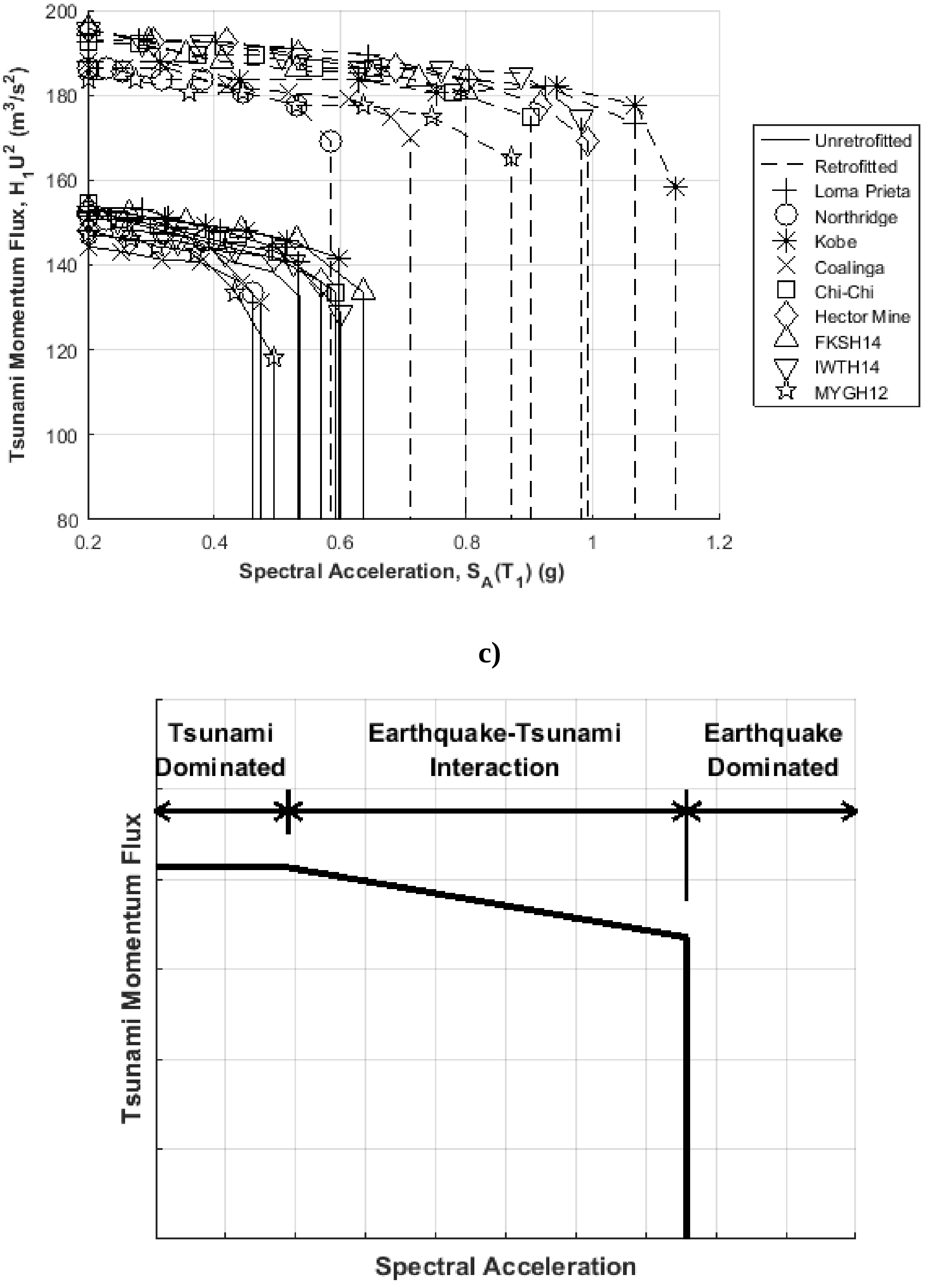

c)

d)

Figure 6.15 (cont.)

The combined action of the deterioration-earthquake-tsunami hazards is complex but some general tendencies can be observed. First and foremost, the limit state curves defined in each interaction diagram can be divided into three distinct regions as shown in Figure 6.15 d). Tsunami dominated failure occurs at low earthquake spectral accelerations and is characterized by a relatively constant level of tsunami momentum flux. In these cases, the earthquake ground motion imparts little to no damage in the timber piles and failure is predominantly the result of the tsunami loading. On the other hand, the abrupt drop to zero tsunami momentum flux at high spectral accelerations indicates earthquake dominated response where the ground motion induces complete failure of the bridge without tsunami loading. The interaction of the sequential earthquake-tsunami hazard is captured between the tsunami dominated and earthquake dominated regions. In the case of the unretrofitted timber pile bridge, the earthquake-tsunami interaction region typically occurs between $S_A(T_1) =$0.30g and $S_A(T_1) =$0.50g. In comparison, the tsunami dominated region becomes extended when FRP retrofits are applied. This is understandable since the additional strength and ductility provided by the FRP retrofit means the timber piles can sustain greater damage during the earthquake but still retain significant load carrying capacity for the tsunami loading.

To illustrate the difference between tsunami dominated behavior and failure due to earthquake-tsunami interaction, the response time histories from two cases plotted in Figure 6.15 b) were compared. The timber pile bridge with section loss Profile I was subjected to the Hector Mine earthquake ground motion at $S_A(T_1) =$0.27g, and $S_A(T_1) =$0.54g. In both cases, the bridge was then struck by a tsunami bore with a linear momentum flux of 135 m^3/s^2. The response is plotted in Figure 6.16.

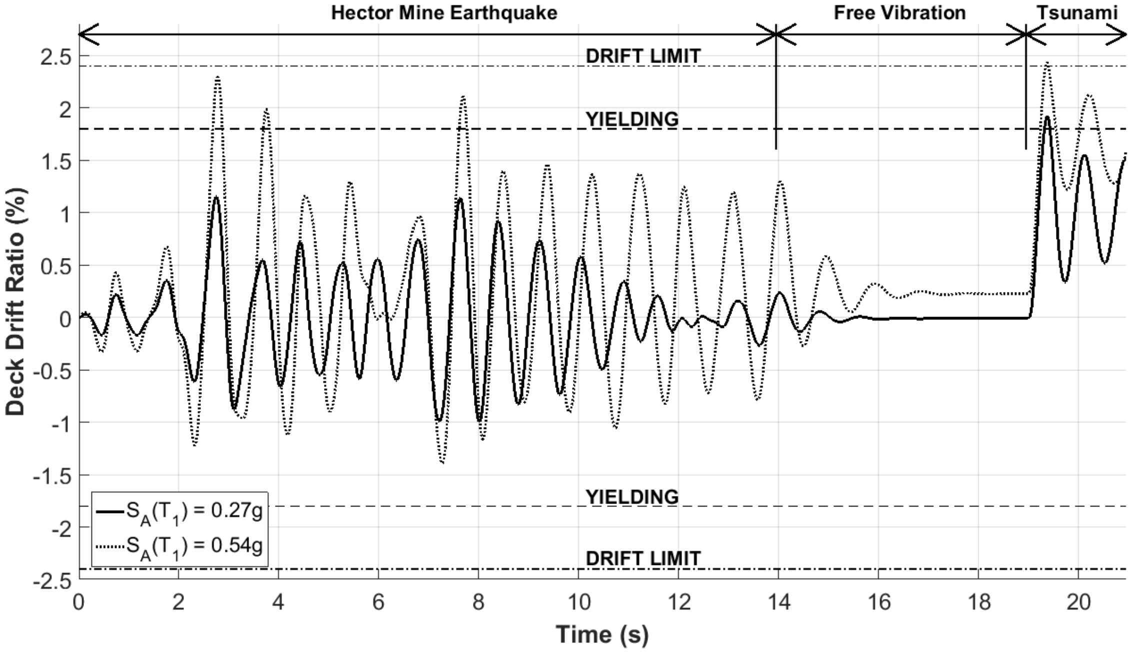

Figure 6.16 Earthquake-tsunami response time history demonstrating tsunami dominated behavior ($\boldsymbol{S_A(T_1)} = 0.27$g) and earthquake-tsunami interaction ($\boldsymbol{S_A(T_1)} = 0.54$g)

The yielding drift ratio indicated in Figure 6.16 corresponds to the drift at which inelastic deformation first occurs in the timber piles. The earthquake ground motion with spectral acceleration at 0.54g caused plastic deformation in the timber piles but the maximum drift did not reach the failure drift limit of 2.4%. The bridge failed in the subsequent tsunami bore impact. With $S_A(T_1)$ =0.27g, the timber piles remained in the elastic regime and the maximum deck drift ratio in the tsunami simulation was approximately 1.9%, indicating the bridge still possessed enough reserve capacity to withstand the given tsunami. The key difference between the two cases is the damage sustained by the timber pile bent in the earthquake simulation which can be characterized by residual deformation and period elongation. For $S_A(T_1)$ =0.27g there is almost no residual deformation and the bridge fundamental period remained virtually unchanged. With $S_A(T_1)$ =0.54g, the residual deformation is more significant at 0.23% and the period is elongated to 0.921 seconds (a 14% increase), indicative of the timber piles losing stiffness. It is clear that increased earthquake damage leads to a diminished reserve load capacity for the subsequent tsunami loading.

Overall, the characteristic differences between the shallow crustal earthquakes and subduction zone earthquakes are not distinguishable in the earthquake-tsunami interaction diagrams. In the case of the bridge with no pile section loss shown in Figure 6.16 a), the average difference in the tsunami intensity at the lowest and highest earthquake intensities is approximately 10%.

When timber pile deterioration is included, the impact of the earthquake-tsunami hazards are amplified as the overall load capacity of the bridge is reduced. On average, the maximum tsunami momentum flux observed in the case with section loss Profile I was 11% lower than the case without any section loss. Given the fact that the 25% section loss modeled in this study represents a modest level of deterioration and is only affecting a single pile, this represents a considerable reduction. Although the peak capacity of the bridge affected with section loss Profile III was marginally lower than that with Profile I in the pushover analysis, the performance of the bridge affected with Profile III was comparable to that with Profile I.

As shown in Figures 6.15 b) and c) the FRP retrofitting greatly improves the performance of the bridge. Compared to the prototype bridge model with no timber deterioration, the maximum tsunami momentum flux of the deteriorated bridge with FRP retrofits is at least 15% higher and the maximum spectral acceleration defining earthquake dominated behavior is also improved by up to 80%. Compared to the cases without FRP retrofits, the general behavior of the retrofitted bridge is more tsunami dominated. This tendency can be attributed to the additional strength and ductility provided by the FRP confinement. It is also evident that in the retrofitted cases, the bridge with section loss Profile III generally failed at slightly higher earthquake and tsunami intensities.

6.5.2 Discussion on Tsunami Hazards

To better understand the impact of tsunami on the timber pile bridge, the hydrodynamic force time histories from an idealized bore with an initial velocity of 5.08 m/s are shown in Figure 6.17. The magnitude and duration of the forces depend on the height and velocity of the tsunami. It is clear from Figure 6.17 that the maximum horizontal and vertical forces do not necessarily occur at the same time. In the horizontal direction, the initial impact of the tsunami causes a high impulsive force which is followed by a steady-state load as the tsunami bore continues to flow at a relatively constant velocity. It was observed that the magnitude of vertical forces on the bridge deck is typically more than 10 times greater than that in the horizontal direction. Given the high tensile strength of timber fibers, the hydrodynamic uplift forces do not lead to significant damage in the timber piles. However, it could have a more significant impact on other bridge components such as bearings and connections. As mentioned above, excessive deck displacement or unseating were frequently observed in past tsunami events. However, this study focused on the performance of the substructure and other failure modes were beyond the scope of this study.

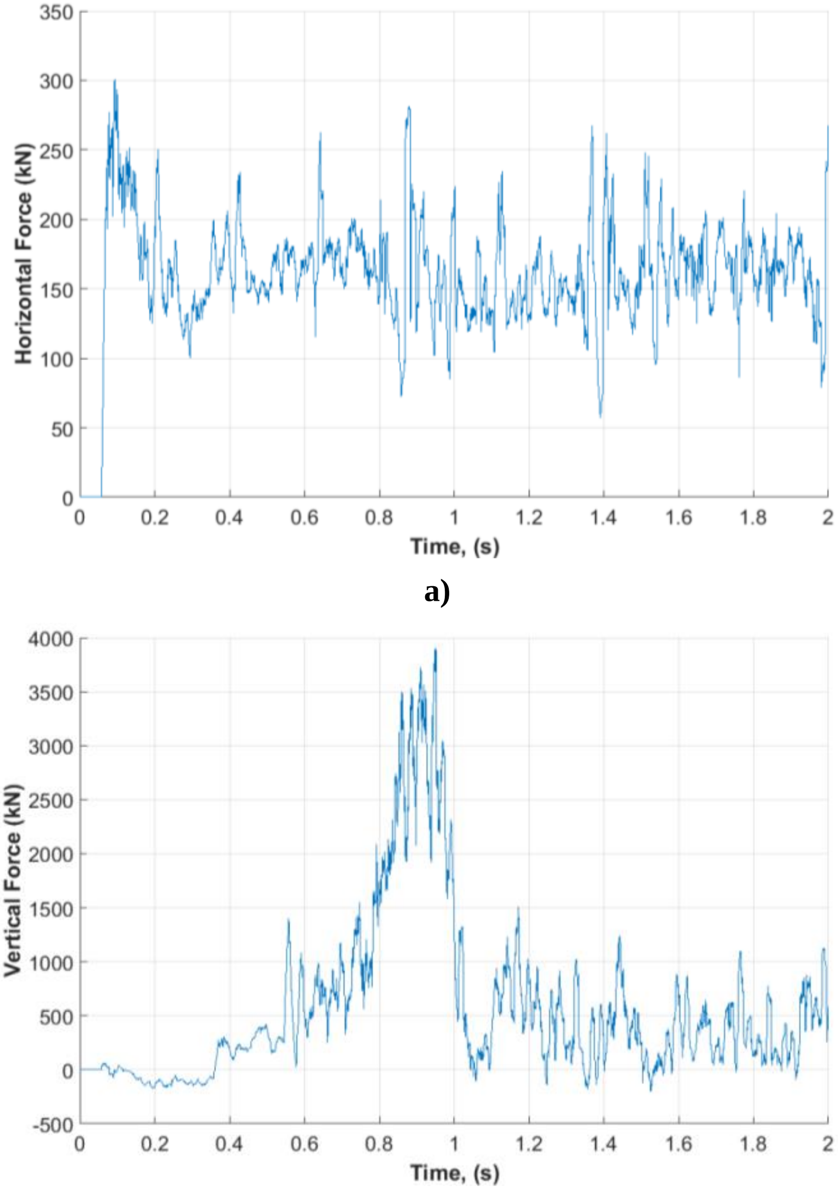

a)

b)

Figure 6.17 Typical tsunami force time histories **a)** Horizontal force **b)** Vertical force

To put the impact of the tsunami into perspective, it is instructive to consider the tsunami hazard in isolation. Although there is no direct information in the literature related to the performance of timber pile bridges in tsunami events, insight can be gained from data available on past tsunamis. In particular, video footages and post-disaster field surveys from the 2011

Tohoku Tsunami have allowed experts to estimate the flow depth and velocity of the tsunami (Fritz et al. 2012; Chock et al. 2013). Analysis by Fritz et al. (2012) found that tsunami heights reached 9 m in Kesennuma Bay, Japan with a maximum flow velocity of up to 11 m/s. Based on the estimated tsunami time history established by Fritz et al., it is possible that the maximum momentum flux of the tsunami current observed in Kesennuma Bay could have exceeded 180 m^3/s^2, in which case the prototype timber pile bridge with no FRP retrofits would have failed with certainty. Tsunami velocity estimates by Chock et al. (2013) vary from approximately 1.36 m/s up to 13.4 m/s depending on the site. Based on the tsunami bore construction used in this study, the maximum tsunami velocity that could be resisted by the timber pile bridge with no section loss ranged between 5.9 m/s and 6.2 m/s. Both the tsunami velocity and height depend greatly on site conditions and it is important to highlight that maximum tsunami height and maximum velocity do not necessarily occur simultaneously. However, both are important factors to consider in evaluating structural performance.

6.6 SUMMARY OF CHAPTER 6

This study examined the performance of a timber pile bridge subjected to a multi-hazard scenario involving timber deterioration, earthquake, and tsunami loads. The study also considered a retrofitting strategy using FRP composites. The main outcomes from the analyses are summarized below.

- The earthquake-tsunami response could be categorized into three regions: tsunami dominated, earthquake dominated, and earthquake-tsunami interaction depending on the damage sustained during the earthquake ground motion. For the prototype bridge model and ground motions considered in this study, results showed that earthquake-tsunami interaction generally occurred between $S_A(T_1) =$0.30g and $S_A(T_1) =$0.50g.

- Improved ductility provided by the FRP retrofitting allowed the timber piles to retain significant load carrying capacity even with earthquake damage. As a result, tsunami dominated failure was more prevalent when FRP retrofits were applied.
- For the bridge model without section loss, increasing the earthquake intensity reduced the tsunami momentum flux at failure by more than 10% between the tsunami dominated and earthquake dominated cases. Differences of up to 20% were observed in cases with timber pile section loss.
- The simulations conducted in this study showed that the prototype timber pile bridge with no section loss failed at tsunami velocities ranging between 5.9 m/s and 6.2 m/s.
- The FRP retrofitting strategy used in this study increased the maximum tsunami momentum flux by more than 15% and the maximum earthquake intensity by up to 80% compared to the prototype bridge with no timber pile section loss.

CHAPTER 7

EVALUATION OF DAMAGE IN TIMBER PILE BRIDGES SUBJECTED TO EARTHQUAKE-TSUNAMI SCENARIOS

The devastation caused by tsunamis in Sumatra (2004), Chile (2010), and Japan (2011) clearly showed the need to assess the risk of tsunamis in earthquake-prone regions and has led to the development of tsunami hazard design guidelines such as FEMA P-646 (FEMA 2012) and the new chapter on tsunami hazards in ASCE 7-16 (ASCE/SEI 2017). Although most structures in high seismic regions are designed to withstand significant earthquake loads, the provisions may not be adequate for an ensuing tsunami should such an event occur. In the case of older, existing structures designed using obsolete seismic design provisions or, as in the case of timber pile bridges, no seismic provisions at all, this is a critical problem. Furthermore, these guidelines provide design earthquake and tsunami loads independently of each other and are not clear on their combined effects. The sequential nature of an earthquake-tsunami event means that there will be carryover and interaction of damage between the two hazards. Therefore, in an earthquake-tsunami event, structures must possess adequate post-earthquake capacity to withstand the subsequent tsunami load effects (FEMA 2012). Loss of strength is a crucial factor to consider especially in timber structures as timber generally has lower strength and ductility capacity compared to steel or reinforced concrete and degradation can occur rapidly.

The main focus of this study is to present a method to capture the effect of earthquake damage on timber piles and how it influences the post-earthquake tsunami response. Timber pile bent models were subjected to simplified, predetermined earthquake-tsunami hazard demands and detailed simulations in which the tsunami was modeled using PFEM. The findings from this study can be useful to engineers in assessing the risk of existing timber pile bridges in sequential earthquake-tsunami scenarios and help them be proactive in making retrofit decisions as well as planning evacuation routes.

7.1 TIMBER PILE BRIDGES

7.1.1 Description

Three different timber pile bent designs were considered in this study. Unlike the unbraced prototype bent considered in Chapter 6, the simulations conducted in this study included two bracing configurations. Similar to the prototype bridge, as-built drawings were consulted to establish constants and variables in the design. The basic timber pile bent models are illustrated in Figure 7.1.

Although Figure 7.1 shows bents supported on seven piles, the number of piles varied between five, six, and seven. However, pile spacing, minimum penetration depth, pile cap dimensions, and bracing designs were generally consistent throughout. These typical details are indicated in Figure 7.1. The bracing system typically consisted of 76 mm × 254 mm lumber connected to the timber piles using 19 mm diameter bolts. The remaining dimensions including deck height (H), exposed pile length (L), span length, pile diameter, as well as material strengths for the timber piles and bracing members were treated as random variables as discussed below.

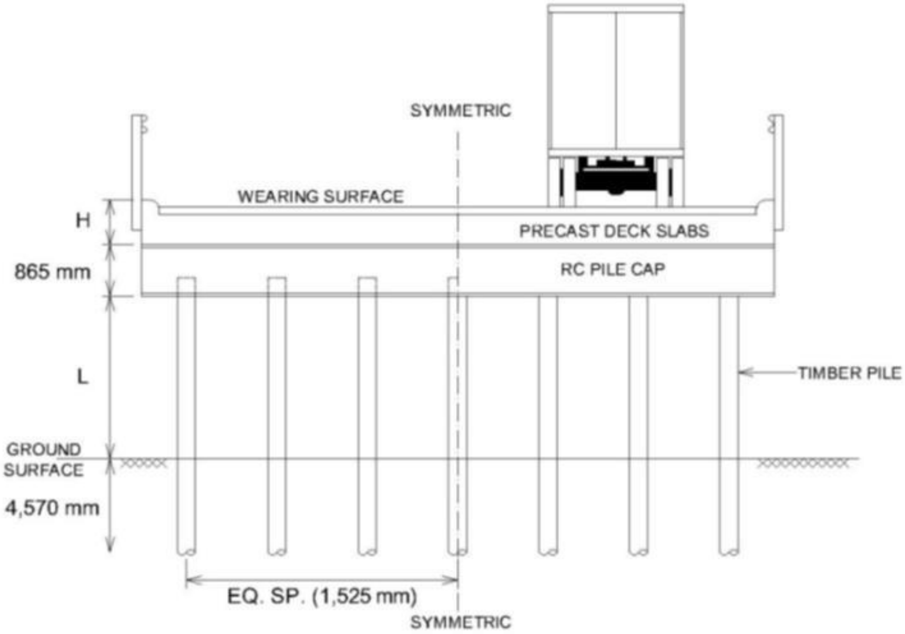

a)

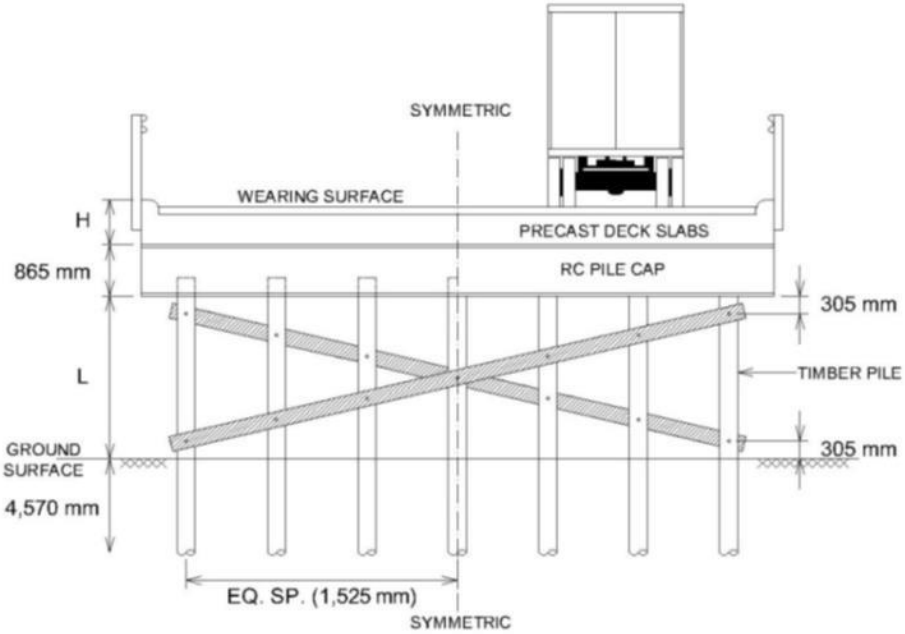

b)

Figure 7.1 Typical timber pile bents with **a)** No bracing **b)** Single cross bracing **c)** Double cross bracing

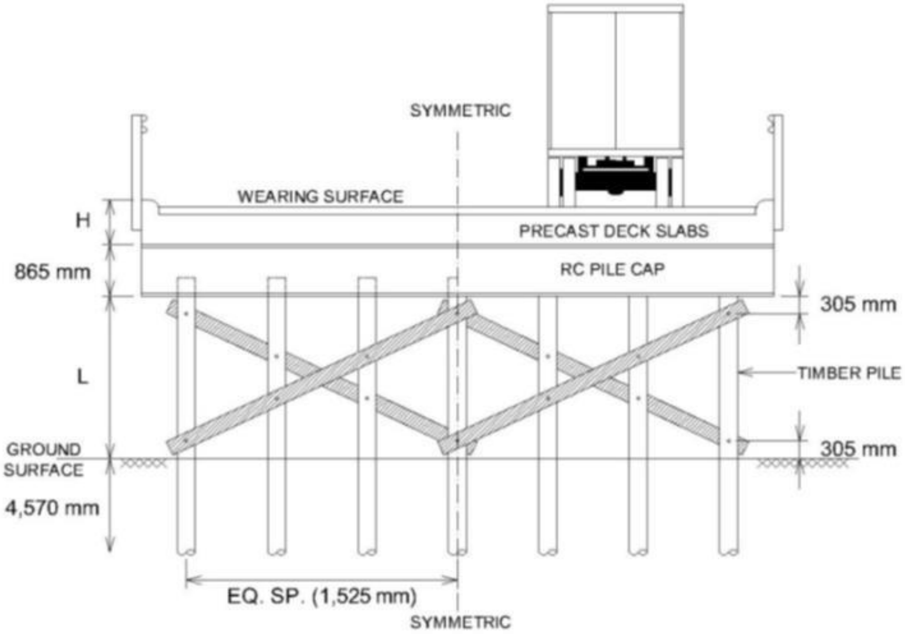

c)

Figure 7.1 (cont.)

7.1.2 Numerical Model

The unbraced timber pile bent model developed in Chapter 6 (see Figure 6.5) provided the basis for the numerical models in this study. Similar to Chapter 6, the bents were modeled and analyzed using the OpenSees framework (McKenna et al. 2000). The main differences between the current study and the model considered in Chapter 6 are the introduction of timber bracing elements, and that that the number of piles is a parameter in this study. The cross bracing in this study were modeled using the method developed by Shama & Mander (2003) which combines the behavior of the brace and the bracing-to-pile connection. Truss elements were used to represent the braces in OpenSees. As noted above, it was assumed that the brace and connector sizes were constant across all models and that the bracing was installed 305 mm from the pile cap and 305 mm from the ground surface (see Figure 7.1). A trilinear force-displacement relationship with gap and slack properties defines the bracing elements. The model defined by Shama & Mander (2003) is shown in Figure 7.2.

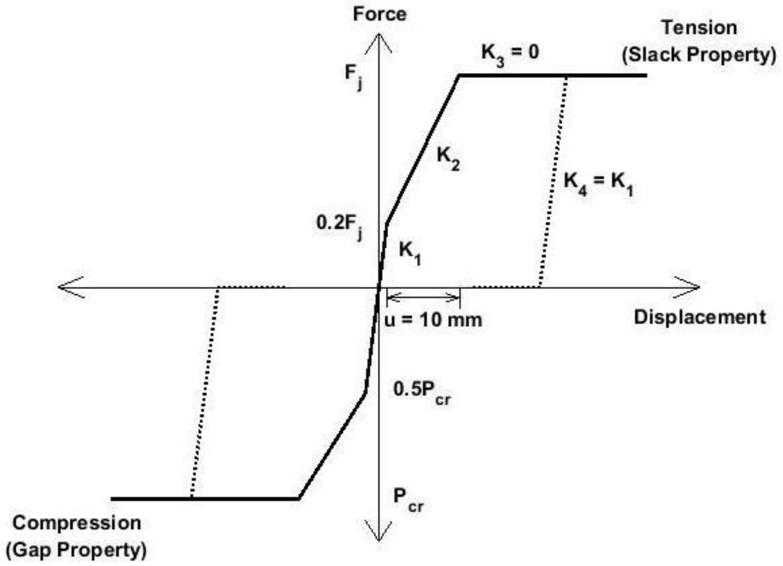

Figure 7.2 Timber cross bracing force-deformation relationship (Shama & Mander 2003)

The tensile strength (F_j) of the bracing system is governed by the connection bearing on the pile while the compressive strength is given as the out-of-plane Euler buckling load (P_{cr}). F_j was computed as:

$$F_j = d_b t f_c \tag{7.1}$$

Where d_b is the diameter of the connector, t is the thickness of the brace, and f_c is the compressive strength of the timber brace. K_1 and K_2 were calculated as:

$$K_1 = \frac{Etd_p}{L_b} \tag{7.2}$$

$$\underset{\text{(Tension)}}{K_2 = \frac{0.8F_j}{u}} \qquad \underset{\text{(Compression)}}{K_2 = \frac{0.5P_{cr}}{u}} \tag{7.3}$$

Where, E is the elastic modulus of the timber brace, L_b is the buckling length of the brace, and u is the slotting displacement equal to 10 mm the exceedance of which causes the bracing to behave in a perfectly plastic manner (Shama et al. 2007). As was the case in Chapter 6, the pile cap and superstructure were assumed to be rigid to simplify the model. A schematic of the timber pile bent models created in OpenSees is shown in Figure 7.3. Neither liquefaction nor scour effects were considered in the analyses.

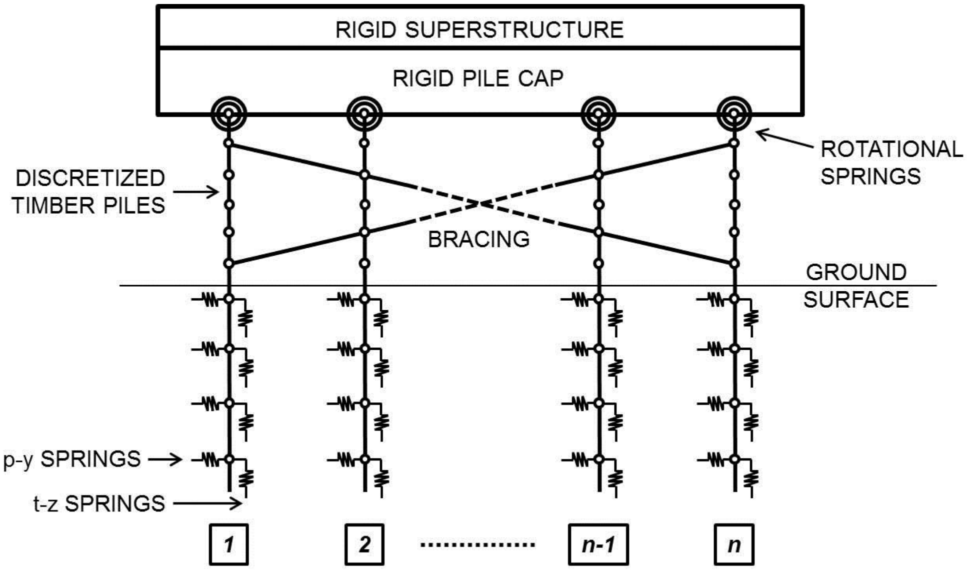

Figure 7.3 Schematic of a timber pile bent numerical model

As discussed above, the number of piles was varied between five, six, and seven. Timber is an anisotropic material with behavior dependent on species and environmental factors.

Naturally occurring defects such as knots and degradation problems such as decay can also significantly affect the strength of timber. Inconsistencies in material behavior and member size can also be a source of uncertainty in timber structures (Mansour 1990; Brites et al. 2013). The material models were developed based on the test results shown in Figure 6.2. The Concrete04 material model in OpenSees was used to replicate the behavior of the timber pile material. Overall, the Concrete04 model is almost identical to the Concrete07 model used in Chapter 6 but was found to be significantly more computationally efficient. Given the large number of simulations required in this study, minimizing computational time was essential. An example of the Concrete04 material behavior is shown in Figure 7.4.

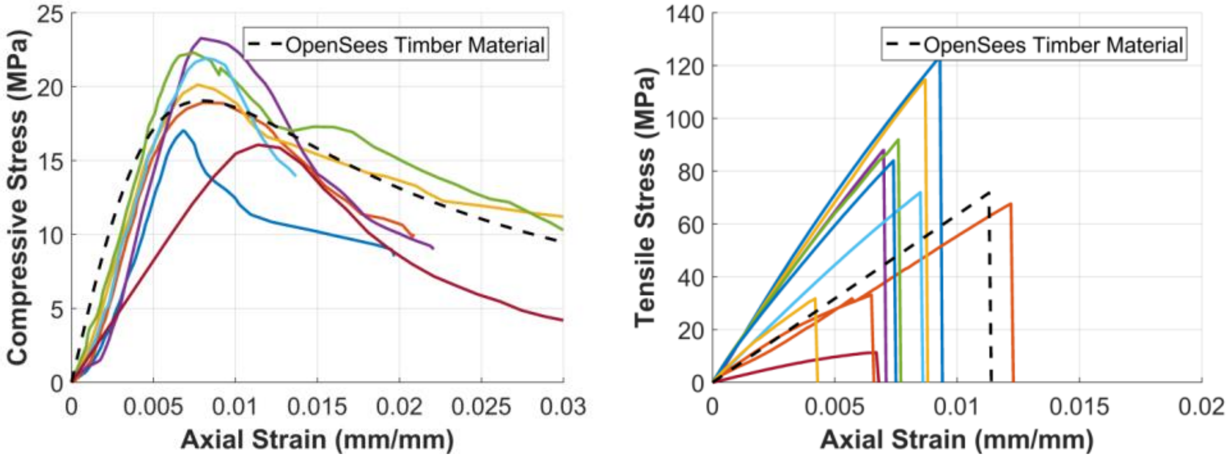

a) **b)**

Figure 7.4 Timber pile material test results and Concrete04 material model used in OpenSees for a) Uniaxial compression, and b) Uniaxial tension

Lastly, Mander et al. (2000) showed that timber piles have high deformation capacity and estimated equivalent viscous damping ratios can reach up to 9% at high levels of drift for timber in good condition and 6% in deteriorated timber. In this study, the AASHTO recommended equivalent viscous damping ratio of 5% for timber structures was adopted in all simulations (AASHTO 2012).

7.2 MONTE CARLO SIMULATION

7.2.1 Sampling

As introduced above, the general layout of typical timber pile bridges does not vary greatly. However, no two bridges can be expected to be identical in geometry. Furthermore, the size and mechanical properties of timber piles are highly variable, not to mention the possibility of deterioration issues such as decay. Therefore, deterministic analysis of timber bridge components is problematic (Bahkt 1983; Mansour 1990). Various researchers have investigated the probabilistic treatment of timber structures (Köhler et al. 2007; Brites et al. 2013). In this study, Monte Carlo simulation was used to relate timber pile bridge response bridge geometry and timber strength. Monte Carlo simulations are often used to determine the probability of failure of a system by evaluating its performance for randomly sampled input parameters (Ang & Tang 2007).

For the simulations in this study, bent models were grouped by the number of piles and bracing configuration. 500 random samples were then generated within each group with random superstructure height, span length, and pile length. Each pile in the model was assigned a distinct diameter and strength. In bents with braced piles, the strength of each timber brace was also treated as a random variable. For each random variable Latin hypercube sampling (LHS) was used to generate the samples. LHS is a stratified sampling scheme in which the range of each variable is first divided into N equally probable intervals and a random value is chosen from each interval based on the prescribed probability density. LHS is commonly used in Monte Carlo simulations to ensure that each variable is fully sampled over the possible range and reduce the sample size (McKay et al. 1979; Kong et al. 2013).

As mentioned above, factors that were kept constant across all models were the pile penetration depth (4,57 mm), soil behavior, pile spacing (1,525 mm), pile cap cross-sectional dimensions (865 mm × 762 mm), and bracing member size (76 mm × 254 mm). All parameters used to define the timber pile bent models, both constant and random, are summarized in Table 7.1. For geometric variables, the range of possible values was obtained from as-built drawings of existing timber pile bridges. Timber strengths were determined experimentally as discussed above.

Table 7.1 Parameters used to define timber pile bent models

Parameter		**Distribution**
Embedded Pile Length	4.57 m	Constant
Pile Spacing	1.52 m	Constant
Pile Cap Cross-Sectional Area	865 mm × 762 mm	Constant
Bracing Cross-Sectional Area	76 mm × 154 mm	Constant
Pile Length Above Ground Surface, *L*	Range: 1.5 m – 2.7 m	Uniform
Superstructure Height, *H*	Range: 0.7 m – 1.1 m	Uniform
Span Length, *B*	Range: 7.6 m – 10.7 m	Uniform
Pile Diameter	Range: 210 mm – 318 mm Mean: 253 mm Median: 249 mm St. Dev.: 29.6 mm	Lognormal
Timber Compressive Strength	Range: 16.1 MPa – 23.3 MPa Mean: 19.9 MPa Median: 20.1 MPa St. Dev.: 2.7 MPa	Lognormal
Timber Tensile Strength	Range: 32.0 MPa – 123.4 MPa Mean: 70.2 MPa Median: 78.0 MPa St. Dev.: 37.2 MPa	Lognormal

The superstructure height, H, was defined as the measurement from the top of the deck component at the edge of the bridge to the top of the pile cap. The variation in superstructure height originates from the type of precast component used. In the survey of existing timber pile bridges, precast voided slab-beams and double T beams were the most common. The height of the superstructure and span length are important factors in a tsunami scenario because they directly affect the hydrodynamic forces.

The compressive strength distribution was applied to both the timber piles and the timber bracing. Stress-strain relationships for the timber piles were generated by assuming a constant strain of 0.008 at peak compressive stress regardless of the peak strength. This value corresponds to the mean strain level at which the compressive test specimens reached peak strength. The elastic modulus from the compressive behavior was used to calculate the strain at failure in tension. As shown in Figure 7.4, the timber material model generated in OpenSees represents the actual material behavior well.

7.2.2 Simplified Earthquake-Tsunami Loading

Structural response in sequential earthquake-tsunami events can be grouped into three categories: 1) earthquake dominated, 2) tsunami dominated, or 3) earthquake-tsunami interaction. The earthquake dominated case occurs when the ground motion is severe enough to cause failure before the arrival of tsunami waves. In a tsunami dominated case little to no damage is sustained during the earthquake and failure is almost entirely due to tsunami loading (Scott & Mason 2017). This study focuses on earthquake-tsunami interaction where both the ground motion and tsunami have a significant impact on the structure. In a sequential earthquake-tsunami loading scenario, it is important to ensure that a structure maintains sufficient post-earthquake strength capacity to resist the tsunami load effects. Treating earthquake and tsunami loads as two independent load cases which overlooks the damage that is carried over from the earthquake ground motion to the tsunami. The damage is a complex combination of strength and stiffness degradation as well as residual deformation which will adversely affect the structure's tsunami response. One simple way to capture earthquake damage is to represent its effect as an amplification of the tsunami drift demand. This is done by comparing the tsunami drift demand with and without earthquake damage. The amplification of tsunami effects due to earthquake damage can be expressed as

$$u_{max}^{*} = A u_{max} \tag{7.4}$$

Where u_{max}^{*} and u_{max} are peak tsunami drifts with and without preceding earthquake loading respectively, and A is the tsunami demand amplification factor. To determine the amplification factor for each timber pile bent, the analysis of each model in the Monte Carlo simulations was conducted in two steps. In the first step the bent was subjected to the hydrodynamic loading only with no earthquake loading to establish a baseline tsunami response. In the second step the bent was subjected to earthquake ductility demand through the half cycle pushover followed by the hydrodynamic force. The half cycle pushover displaced the deck up to a drift ratio corresponding to a predefined ductility demand then unloaded to zero lateral load.

To define the yielding point of each random bent a full pushover analysis was conducted prior to the earthquake-tsunami simulation. For unbraced bents the yield deformation was defined based on first yielding which typically occurred at approximately 50% of the ultimate lateral load. For braced bents yielding was defined using the reduced stiffness equivalent elastoplastic yield method (Park 1988). The reduced stiffness was computed as the secant stiffness at 50% of the ultimate lateral load. Figure 7.5 shows typical pushover curves for unbraced and braced timber pile bents and the yielding point definition.

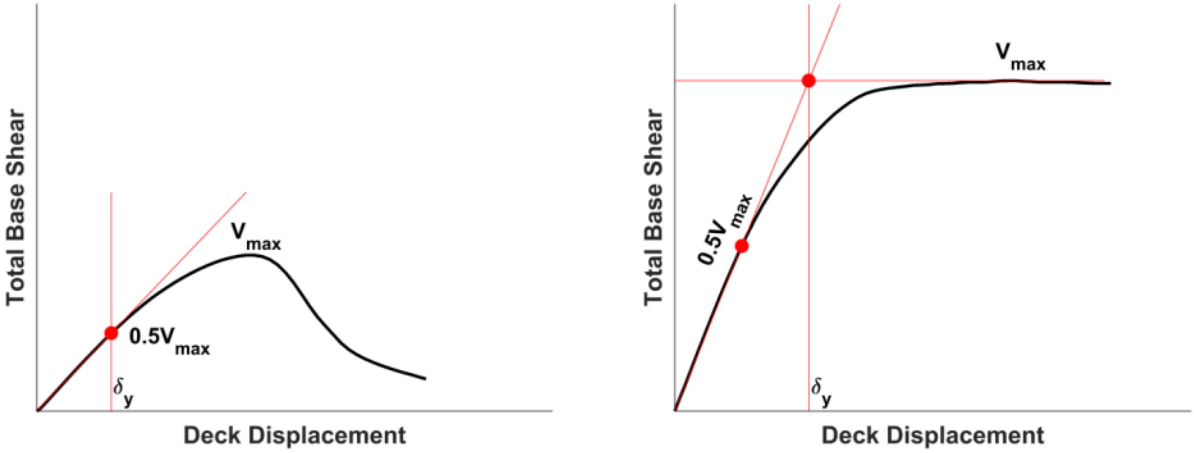

a)

b)

Figure 7.5 Definition of yielding in a) Unbraced bents, and b) Braced bents

Different definitions of yielding were adopted for the unbraced and braced cases because unbraced bents typically demonstrated considerably lower strength and deformation capacity due to the lack of redundancy. Therefore, the onset of yielding in the timber piles was determined to be more appropriate. As suggested by the typical pushover curves in Figure 7.5, bracing the timber piles significantly increases the strength and ductility. It was further observed that double bracing typically resulted in slightly higher strength and drift capacity compared to bents with single timber bracing.

Tsunamis can impart several different load effects on a structure including hydrostatic forces, hydrodynamic (drag) forces, uplift, and debris impact forces (FEMA 2012). However, analysis was limited to consideration of hydrodynamic forces which represent forces imparted on an object by a steady flow of fluid. Since the piles represent a very small contact area in comparison to the out-of-plane dimensions of the superstructure, it was assumed that the fluid-superstructure interaction constitutes 100% of the tsunami forces. The hydrodynamic force was calculated using

$$F_D = \frac{1}{2}\rho_s C_d B(hu^2) \tag{7.5}$$

Where ρ_s is the fluid density equal to 1,100 kg/m^3, representative of seawater with suspended sediments, C_d is the drag coefficient, taken as 2.0, B is the width of the structure in the direction normal to the flow, in this case the span length, h is the tsunami flow depth, and u is the depth averaged tsunami velocity (FEMA 2012). The quantity $h\mathrm{u}^2$ is known as the momentum flux and is directly related to the force that can be imparted by a fluid flow. The hydrodynamic force was applied to the rigid superstructure as a step function in the same direction as the pushover.

All bents with five piles along with six and seven pile bents with unbraced piles were subjected to a ductility demand of $\mu = 2$. Braced bents with six and seven piles were subjected to ductility demands of $\mu = 2$, and $\mu = 3$. For the tsunami loading, the maximum and minimum hydrodynamic force that can be resisted by each bent group was first determined by considering the most extreme possible bridge configuration. The corresponding maximum and minimum tsunami velocities were averaged and used to calculate the hydrodynamic force for each model. The earthquake demand and tsunami velocities assumed in each Monte Carlo simulation are summarized in Table 7.2. The 13 pushover-tsunami simulations shown in Table 7.2 make up the Monte Carlo simulations. As mentioned above, each group was represented by 500 random bent models.

Table 7.2 Earthquake ductility demand and tsunami velocity applied to each Monte Carlo group

	Unbraced		**Single Bracing**		**Double Bracing**	
	Ductility Demand	**Tsunami Velocity**	**Ductility Demand**	**Tsunami Velocity**	**Ductility Demand**	**Tsunami Velocity**
5 Piles	$\mu = 2$	2.4 m/s	$\mu = 2$	4.7 m/s	$\mu = 2$	5.0 m/s
6 Piles	$\mu = 2$	2.7 m/s	$\mu = 2$ $\mu = 3$	4.9 m/s 4.7 m/s	$\mu = 2$ $\mu = 3$	5.6 m/s 5.3 m/s
7 Piles	$\mu = 2$	3.0 m/s	$\mu = 2$ $\mu = 3$	5.1 m/s 5.0 m/s	$\mu = 2$ $\mu = 3$	5.7 m/s 5.4 m/s

For identical levels of earthquake ductility demand, the tsunami velocity applied to bents with single and double bracing were more than 70% and 90% greater respectively than those applied to unbraced bents. Since the values shown in Table 7.2 were established based on the most extreme possible bridge configurations as explained above, the increased tsunami velocities are indicative of the added redundancy and capacity provided by the bracing.

7.2.3 Tsunami Demand Amplification

Each bent group consisted of 500 random samples for a total of 6,500 samples in the Monte Carlo simulation. A typical structural response to the simplified earthquake-tsunami loading is shown in Figure 7.6.

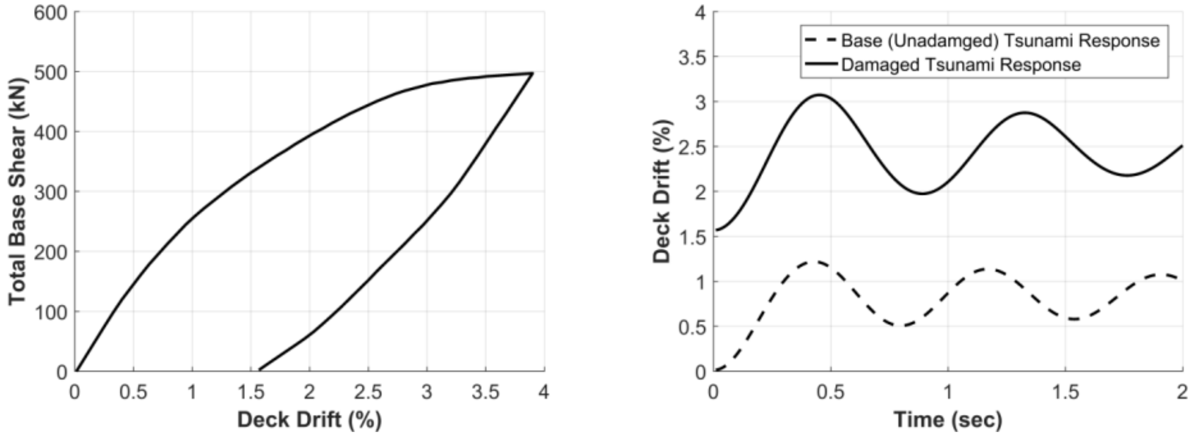

a) **b)**

Figure 7.6 Response of a six timber pile bent with single bracing **a)** Pushover ductility demand **b)** Tsunami response

Figure 7.6 a) shows the pushover simulating earthquake demand. The residual drift is clearly evident. Tsunami responses with and without preceding earthquake loading are compared in Figure 7.6 b). In the damaged case, the tsunami response begins with the residual drift from the pushover. The earthquake damage also results in stiffness loss which is evident in period elongation in the tsunami response. For this example the tsunami demand amplification factor, A, defined as the ratio of damaged peak tsunami demand to undamaged peak tsunami demand, is approximately 2.5. For each case in the Monte Carlo simulations, A was calculated using Equation (7.4). The results are plotted in Figure 7.7 using box plots to show the observed variation. Figure 7.7 a) shows the distribution of the undamaged base peak tsunami response and Figure 7.7 b) shows the tsunami demand amplification factor, A. In each boxplot the red line indicates the median while the blue box delineates the middle 50% of the data. The dotted lines indicate the upper and lower 25% of the distribution.

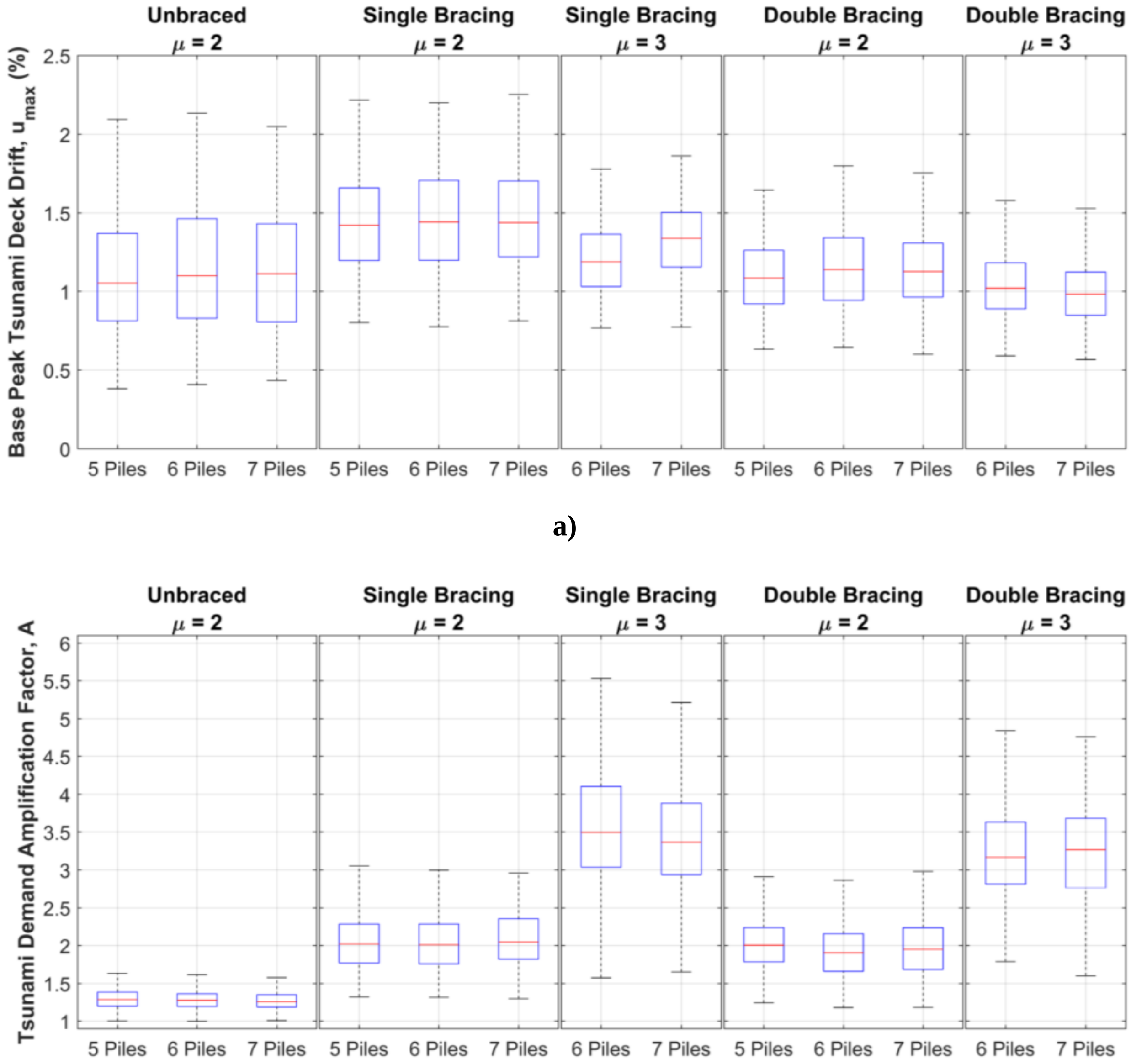

a)

b)

Figure 7.7. Monte Carlo simulation results **a)** Base peak tsunami deck drift **b)** Tsunami demand amplification factors

The box plots provide useful insight into the performance of the timber pile bridges. Between the unbraced and single braced cases in Figure 7.7 a), the median base tsunami response of the single braced bents was approximately 30% greater than that of the unbraced case. Considering the tsunami velocity prescribed to the single bracing simulation group was more than 1.7 times that applied to the unbraced piles (see Table 7.2), this is a relatively modest increase and indicative of the added stiffness provided by the bracing. Between single bracing and double bracing, it can be seen that adding a second set of cross bracing can even further improve a bridge's performance. These observations extend to performance under combined earthquake-tsunami loading. Although comparable tsunami demand amplification factors were observed for the single and double bracing cases, the maximum base tsunami drift was lower in bents with double bracing by at least 25% and 22% for earthquake ductility demands of 2 and 3, respectively. This clearly highlights the benefits of structural redundancy provided by the cross bracing. In the case of unbraced piles, the tsunami demand amplification factor is relatively low. However, given that unbraced timber pile bents typically have low ductility capacity, even moderate levels of earthquake damage can significantly increase the risk of structural failure.

It is also worth noting that there is significantly more variation in the base tsunami response in unbraced piles than in the braced cases. Without the ability to redistribute loads, the performance of unbraced timber pile bents is critically dependent on the capacity of each individual pile. This means that a single deficient pile can severely limit the overall capacity of a bridge. In contrast, providing alternate load paths through bracing effectively smooths out the differences between the piles and leads to significantly higher strength and ductility. These observations are also evident in the regression models discussed below.

Since the amplification factor is a relative term, the magnitude of the factor has little significance on its own. However, it is important to point out what the factor signifies is that damage sustained from the preceding earthquake ground motion amplifies the effect of the ensuing tsunami loads. The amplification factors reached as high as 1.63, 3.05, and 2.95 for the unbraced, single braced, and double braced timber pile bents, respectively subjected to a ductility demand of 2. This clearly demonstrates that designing a structure under earthquake and tsunami load demands independently of each other could be detrimental.

7.2.4 Regression Analysis

Once all bent samples were analyzed, linear regression was performed to relate bridge and material parameters to tsunami demand amplification. In the regression, the inverse of the amplification factor was adopted as the response variable to satisfy the homoscedasticity assumption. Superstructure dimensions (height (H), and span length (B)), exposed pile length (L), average pile diameter (d_{avg}), average timber pile strength (compressive ($f_c|_{avg}$), and tensile ($f_t|_{avg}$)), and bracing strength ($f_c|_{brc}$) were the predictors. To first compare the regression models the predictor variables were standardized by subtracting the mean from each sample value then dividing by the standard deviation. In all cases all predictors were determined to be statistically significant. In Figure 7.8, scatter plots with a fitted line for superstructure height, H is shown on the left, while the fitted lines for each predictor variable are compared in the plot on the right. The fitted line plots show the general influence of each predictor on the tsunami demand amplification factor. All results presented in Figure 7.8 are for bents with six timber piles.

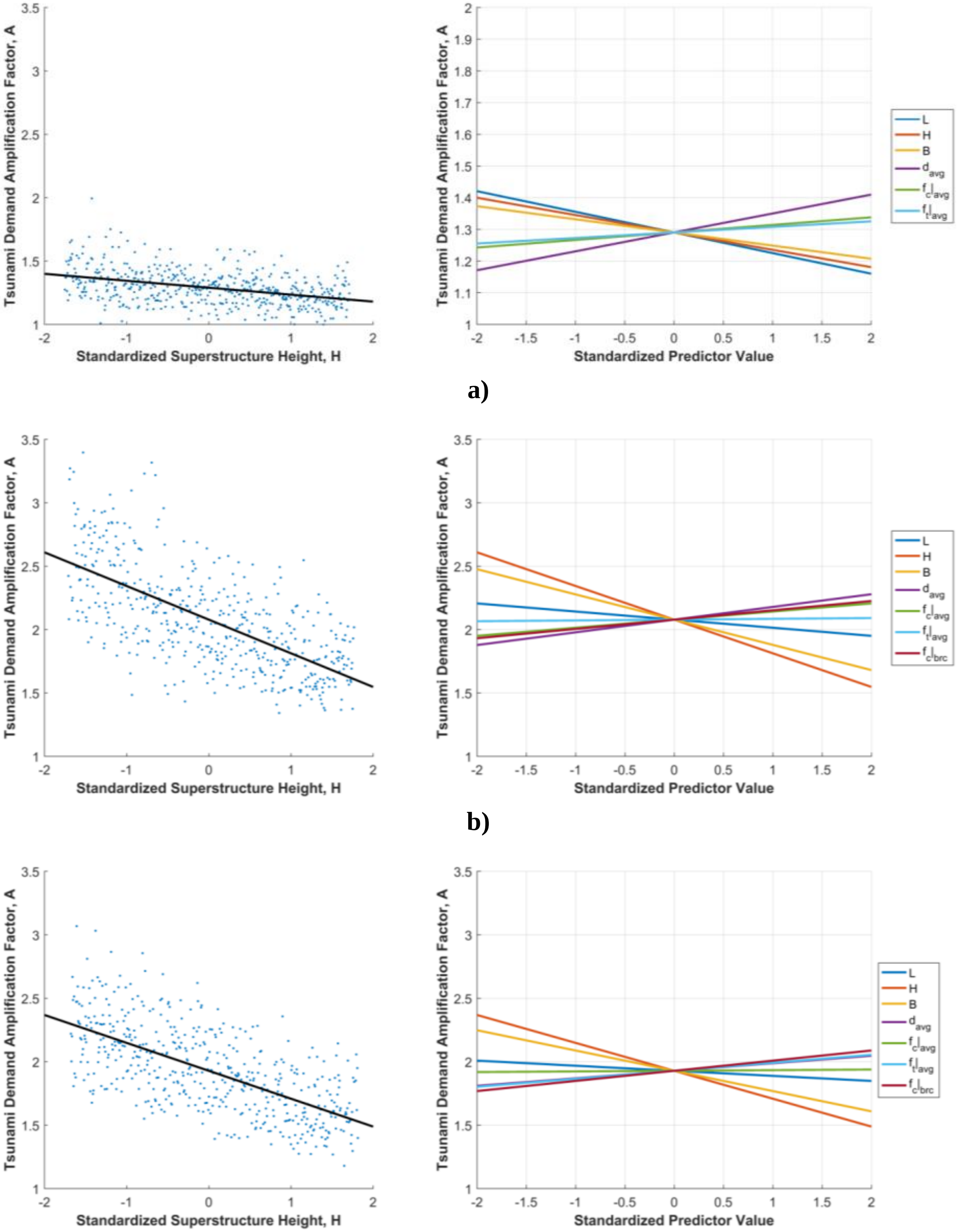

a)

b)

c)

Figure 7.8 Scatter plots showing amplification factor correlation to pile length and superstructure height for six pile bents **a)** Unbraced **b)** Single bracing **c)** Double bracing

The scatter plots clearly demonstrate the variability in the Monte Carlo simulation results. Several observations can be made from comparing the slope of the fitted lines. The first thing to note is the sign of each fitted line. Pile length above the ground surface, superstructure height, and span length negatively influence the amplification factor, decreasing the amplification factor with increasing value. Increasing average pile diameter and the pile and bracing strength parameters increase the amplification factor. The counterintuitive nature of the signs is due to the fact that the tsunami demand amplification factor is defined as a ratio (see Equation (7.4)), and the magnitude of the actual factor is relative to the base tsunami drift.

The slope of the fitted lines also gives insight about the level of dependence on each predictor. For the unbraced bent, pile length and diameter have the strongest impact on tsunami demand amplification. With bracing, the amplification factor becomes predominantly correlated to superstructure height. As discussed above, this is due to the fact that bracing reduces the effect of individual piles on the performance of the bent. This is shown by the reduced correlation to pile diameter and pile strength. In general, superstructure dimensions, H, and B, strongly affect the tsunami demand amplification factor regardless of the number of piles or bracing configuration. This is reasonable since the tsunami induced load is directly proportional to impact area presented by the deck. It is also clear that the geometric characteristics of the timber piles (i.e. length and diameter) generally affect the overall performance more than the material strengths. The strength of the timber piles is a relatively minor factor. This highlights the importance of structural stiffness over strength. With the exception of impact loads from floating debris, tsunami loading is of sustained nature (ASCE/SEI 2017). Therefore, it is important to ensure sufficient post-earthquake structural stiffness in addition to strength.

Regression models without standardization of the predictor variables are summarized in Table 7.3. For a given timber pile bridge, the regression model shown in Table 7.3 can be used to estimate the tsunami demand amplification factor. It should be noted that the regression models predict the inverse of the amplification factor, A^{-1}.

The R^2 statistic and the standard error of regression suggest the linear models are able to predict the demand amplification with good precision. Lower R^2 values seen in the high ductility demand ($\mu = 3$) cases indicate increased variation in the results. This is primarily attributable to disparities in the ductility capacity of the models. However, the standard error values suggest the precision of predictions from the regression models is largely unchanged. In each regression, the residuals were checked in each case to verify that the error was random.

Table 7.3 Linear regression summary and regression coefficients

Simulation Group			Linear Regression Summary		Regression Coefficients							
No. of Piles	**Bracing**	**Ductility Demand, μ**	**R^2 (%)**	**Standard Error**	**Const.**	**L (m)**	**H (m)**	**B (m)**	**d_{avg} (mm)**	**$f_c\vert_{avg}$ (MPa)**	**$f_t\vert_{avg}$ (MPa)**	**$f_c\vert_{brc}$ (MPa)**
5	Unbraced	2	82.0	0.037	1.102	0.124	0.319	0.032	-0.003	-0.011	-0.001	-
	Single Bracing	2	83.2	0.041	0.583	0.056	0.558	0.055	-0.003	-0.011	0.000	-0.010
	Double Bracing	2	79.1	0.036	0.457	0.052	0.471	0.049	-0.002	-0.006	-0.001	-0.008
6	Unbraced	2	80.7	0.035	1.080	0.126	0.310	0.033	-0.003	-0.010	-0.001	-
	Single Bracing	2	84.4	0.038	0.556	0.068	0.541	0.051	-0.003	-0.010	0.000	-0.009
		3	67.9	0.038	0.441	0.034	0.374	0.033	-0.002	-0.007	0.000	-0.007
	Double Bracing	2	82.4	0.040	0.407	0.068	0.560	0.056	-0.002	-0.008	0.000	-0.014
		3	64.8	0.037	0.273	0.057	0.336	0.027	-0.001	-0.005	-0.001	-0.005
7	Unbraced	2	81.5	0.034	1.191	0.124	0.305	0.028	-0.004	-0.011	-0.001	-
	Single Bracing	2	82.2	0.039	0.579	0.070	0.494	0.052	-0.003	-0.008	0.000	-0.008
		3	61.8	0.039	0.403	0.049	0.362	0.034	-0.002	-0.010	0.000	-0.004
	Double Bracing	2	79.5	0.043	0.500	0.094	0.508	0.053	-0.003	-0.010	-0.001	-0.010
		3	67.7	0.037	0.193	0.071	0.292	0.029	-0.001	-0.002	0.000	-0.006

7.3 VALIDATION OF MONTE CARLO SIMULATION RESULTS

7.3.1 PFEM Tsunami Analysis

To validate the results of the Monte Carlo simulations, analyses with a more detailed tsunami simulation using PFEM was carried out. Similar to the tsunami simulation in Chapter 6, the tsunami was modeled as an idealized bore with a prescribed height and initial velocity. The initial setup of the PFEM tsunami simulation is illustrated in Figure 6.7.

The PFEM tsunami simulations were preceded by the same level of pushover ductility demand which imposed the same level of damage in the timber piles as in the simplified analyses that made up the Monte Carlo simulations. The height of the tsunami bore was assumed to extend to the top of the deck. This ensured that the initial momentum flux of the tsunami bore applied the same horizontal force to the superstructure as the hydrodynamic force applied in the Monte Carlo simulations. The key aspect of this comparison is to verify the adequacy of the hydrodynamic loading considered in the simplified analysis and validate the linear regression models.

7.3.2 Response Comparison

Five timber pile bents with six piles and single bracing were selected to verify the validity of the simplified hydrodynamic tsunami loading using more detailed PFEM simulations. Since the regression models showed that deck height was the most critical parameter for this case, models were selected to represent a variation in the deck height. Details of each bent are given in Table 7.4 along with their respective tsunami demand amplification factors predicted using the regression model.

Table 7.4 Six pile bents with single cross bracing selected for detailed tsunami analysis

	Case 1	**Case 2**	**Case 3**	**Case 4**	**Case 5**
L (m)	2.65	2.00	2.27	1.93	2.18
H (m)	0.73	0.81	0.91	1.02	1.11
B (m)	7.83	8.80	9.78	8.13	8.71
d_{avg} (mm)	261	269	262	249	253
$f_c\|_{avg}$ (MPa)	20.24	19.84	18.23	19.79	20.07
$f_t\|_{avg}$ (MPa)	61.14	96.39	115.15	87.01	90.74
$f_c\|_{brc}$ (MPa)	21.11	17.84	20.24	18.75	17.93
Regression Predicted Amplification Factor, A	2.74	2.47	1.86	1.86	1.60

All cases shown in Table 7.4 were subjected to a pushover ductility demand of $\mu = 2$ prior to the PFEM tsunami simulation. The predicted tsunami demand amplification factors shown in Table 4 suggest considerable damage is sustained by each of the bents. Snapshots from a PFEM tsunami simulation are shown in Figure 7.9 with a comparison of the simplified tsunami simulation response and PFEM tsunami response.

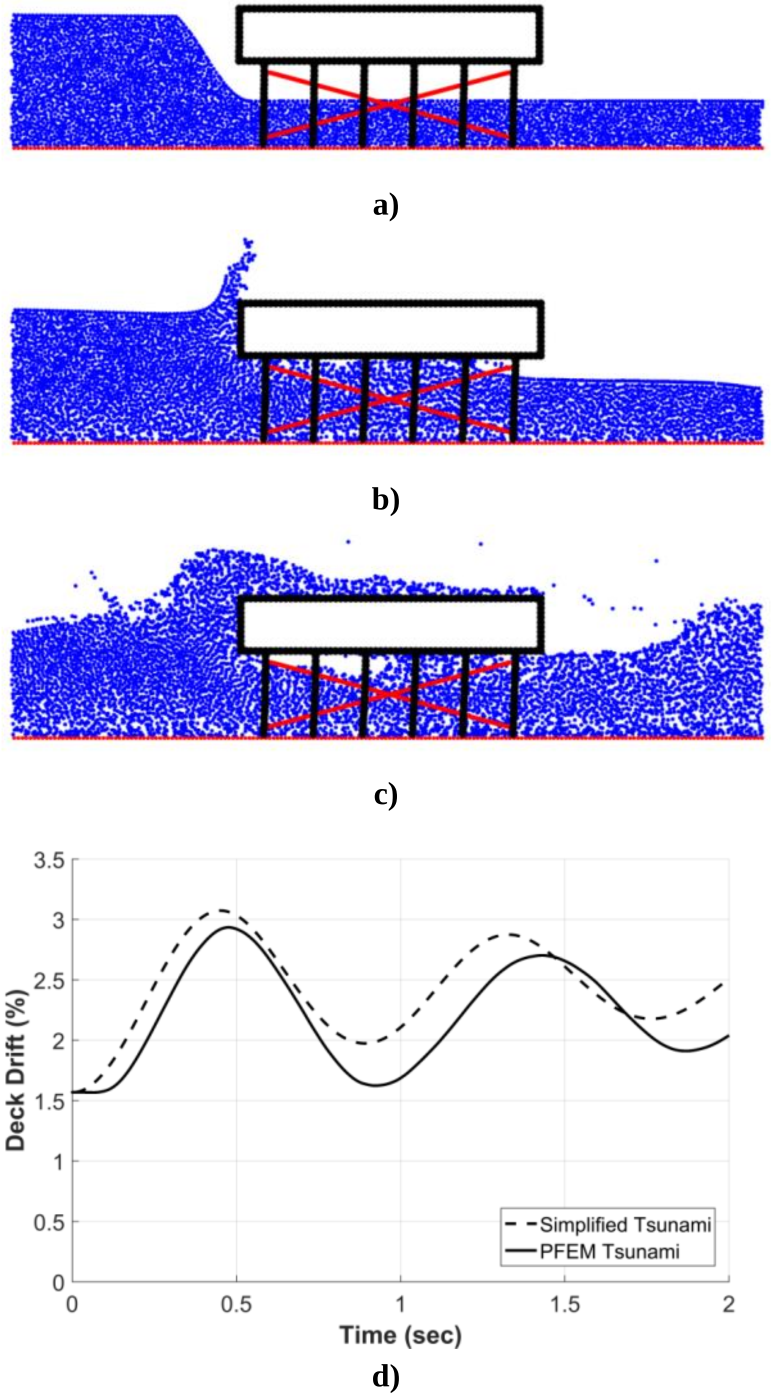

Figure 7.9 Tsunami simulation using PFEM at time **a)** t = 0.0 sec **b)** t = 1.0 sec **c)** t = 3.0 sec, and tsunami response comparison, **d)**

The PFEM solution offers a more accurate representation of real tsunami wave impact than applying only the hydrodynamic force as it effectively captures all the dynamic load effects of the fluid-structure interaction. However, the simplified tsunami loading generally yielded slightly higher tsunami drifts. This is most likely due to the fact that the simplified hydrodynamic load was sustained at a constant magnitude over the entire duration of the simulation unlike the PFEM tsunami bore. In Table 7.5, peak drifts obtained from the pushover-PFEM simulations are compared to the simplified earthquake-tsunami analysis results from the Monte Carlo simulations, and the amplified peak drift calculated using Equation (7.4) and the predicted amplification factors shown in Table 7.5.

Table 7.5 Comparison of post-earthquake tsunami drift demand

	Post-Earthquake Peak Tsunami Deck Drift (%)				
	Case 1	**Case 2**	**Case 3**	**Case 4**	**Case 5**
Pushover-PFEM Tsunami	2.06	2.94	2.79	2.84	3.11
Simplified Earthquake-Tsunami	2.44	3.07	3.15	2.86	3.34
Prediction Using Regression Model Amplification Factor	2.38	3.01	3.21	3.02	3.47

Overall, the PFEM tsunami response compared well with the hydrodynamic loading with the PFEM analysis results yielding conservative peak deck drifts by as much as 18%. There is a slight discrepancy between the regression model based estimation and the actual simplified earthquake-tsunami analysis results. It is worth noting that the tsunami demand amplification factor obtained from the regression models yielded post-earthquake tsunami demand estimates that were slightly more conservative than the PFEM based simulations by up to 15%. This shows that the more simplified approach proposed in this paper can yield reliable results compared to more detailed methods. However, given the limited number of cases considered here, this needs to be validated against a larger sample size.

7.4 SUMMARY OF CHAPTER 7

In this chapter, a tsunami demand amplification factor was introduced as a simple approach to reflect the effect of structural damage sustained during the earthquake in the subsequent tsunami demand. Monte Carlo simulations were performed on randomly generated timber pile bridge models to develop regression models that can provide reliable tsunami amplification factors. The main findings from the study are summarized below:

- Under identical earthquake ductility demands, braced bents resisted tsunami velocities up to 70% higher than unbraced timber pile bents.
- Compared to timber pile bents with single bracing, double bracing lowered the peak deck drift under tsunami loading by up to 25%. This highlights adding stiffness and redundancy to timber pile bridges is highly important to its resilience.
- The earthquake demand simulated through static pushover resulted in considerable residual deformations and loss of stiffness in the timber piles.
- Imposing a ductility demand of 2 prior to tsunami loading amplified the peak tsunami drift by up to 1.63, 3.05, and 2.95 for the unbraced, single braced, and double braced timber pile bents, respectively compared to the base tsunami response with no earthquake damage. Significantly higher amplifications were observed under a ductility demand of 3. This clearly demonstrates that the effect of earthquake damage must be factored into tsunami design considerations.

- Regression models showed that the size of the superstructure has a considerable impact on the combined earthquake-tsunami demand regardless of the pile and bracing configuration.
- In general, pile size was a more significant factor in the tsunami demand amplification. However, the addition of bracing elements hides the influence of individual piles on the overall performance of the bent.
- The simplified loading procedure yielded comparable results to the PFEM simulation. Furthermore, it was shown that the regression models developed in this paper can provide reliable, conservative estimates of the tsunami demand amplification.

CHAPTER 8

CONCLUSIONS AND RECOMMENDATIONS

8.1 CONCLUSIONS

This research aimed to address some key deficiencies and problems facing timber pile bridges through four main objectives: 1) Developing a comprehensive load rating method for piles carrying compression and lateral loads, 2) Introducing FRP retrofit design guidelines for deteriorated timber piles, 3) Investigating the long-term performance of FRP retrofitted timber piles, and 4) Investigating timber pile bridge performance under various multi-hazard loading scenarios that were not anticipated in the original design. Below, the main conclusions from the studies in Chapters 3 to 7 are summarized to show how these objectives were satisfied.

8.1.1 Chapter 3: Long-term Performance of FRP Strengthened Timber Piles

The effectiveness of FRP composites for strengthening timber structural members has been demonstrated in various studies as well as in this study. One of the main obstacles hindering their use in the field is uncertainty surrounding their durability. To evaluate the long-term performance of FRP wrapped timber piles, field-extracted Red Oak timber pile specimens were retrofitted with GFRP composites fabricated with three different types of resin and subjected to an accelerated aging procedure to artificially induce deterioration that would take years to develop in the field over a relatively short period of time. The specimens were then tested under uniaxial compression to determine if the aging process affects the performance. Although the accelerated aging procedure did have a degrading effect on the strength of the FRP wrapped pile specimens, it was much less severe compared to unretrofitted specimens.

Increasing the thickness of the FRP led to higher strength retention and improved ductility. The accelerated aging procure had no visible effect on the composite itself. These results suggest that FRP retrofits can reliably protect and strengthen bridge timber piles in the long term.

8.1.2 Chapter 4: Full-Scale Testing of Abutment Timber Piles Retrofitted with FRP Composites

For deteriorated timber pile bridge abutments, fully confining the timber piles using FRP is not possible due to the backing wall. Therefore, FRP retrofits can only be applied to the tension face of the piles as reinforcement. In this study, the effectiveness of this retrofitting technique was experimentally tested using three full-size timber piles. The results showed that in order to design effective FRP retrofits, detailed knowledge about the in-situ timber condition and level of deterioration is needed. The retrofit design needs to be tailored to the specific condition of a pile and the target performance level. To further investigate this approach, SWT measurements taken on the specimens and the test results were used to carefully calibrate an FE model with deteriorated timber material properties. The FE model was used to iteratively determine the volumetric ratio of FRP that would be required to sufficiently restore the capacities of the deteriorated abutment piles under varying levels of bending moment. This study demonstrated that SWT measurements may be used to establish a quantitative relationship between timber condition and stiffness which can then be used to determine the existing structural capacity of a pile and design the retrofit accordingly.

8.1.3 Chapter 5: Load Rating of Deteriorated and FRP Retrofitted Abutment Timber Piles

This chapter presented a modified allowable stress load rating method for deteriorated and FRP retrofitted abutment timber piles which accounts for combined axial-flexural loading.

The load rating method and FRP retrofitting approach introduced in this chapter can be applied to different bridge geometries, loading conditions, and timber pile conditions to estimate the in-situ structural capacity that engineers can use to make repair/retrofit decisions. A finite element model of a single abutment timber pile was used to evaluate the modified load rating method over a range of key bridge parameters dead load magnitude, pile length, and section loss. It was shown that increasing the dead load from 44.5 kN to 178 kN can reduce the allowable live load stress by at least 37% and increasing the pile length from 1.83 m to 2.44 m can result in reductions of up to 87%. Section loss eccentrically affecting the pile cross-section (see Profiles II and III) generally have a more critical impact on the performance of abutment timber piles and can reduce the allowable live load by up to 75%. Overall, deterioration Profile I yields less critical results compared to Profiles II and III. For severe deterioration, Profiles II and III can yield up to 75% lower allowable live load stress than Profile I with a 44.5 kN dead load. Results from the study based on the finite element model were compiled into a series of load rating charts which can be used to estimate the capacity of an abutment timber pile under varying conditions. The load rating method was further demonstrated using a prototype timber pile bridge and used to develop a design

8.1.4 Chapter 6: Multi-Hazard Assessment and Retrofit of Deteriorated Timber Pile Bridges

Compared to research studies on the behavior and performance of reinforced concrete and steel structures, there is almost no information available in the literature relating to heavy timber structures such as timber pile bridges. With growing interest to expand the scope of structural designs to extreme loads from multiple hazards, the knowledge gap is expanding. In this chapter, the performance of a model bridge with timber pile substructure and precast concrete superstructure was examined in a multi-hazard scenario involving three hazards: timber deterioration, earthquake, and tsunami loading. As a countermeasure to timber deterioration, a retrofitting strategy using FRP composites was also investigated. Material models for as-is timber piles and FRP confined timber piles were derived based on experiments conducted on field-extracted specimens. The earthquake and tsunami hazards were simulated sequentially in OpenSees with PFEM being used to conduct the tsunami simulation. The capacity of the prototype timber pile bent was evaluated in an incremental manner and presented in terms of the hazard intensity using hazard interaction diagrams. The limit state curve can be divided into tsunami dominated, earthquake dominated, and earthquake-tsunami interaction regions depending on the damage sustained during the earthquake ground motion. The results also showed that although a timber pile bent demonstrates sufficiently high residual capacity to resist tsunami forces after earthquake loading, a 25% section loss affecting a single pile can reduce that capacity by up to 50%. In the case of a bent with a deteriorated pile, structural retrofits must consider load redistribution and also adequately strengthen the adjacent timber piles. With proper design, FRP confinement can improve the capacity of a deteriorated timber pile bent under sequential earthquake-tsunami loading.

8.1.5 Chapter 7: Evaluation of Damage in Timber Pile Bridges Subjected to Earthquake-Tsunami Scenarios

While codes and guidelines are being revised to include tsunami hazards in new design, existing structures designed based on outdated provisions are at high risk. Furthermore, although design earthquake and tsunami loads can be estimated from various guidelines, codes provisions are not very clear on the effect damage sustained during the earthquake episode has on a structure's ability to resist subsequent tsunami loads. This chapter focused specifically on the interaction effect of earthquake-tsunami loads on timber pile bridge substructure. First, a tsunami demand amplification factor was introduced as means to capture the effect of accumulated damage from the initial earthquake loading. Then, a Monte Carlo simulation was carried out to develop linear regression models for estimating the amplification factor for a variety of braced and unbraced timber pile bents. The Monte Carlo simulation used simplified quasi-static loads to estimate the seismic and tsunami induced loads. The results were validated against more detailed dynamic analyses using PFEM and found to yield comparable results. The analysis results showed that earthquake damage can increase the deck drift demand imposed by tsunami loading by more than 60% compared to tsunami loading with no preexisting damage. Overall, the size of the timber piles was the most significant factor in how much damage would be sustained under lateral earthquake loads and the resulting magnitude of the tsunami demand amplification. However, the addition of bracing elements hides the influence of individual piles on the overall performance of the bent. The study provides a simple approach to predict the performance of timber pile bridges in earthquake-tsunami loading scenarios based on which repair or strengthening measures can be designed.

8.2 RECOMMENDATIONS FOR FUTURE RESEARCH

Although a bridge as a structural system is made up of many different components, this research focused specifically on timber pile substructure. The investigative studies that comprise this research could be extended to aged and deteriorated reinforced concrete or steel bridge structures but even within the scope of timber bridges, there are several areas that could be the subject of future research.

- SWT has been shown to be a simple and effective way to identify deterioration in timber piles. However, the correlations drawn between SWT condition assessments and timber pile behavior in this research study were based on limited samples size. Therefore, further investigation is needed to establish a clear relationship between stress wave transmission characteristics and timber material behavior.
- The experimental investigation of FRP retrofits in this research did not examine the bond strength between FRP and timber. Since timber piles are typically treated with preservatives, and their surfaces are porous and uneven, both short-term and long-term bond strength should be examined. This is especially important for partial FRP retrofits in which the FRP is used as flexural reinforcement.
- Numerical simulation of tsunami impact on a timber pile bent showed that very high uplift forces are generated on the superstructure. Field surveys in the aftermath of past tsunamis have also identified deck uplift as a common failure mode in bridges. Since timber pile bridges are very simple structures with simply supported decks, the bridge system should be modeled in more detail to assess the possibility of deck uplift.
- The earthquake-tsunami hazard interaction diagrams developed in Chapter 6 demonstrated the failure limit of a timber pile bridge in a deterministic fashion using a prototype bridge and a limited selection of ground motion records. However, this approach has clear limitations and a more probabilistic approach should be pursued to establish fragility curves that can aid engineers and governing agencies in decision-making processes. Although the idea of fragility has been accepted in most areas of structural engineering, it has not yet been widely adapted to multiple hazard scenarios such as earthquake-tsunami events.

REFERENCES

Agerschou, H. A. (1962). Analysis of the Engineering News Pile Formula. *Journal of the Soil Mechanics and Foundations Division – Proceedings of the American Society of Civil Engineers*, *88*, 1-11.

Allicock, D. R. (1999). Experimental study of timber piles subjected to reverse cyclic loading. M.S. thesis. State University of New York at Buffalo, Buffalo, NY.

American Association of State Highway and Transportation Officials (AASHTO). (2002). *Standard specifications for Highway Bridges*. Washington, DC.

American Association of State Highway and Transportation Officials (AASHTO) (2012). *LRFD Bridge Design Specifications 6th ed.*, Washington, DC.

American Association of State Highway and Transportation Officials (AASHTO) (2011). *Manual for Bridge Evaluation 2nd ed.*, Washington, DC.

American Forest and Paper Association (AFPA). (2005). *National Design Specification (NDS) for Wood Construction*, Washington DC.

American Society of Civil Engineers/Structural Engineering Institute (ASCE/SEI). (2017). *Minimum design loads and associated criteria for buildings and other structures. ASCE/SEI 7-16*, Reston, VA.

American Wood Preservers Institute (AWPI), Timber Piling Council (2002). *Timber Pile Design and Construction Manual*. AWPI. Vancouver, WA.

Andrawes, B., and Caiza, P. (2011). Bridge Timber Piles Load Rating under Eccentric Loading Conditions. *Journal of Bridge Engineering*, *17*(4), 700-710.

Ang, A. H.-S., Tang, W.H. (2007). *Probability concepts in engineering: Emphasis on applications to civil & environmental engineering, 2nd ed.*. New York: Wiley.

Armstrong, J. P.; Patterson, D. W., & Sneckenberger, J. E. (1991). Comparison of three equations for predicting stress wave velocity as a function of grain angle. *Wood and Fiber Science*, *23*(1), 32-43.

Arnason, H., Petroff, C., & Yeh, H. (2009). Tsunami bore impingement onto a vertical column. *Journal of Disaster Research*, *4*(6), 391-403.

ASTM D1037-12 (2012). *Standard Test Methods for Evaluating Properties of Wood-Base Fiber and Particle Panel Materials*. ASTM International, West Conshohocken, PA, 2012, https://doi.org/10.1520/D1037-12.

ASTM D143-14 (2014) *Standard Test Methods for Small Clear Specimens of Timber*. ASTM International, West Conshohocken, PA, 2014, https://doi.org/10.1520/D0143.

ASTM D25-12(2017a). *Standard Specification for Round Timber Piles*. ASTM International, West Conshohocken, PA, 2017, https://doi.org/10.1520/D0025-12R17.

ASTM D2899-12 (2017b). *Standard Practice for Establishing Allowable Stresses for Round Timber Piles.* ASTM International, West Conshohocken, PA, 2017, https://doi.org/10.1520/D2899-12R17

Avent, R. R. (1989). Durability of Posted and Epoxy-Grouted Timber Piles. *Journal of Structural Engineering*, *115*(4), 826-833.

Azadbakht, M., & Yim, S. C. (2014). Simulation and estimation of tsunami loads on bridge superstructures. *Journal of Waterway, Port, Coastal, and Ocean Engineering*, *141*(2), 04014031.

Borello, D. J., Andrawes, B., Hajjar, J., Olson, S. M., Hansen, J., and Buenker, J. (2009). Forensic collapse investigation of a concrete bridge with timber piers. *Illinois Center for Transportation (ICT).*

Borello, D. J., Andrawes, B., Hajjar, J. F., Olson, S. M., and Hansen, J. (2010). Experimental and analytical investigation of bridge timber piles under eccentric loads. *Engineering Structures*, *32*(8), 2237-2246.

Brites, R.D., Neves, L.C., Machado, J.S., Lourenço, P.B., Sousa, H.S. (2013). Reliability analysis of a timber truss system subjected to decay. *Engineering Structures, 46*, 184-192.

Broms, B. B. (1964). Lateral resistance of piles in cohesionless soils. *Journal of the Soil Mechanics and Foundations Division*, 90(3), 123-158.

Buchanan, A. H. (1984). Strength model and design methods for bending and axial load interaction in timber members. Doctoral dissertation. University of British Columbia. Vancouver, British Columbia, Canada.

Caiza, P., Shin, M., and Andrawes, B. (2012). Flexure-Compression Testing of Bridge Timber Piles Retrofitted with Fiber Reinforced Polymers. *Open Journal of Civil Engineering*, *2*(03), 115.

Carey, T., Mason, H. B., Barbosa, A. R., & Scott, M. H. (2014). Modeling framework for soil-bridge system response during sequential earthquake and tsunami loading. *Proc., 10th US National Conference on Earthquake Engineering*, Anchorage, AK.

Chanson, H. (2006). Tsunami surges on dry coastal plains: Application of dam break wave equations. *Coastal Engineering Journal*, *48*(04), 355-370.

Chellis, R. D. (1944). *Pile-Driving Handbok: Theory, Design, Practice of Pile Foundations*. Pitman Publishing Corporation, New York, NY.

Chellis, R. D. (1961). *Pile Founations*. McGraw-Hill, New York, NY.

Chock, G. Y. (2016). Design for tsunami loads and effects in the ASCE 7-16 standard. *Journal of Structural Engineering*, *142*(11), 04016093.

Chock, G., Robertson, I., Kriebel, D., Francis, M., & Nistor, I. (2013). Tohoku, Japan, Earthquake and Tsunami of 2011: Performance of Structures Under Tsunami Loads. American Society of Civil Engineers (ASCE), Reston, VA.

Chow, P., Reinschmidt, A.J., Barenberg, E. J. & Lewis, S.L. (1986) Laboratory Tests on Artificial Weathering of *Quercus rubra* Crossties. *Int. Res. Gr. On Wood Pres. Doc. IRG/WP/2252*. Sweden. 7 p.

Chow, P., Lewis, S. L., Reinschmidt, A. J., & Barenberg, E. J. (1987). Effects of Natural and Accelerated Aging on Oak Crossties. *American Wood-Preservers' Association Proceedings.*

Dahlberg, J., Phares, B., Bigelow, J., and Klaiber, F. W. (2012). *Timber Abutment Piling and Back Wall Rehabilitation and Repair*. No. IHRB Project TR-616.

Dassault Systèmes Simulia Corp. (2011). *ABAQUS 6.11*. Vélizy-Villacoublay Cedex, France.

Department of the Army (1985). *Pile Construction. Field Manual No. 5-134*. Headquarters, Department of the Army, Washington, DC.

Divos, F., & Szalai, L. (2002). Tree evaluation by acoustic tomography. In *Proceedings of the 13th international symposium on nondestructive testing of wood*, 251-256. Forest Products Research Society, Madison, WI.

Duwadi, S. R., and Wood, R. C. (1996). The Federal highway administration timber bridge program. *Proc., National Conf. on Wood Transportation Structures,* Madison, WI, 333-339.

Edelsbrunner, H., & Mücke, E. P. (1994). Three-dimensional alpha shapes. *ACM Transactions on Graphics (TOG)*, *13*(1), 43-72.

Emerson, R. N. (1999). Nondestructive evaluation of timber bridges. Doctoral dissertation. Washington State University. Pullman, WA.

Emerson, R. N. (2004). In situ repair technique for decayed timber piles. *Blandford G. Structures Congress*. Nashville: Structures, 1-9.

Erickson, E., & Wood, L. (1960). Strength and Related Properties of Wood Poles, *STP38342S Papers on Building Constructions*, STP38342S, D Committee and E Committee, Ed., ASTM International, West Conshohocken, PA, 81-87.

Fanous, F. S., Klaiber, F. W., & Eapen, A. S. (2003). *Evaluation of Appropriate Maintenance, Repair and Rehabilitation Methods for Iowa Bridges (No. TR-429,)*. Department of Civil & Construction Engineering, Iowa State University.

Federal Emergency Management Agency (FEMA). (2012). *Guidelines for Design of Structures for Vertical Evacuation from Tsunamis FEMA P-646,* Washington, DC.

Fisette, P. (2002). Controlling Termites and Carpenter Ants. Retrieved from https://bct.eco.umass.edu/publications/articles/controlling-termites-and-carpenter-ants/.

Fritz, H. M., Phillips, D. A., Okayasu, A., Shimozono, T., Liu, H., Mohammed, F., & Takahashi, T. (2012). The 2011 Japan tsunami current velocity measurements from survivor videos at Kesennuma Bay using LiDAR. *Geophysical Research Letters*, *39*(7), doi: 10.1029/2011GL050686.

Geist, E. L. (1998). Local tsunamis and earthquake source parameters. *Advances in Geophysics*, *39*, 117-209.

Geist, E. L., Titov, V. V., & Synolakis, C. E. (2006). Tsunami: wave of change. *Scientific American, 294*(1), 56-63.

Ghobarah, A., Saatcioglu, M., & Nistor, I. (2006). The impact of the 26 December 2004 earthquake and tsunami on structures and infrastructure. *Engineering structures*, *28*(2), 312-326.

Graham, J. S. (1996). Design of timber foundation piling for highway bridges and other structures. In *National Conference on Wood Transportation Structures* (No. FPL-GTR-94).

Groenier, J. S. (2006). Load Rating of Wood Bridges Using LRFD and ASD. In *Structures Congress 2006: Structural Engineering and Public Safety,* 1-10.

Hagos, M. W. (2001). Repair of heavily decayed timber piles using glass fiber-reinforced polymers (GFRP) and cementitious grout. M.S. thesis, University of Manitoba, Winnipeg, Manitoba, Canada.

Hannigan, P. J., Rausche, F., Likins, G. E., Robinson, B. R., & Becker, M. L. (2016). *Design and construction of driven pile foundations (Vol. I & II)*, Federal Highway Administration (FHWA) (Report No. FHWA-NHI-16-009 & FHWA-NHI-16-0010), Washington, D.C.

Highley, T. L., & Scheffer, T. (1989). Controlling decay in waterfront structures: Evaluation, prevention, and remedial treatments. Research paper FPL RP-US Department of Agriculture, Forest Service, Forest Products Laboratory (USA).

Holt, J. D., Chen, S., and Douglas, R. A. (1994). Determining lengths of installed timber piles by dispersive wave propagation. *Transportation Research Record*, (1447), 110-115.

Idelsohn, S. R., Oñate, E., & Pin, F. D. (2004). The particle finite element method: a powerful tool to solve incompressible flows with free-surfaces and breaking waves. *International journal for numerical methods in engineering*, *61*(7), 964-989.

Idelsohn, S. R., & Onate, E. (2010). The challenge of mass conservation in the solution of free-surface flows with the fractional-step method: Problems and solutions. *International Journal for Numerical Methods in Biomedical Engineering*, *26*(10), 1313-1330.

Idelsohn, S. R., Onate, E., Del Pin, F., & Calvo, N. (2006). Fluid-structure interaction using the particle finite element method. *Computer Methods in Applied Mechanics and Engineering*, *195*(17), 2100-2123.

Johns, K. C., & Lacroix, S. (2000). Composite reinforcement of timber in bending. *Canadian Journal of Civil Engineering*, *27*(5), 899-906.

Jung, J. (1979). *Stress wave grading techniques on veneer sheets* (Report No. FSGTR-FPL-27). Madison, WI: Forest Products Laboratory.

Kawashima, K., & Buckle, I. (2013). Structural performance of bridges in the Tohoku-Oki earthquake. *Earthquake Spectra*, *29*(S1), S315-S338.

Kim, Y. R., Ranjithan, S. R., Donato, P. J., & Murphy, C. M. (2000). *Nondestructive evaluation of the structural condition of timber piles* (Final Report) (FHWA/NC/2000-004). Raleigh, NC: North Carolina Department of Transportation.

Klaiber, F. W., White, D. J., Wipf, T. J., Phares, B. M., & Robbins, V. W. (2004). *Development of Abutment Design Standards for Local Bridge Designs – Vol. 1: Development of Design Methodology*. Iowa Department of Transportation Project TR – 486.

Köhler, J., Sørensen, J.D., & Faber, M.H. (2007). Probabilistic modeling of timber structures. *Structural Safety*, *29*(4), 255-267.

Kong, D., Johansson, N., Van Hees, P., Lu, S., & Lo, S. (2013). A Monte Carlo analysis of the effect of heat release rate uncertainty on available safe egress time. *Journal of Fire Protection Engineering*, *23*(1), 5-29.

Kornkasem, W., Foutch, D. A., & Long, J. H. (2001). *Seismic Behavior of Pile-Supported Bridges*. MAEC Report 03-05, University of Illinois at Urbana-Champaign, Urbana, IL.

Koshimura, S., & Mofjeld, H. O. (2001). Inundation modeling of local tsunamis in Puget Sound, Washington, due to potential earthquakes. *Proc., International Tsunami Symposium 2001*, Seattle, Washington, 861-873.

Koshizuka, S., & Oka, Y. (1996). Moving-particle semi-implicit method for fragmentation of incompressible fluid. *Nuclear science and engineering*, *123*(3), 421-434.

LSTC (Livermore Software Technology Corporation) (2015). *LS-DYNA R7.1.1*. Livermore, CA.

Lopez-Anido, R., Michael, A. P., and Sandford, T. C. (2003). Experimental characterization of FRP composite-wood pile structural response by bending tests. *Marine Structures*, *16*(4), 257-274.

Lumsden, G. Q. (1961). Strength and related properties of wood poles – An outstanding ASTM report. *Electrical Engineering*, *80*(10), 786-787.

Mander, J., Allicock, D., & Friedland, I. (2000). Seismic performance of timber bridges. *Transportation Research Record: Journal of the Transportation Research Board*, *1740*, 75-84, doi: 10.3141/1740-10.

Mansour, M.H. (1990). Variability analysis of timber bridge responses. *Structural Safety*, *9*(1), 41-58.

McKay, M.D., Beckman, R.J., & Conover, W.J. (1979). Comparison of three methods for selecting values of input variables in the analysis of output from a computer code. *Technometrics*, *21*(2), 239-245.

McKenna, F., Fenves, G. L., & Scott, M. H. (2000). *Open system for earthquake engineering simulation.* University of California, Berkeley, CA. Available from: http://opensees.berkeley.edu.

Mertz, D. (2012). *Steel Bridge Design Handbook: Load Rating of Steel Bridges*. Federal Highway Administration (FHWA) Report No. FHWA-IF-12-052 - Vol. 18. FHWA, Washington, DC.

Mirmiran, A., & Shahawy, M. (1997). Behavior of concrete columns confined by fiber composites. *Journal of Structural Engineering*, *123*(5), pp. 583-590.

Mirmiran, A., Shahawy, M., Nanni, A., Karbhari, V. M., Yalim, B., & Kalayci, A. S. (2008). Recommended construction specifications and process control manual for repair and retrofit of concrete structures using bonded FRP composites (No. Project 10-59B).

Najm, H., Secaras, J., & Balaguru, P. (2007). Compression tests of circular timber column confined with carbon fibers using inorganic matrix. *Journal of Materials in Civil Engineering*, *19*(2), pp. 198-204

Nistor, I., Palermo, D., Cornett, A., & Al-Faesly, T. (2011). Experimental and Numerical Modeling of Tsunami Loading on Structures. *Coastal Engineering Proceedings*, *1*(32), doi: https://doi.org/10.9753/icce.v32.currents.2

Oñate, E., Idelsohn, S. R., Del Pin, F., & Aubry, R. (2004). The particle finite element method – an overview. *International Journal of Computational Methods, 1*(02), 267-307.

Park, R. (1988). Ductility evaluation from laboratory and analytical testing. In *Proceedings of the 9th World Conference on Earthquake Engineering*, Tokyo-Kyoto, Japan.

Polous, H. G., & Davis, E. H. (1980). *Pile Foundation Analysis and Design*. John Wiley & Sons Inc., New York, NY.

Plevris, N., & Triantafillou, T. C. (1992). FRP-reinforced wood as structural material. *Journal of Materials in Civil Engineering*, *4*(3), 300-317.

Ritter, M. A. (1990). *Timber bridges: Design, construction, inspection, and maintenance*. United States Department of Agriculture (USDA), Forest Service, Washington, D.C.

Ross, R. J., & Pellerin, R. F. (1994). *Nondestructive testing for assessing wood members in structures* (Report No. FPL-GTR-70). Madison, WI: Forest Products Laboratory.

Ross, R. J., Degroot, R. C., Nelson, W. J., & Lebow, P. K. (1997). The relationship between stress wave transmission characteristics and the compressive strength of biologically degraded wood. *Forest Products Journal*, *47*(5), 89-93.

Ross, R. J., White, R. H., Pellerin, R. F., Wang, X., & Brashaw, B. K. (2004). *Wood and timber condition assessment manual, 2nd ed*. Madison, WI: Forest Products Laboratory.

Satake, K., & Tanioka, Y. (1999). Sources of tsunami and tsunamigenic earthquakes in subduction zones. *Pure and Applied Geophysics*, *154*(3-4), 467-483.

Scott, M.H., & Mason, H.B. (2017). Constant-ductility response spectra for sequential earthquake and tsunami loading. *Earthquake Engineering & Structural Dynamics*, *46*, 1549–1554.

Shama, A. A., & Mander, J. B. (2003). The seismic performance of braced timber pile bents. *Earthquake engineering & structural dynamics*, *32*(3), 463-482.

Shama, A. A., & Mander, J. B. (2004). Behavior of timber pile-to-cap connections under cyclic lateral loading. *Journal of Structural Engineering*, *130*(8), 1252-1262.

Shama, A. A., Mander, J. B., Friedland, I. M., & Allicock, D. R. (2007). *Seismic Vulnerability of Timber Bridges and Timber Substructures.* MCEER Technical Report No. MCEER-07-0008, State University of New York at Buffalo, Buffalo, NY.

Shewchuk, J. R. (1996). Triangle: Engineering a 2D quality mesh generator and Delaunay triangulator. In *Applied computational geometry towards geometric engineering*, Springer, Berlin, Heidelberg, 203-222.

Smulski, S.J. (1991). Relationship of stress wave and static bending determined properties of four northeastern hardwoods. *Wood and Fiber Science*, *23*(1), 44.57.

Steiger, R., and Fontana, M. (2005). Bending moment and axial force interacting on solid timber beams. *Materials and Structures, 38*(5), 507-513.

St-Germain, P., Nistor, I., & Townsend, R. (2012). Numerical modeling of the impact with structures of tsunami bores propagating on dry and wet beds using the SPH method. *International Journal of Protective Structures*, *3*(2), 221-255.

Timber Piling Council (2016). *Timber Pile Design & Construction Manual*. Southern Pressure Treaters' Association, Starkville, MS.

Tomlinson, M., & Woodward, J. (2008). *Pile design and construction practice, 5th ed.*. Taylor & Francis, Milton Park, Abingdon, UK.

US Department of Commerce (1962). *Standard Plans for Highway Bridges, Volume III – Timber Bridges*. Bureau of Public Roads, Washington, D.C.

Walhorn, E., Kölke, A., Hübner, B., & Dinkler, D. (2005). Fluid–structure coupling within a monolithic model involving free surface flows. *Computers & structures*, *83*(25-26), 2100-2111.

Wang, X., Divos, F., Pilon, C., Brashaw, B. K., Ross, R. J., & Pellerin, R. F. (2004). *Assessment of decay in standing timber using stress wave timing nondestructive evaluation tools: A guide for use and interpretation.* Forest Products Laboratory: Madison, WI.

Wei, Z., Dalrymple, R. A., Hérault, A., Bilotta, G., Rustico, E., & Yeh, H. (2015). SPH modeling of dynamic impact of tsunami bore on bridge piers. *Coastal Engineering*, *104*, 26-42.

Wilcox, W. W. (1978). Review of literature on the effects of early stages of decay on wood strength. *Wood and Fiber Science*, *9*(4), 252-257.

Wilkinson, T. L. (1968). *Strength Evaluation of Round Timber Piles, Forest Products Laboratory* (Report No. FSRP-FPL-101). Madison, WI.

Wipf, T. J., Klaiber, F. W., White, D. J., & Koskie, J. (2007). *Investigation of Steel-Stringer Bridges: Superstructures and Substructures (Vols. 1-2)* (Report No. IHRB Project TR-522). Ames, IA: Center for Transporation Research and Education, Iowa State University.

Wood, L. W. (1950). Formulas for columns with side loads and eccentricity. *Forest Products Laboratory*. Madison, WI.

Wood, L. W., Erickson, E. C. O., & Dohr, A. W. (1960). *Strength and Related Properties of Wood Poles* (Final Report), American Society for Testing Materials, Philadelphia, PA.

Xiao, Y., & Wu, H. (2000). Compressive behavior of concrete confined by carbon fiber composite jackets. *Journal of Materials in Civil Engineering*, *12*(2), 139-146.

Yeh, H. H. (1991). Tsunami bore runup. *Tsunami Hazard*, Springer, Netherlands, pp. 209-220.

Yeh, H. (2006). Maximum fluid forces in the tsunami runup zone. *Journal of waterway, port, coastal, and ocean engineering*, *132*(6), 496-500.

Yeom, G.-S. (2009). Behavior of a Container Drifted by Runup Tsunami and Estimation of its Collision Force. Doctoral Dissertation. Nagoya University, Japan.

Yim, S. C., Wei, Y., Azadbakht, M., Nimmala, S., & Potisuk, T. (2014). Case study for tsunami design of coastal infrastructure: Spencer Creek Bridge, Oregon. *Journal of Bridge Engineering*, *20*(1), 05014008.

Zhang, W., Song, X., Gu, X., & Tang, H. (2011). Compressive behavior of longitudinally cracked timber columns retrofitted using FRP sheets. *Journal of Structural Engineering*, 138(1), 90-98.

Zhu, M., & Scott, M. H. (2014a). Improved fractional step method for simulating fluid-structure interaction using the PFEM. *International Journal for Numerical Methods in Engineering*, *99*(12), 925-944.

Zhu, M., & Scott, M. H. (2014b). Modeling fluid–structure interaction by the particle finite element method in OpenSees. *Computers & Structures*, *132*, 12-21.

APPENDIX

AS-BUILT STRUCTURAL DRAWINGS OF EXISTING TIMBER PILE BRIDGES

This appendix contains the as-built drawings and structural details of nine existing timber pile bridges. The drawings are provided as a supplemental document in a single PDF file with the file name “Appendix - As-Built Structural Drawings of Existing Timber Pile Bridges.”